THESIS

2

(1998)

This is to certify that the

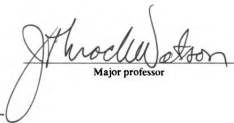dissertation entitled

NON-LINEAR ION ACCELERATION FOR IMPROVED MASS RESOLUTION IN TIME-OF-FLIGHT MASS SPECTROMETRY

presented by

Benjamin DeCamp Gardner

has been accepted towards fulfillment
of the requirements for

_____Ph.D._____ degree in __Chemistry__

Major professor

Date _18 December 1997_

PLACE IN RETURN BOX
to remove this checkout from your record.
TO AVOID FINES return on or before date due.

DATE DUE	DATE DUE	DATE DUE
FEB 2 0 2000		

NON-LINEAR ION ACCELERATION FOR IMPROVED MASS RESOLUTION IN TIME-OF-FLIGHT MASS SPECTROMETRY

By

Benjamin DeCamp Gardner

A DISSERTATION

Submitted to
Michigan State University
in partial fulfillment of the requirements
for the degree of

DOCTOR OF PHILOSOPHY

Department of Chemistry

1997

ABSTRACT

NON-LINEAR ION ACCELERATION FOR IMPROVED MASS RESOLUTION IN TIME-OF-FLIGHT MASS SPECTROMETRY

By

Benjamin DeCamp Gardner

The continued advancement of chromatographic separations techniques serves as a primary driving force for improved detector technologies. The capacity to rapidly separate complex analyte mixtures and achieve temporally narrow eluent peaks poses a serious challenge to even the most sophisticated detectors. To date, the mass spectrometer, which provides a second axis of information for multi-dimensional analysis, has been the detector of choice for the most discriminating analyses. Given the diminishing time frames, the time-of-flight mass spectrometer currently stands as the most appropriate detector technology, due to its combination of high-speed data acquisition capability, multi-channel detection specificity and superior detectability. Yet, if the time-of-flight mass spectrometer is to remain relevant to the emerging chromatographic techniques, fundamental improvements to basic mass spectrometer design will continue to be required.

In response to the challenges posed by the increasing chromatographic information density, research at Michigan State University has resulted in the development of a time-of-flight mass spectrometer and an accompanying data acquisition system that provides

mass spectral acquisition rates of up to 500 Hz and fully accommodates the requirements of high-performance gas chromatography-mass spectrometry. This dissertation documents some of the developments of this time-of-flight mass spectrometer system along with performance characteristics. It further examines the fundamental limitations to the achievement of mass resolving power and specifically delineates a method compensating for one of these limitations, that posed by the initial spatial distribution of ions along the optical axis within the time-of-flight ion source at the moment of creation in, or capture by, the applied electrical field. For the first time, the limitations to the model of space focusing using two-field linear ion acceleration developed by Wiley and McLaren [1] in 1955 is experimentally verified. A superior model based on a combination of linear and non-linear acceleration is theoretically evaluated and experimentally verified using a novel time-of-flight mass spectrometer designed to allow the probing of ion acceleration behavior in selected ion source regions with site-specific laser-induced photo-dissociation. The data show that, in extended-length ion sources, a greater than seven-fold improvement to resolving power may be expected by using non-linear ion acceleration. Finally, the relative merits of non-linear ion acceleration are discussed along with the potential application to various analytical techniques in which analyte introduction necessitates the use of a relatively large ion optical volume.

---

1. Wiley, W. C.; McLaren, I. H. *Rev. Sci. Instrum.* **1955**, *26*, 1150.

ACKNOWLEDGMENTS

While only one person puts his or her name on the cover, the research that results in endeavors such as this is invariably the product of many hands. My work is no exception to this, and there are many individuals to whom I am deeply grateful for their help. First, I am indebted to Dr. Watson for his guidance in my academic progress through the Ph.D. program. Dr. Watson has been very supportive of the unusual arrangement that led to my association and collaboration with Dr. Holland, and has many times filled in important gaps in my professional development. To Jack Holland I am especially grateful. Jack, you taught me to view science in a unique way and to pursue my instincts, even when the model I proposed was controversial. I will always be grateful for your support and encouragement. Your unconventional guidance, both in academia and industry, has helped lay a solid foundation for me, and your friendship has been priceless. To quote a time-worn phrase, "I owe you dinner."

Many others have also played a role in my success: Ron Tecklenburg, Raimund Grix, Chris Enke, George Yefchak, and David Sparkman have each been fruitful collaborators and good friends, as has Richard Berkley at the EPA, and Don Patterson, John Barr, and James Grainger at the Centers for Disease Control in Atlanta. Still others like Mike Davenport, Mel Micke, and Melinda Berning have each been of incredible assistance to me in the Mass Spectrometry Facility. My co-workers, including Ken Roth, Dave McLane, Paul Vlasek, Jennifer Johnson, and I have certainly shared many good times in

TABLE OF CONTENTS

LIST OF TABLES

LIST OF FIGURES

CHAPTER 1

GENERAL INTRODUCTION

Introduction

One of the great milestones in analytical chemistry has been the development and use of gas chromatography-mass spectrometry (GC-MS). Widely used, GC-MS is applied in a diverse and ever-widening array of disciplines, ranging from the analysis of foodstuffs and medicine, to petroleum, geochemistry, and environmental monitoring. It is the foremost tool for the definitive analysis of volatile complex mixtures and, because of its unparalleled specificity, it has become the dominant referee method in analyses where ambiguous results have been obtained by more classical analytical procedures.

GC-MS represents the combination of two analytical techniques; gas chromatography (GC), which is a separations technique, and mass spectrometry (MS), which is an analysis technique. The strength of the GC-MS combination is attributable to the multi-dimensional capability created by both the high separation power of the gas chromatograph and the detection capacity of the mass spectrometer. The gas chromatograph separates the components of a volatile sample mixture and delivers relatively pure analyte to the mass spectrometer for analysis, while the mass spectrometer in turn analyzes each component with the specificity and sensitivity needed to provide both qualitative and quantitative analytical information.

Instrumentation for GC-MS has undergone a tremendous evolution over the past three decades. The need to evaluate increasingly complex samples, along with increases in

sample load, continues to drive the development of improved chromatographic technology. Modern chromatographic column technologies continue to yield higher-resolution separations in shorter time spans. Unfortunately, the concomitant temporal reduction in chromatographic peak width has not been accompanied by an increase in the detection bandpass of commercially available mass spectrometers. Consequently, these mass spectrometers are no longer the optimal chromatographic detectors for applications requiring both high chromatographic resolution and complete analytical analysis.

Given the current trend toward higher resolution chromatographic analyses, GC-MS will remain the predominant analytical methodology for the most modern applications only if improved MS technology is developed. As will be shown below, time-of-flight mass spectrometry (TOFMS) stands as the only detector technology presently capable of acquiring data at rates accommodating current and emerging chromatographic methods while retaining both high selectivity and sensitivity.

General Principles of GC-MS

The technique of gas chromatography, as applied to the analysis of organic compounds, is predominantly a form of partition chromatography in which the mobile phase is a gas and the stationary phase is a liquid coating on a column wall or other immobilized support. Once a sample mixture is injected into the carrier gas and volatilized, it is transported through the column where the chemically distinct sample components separate as a consequence of differences in their partitioning between the two phases, exiting the column sequentially in a process referred to as *elution*. As the chromatographically separated sample components emerge from the column end, they enter the vacuum of the mass spectrometer.

In the MS technique, sample molecules are ionized by one of several methods, the most common being electron bombardment. Upon ionization, many of the ions fragment from molecular size into various smaller ions and neutral species. The abundances of these ions are then determined as a function of their mass-to-charge ratio (m/z) and plotted in a histogram as relative abundance vs. m/z. This histogram, referred to as a *mass spectrum*, is a "fingerprint" of the compound, and is often unique. The abundances of ions originating from the same compound may also be summed to represent the quantity of that compound in the mixture. A plot of total ion abundance vs. time yields a *chromatogram* similar to that obtained by a single channel detector with each peak representing a particular component.

The Problem

Since the chromatographic behavior is ultimately characterized from reconstruction of MS data, the analytical performance of GC-MS depends on the capacity of the mass spectrometer to analyze the eluting chromatographic components at a rate sufficient to provide both qualitative and quantitative information with minimum uncertainty. The effect of an insufficient analysis rate is manifested in two ways; by *spectral skewing* and *chromatogram distortion*. Commercial mass spectrometers used as chromatographic detectors operate in a scanning mode where information about ion abundance is obtained exclusively and sequentially over the m/z range being examined. This information is then compiled into a single mass spectrum. Spectral skewing occurs if this finite scan time is significantly long in comparison to the rate of change in analyte concentration within the ionization chamber of the mass spectrometer. Here the relative abundances of the various

ions formed in the ionization process will be misrepresented, and a corrupt or skewed mass spectrum will be generated.

The relationship between the qualitative appearance of the mass spectrum and the rate of change in analyte concentration is illustrated in Figure 1-1. For unidirectional scanning, in this case from low m/z to high m/z, a mass spectrum acquired while the analyte concentration is increasing produces a spectrum having the intensities of peaks for higher m/z ions enhanced, whereas a spectrum acquired while the analyte concentration is diminishing exhibits relatively enhanced peak intensities for ions of low m/z. In both cases the qualitative appearance of the mass spectrum is misrepresented, making compound identification difficult, or even impossible. The correct mass spectrum is collected either during a time when the analyte concentration remains constant or when the scan speed is rapid compared to the elution dynamics, eliminating or at least minimizing any effect of changes in analyte concentration.

Fig
the
sca
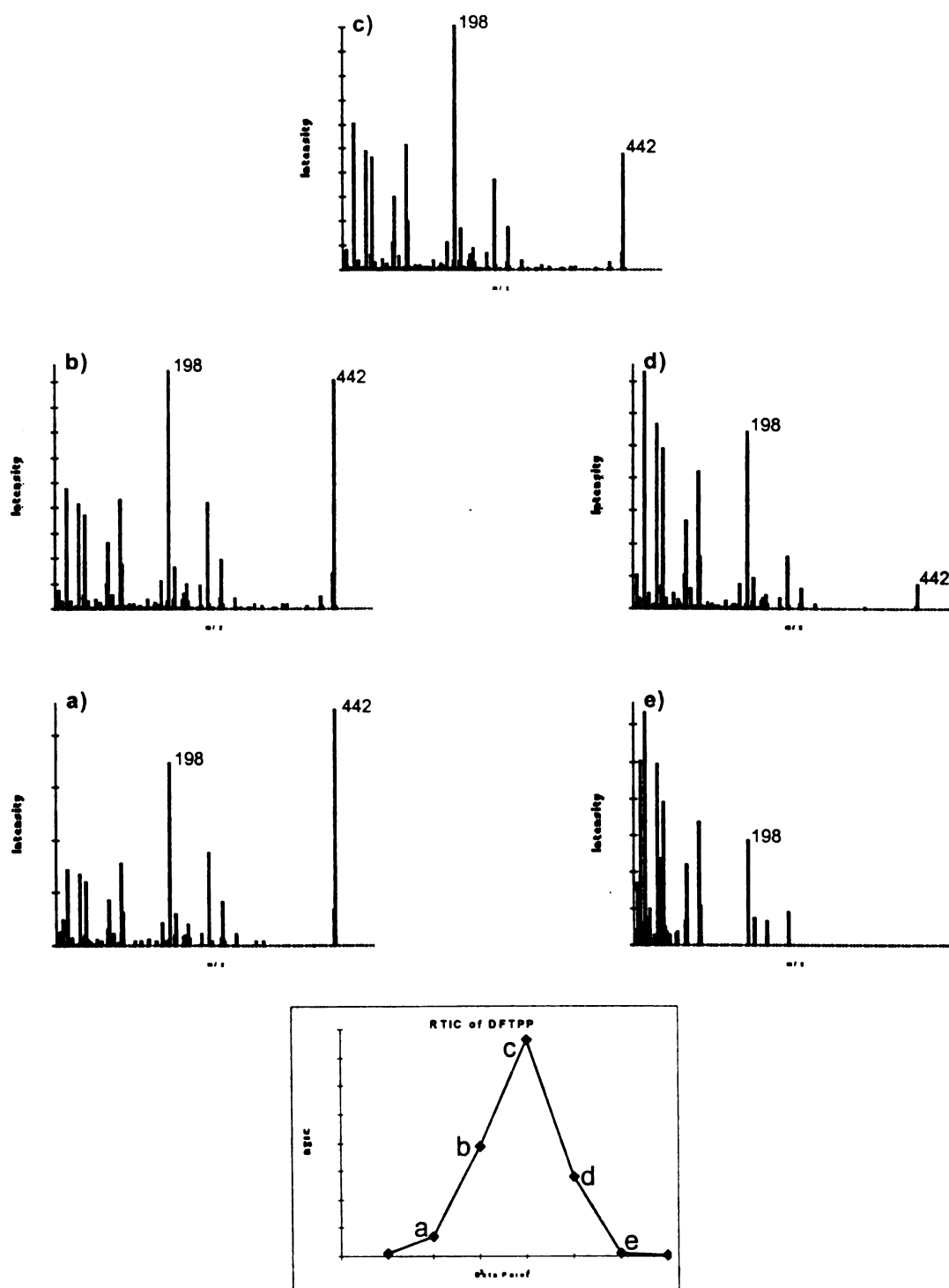
Figure 1-1. Reconstructed total ion chromatogram (RTIC) and five spectra illustrating the skewing of decafluorotriphenylphosphine (DFTPP) mass spectra when acquired on a scanning quadrupole mass spectrometer.

of

ge

ge

to

a

th

po

re

Ga

the

inf

sho

rep

exa

oth

be

sca

ma

ulti

The second problem, that of chromatographic distortion, relates to the reconstruction of the chromatogram. The optimal chromatogram used for quantitative purposes is generated from a continuous measurement of the analyte signal. A chromatogram generated from a scanning mass spectrometer, however, is constructed by summing the total or selected ion abundances measured during a single scan and assigning this value to a discrete elution time point. A spectral generation rate that is relatively slow compared to the temporal width of the eluting analyte will yield a distorted chromatogram which poorly describes the true elution profile of the sample.

The effect of an inadequate scan rate is illustrated in Figure 1-2. The chromatogram reconstructed from the scan-acquired data mistakenly identifies only a single non-Gaussian shaped peak and incorrectly defines its position on the time axis. Furthermore, the mass spectrum assigned to the apex of the reconstructed peak contains ion abundance information from two analytes. For isolated, Gaussian-distributed peaks, it has been shown that 10–12 data points must be collected across the peak in order to sufficiently represent the peak area for quantitation [1]. Many more data points are required when the exact elution time must be determined, and when the analyte must be distinguished from other partially co-eluting species [2].

The obvious solution to avoid spectral skewing or chromatographic distortion would be to scan at a sufficient rate. Unfortunately, the more rapidly a mass spectrometer is scanned, the less time is available for monitoring the ion abundance of each m/z in the mass range and the concomitant decrease in signal-to-noise ratio (S/N) diminishes the ultimate detection limit of the instrument. For reasonable levels of sensitivity and S/N, the
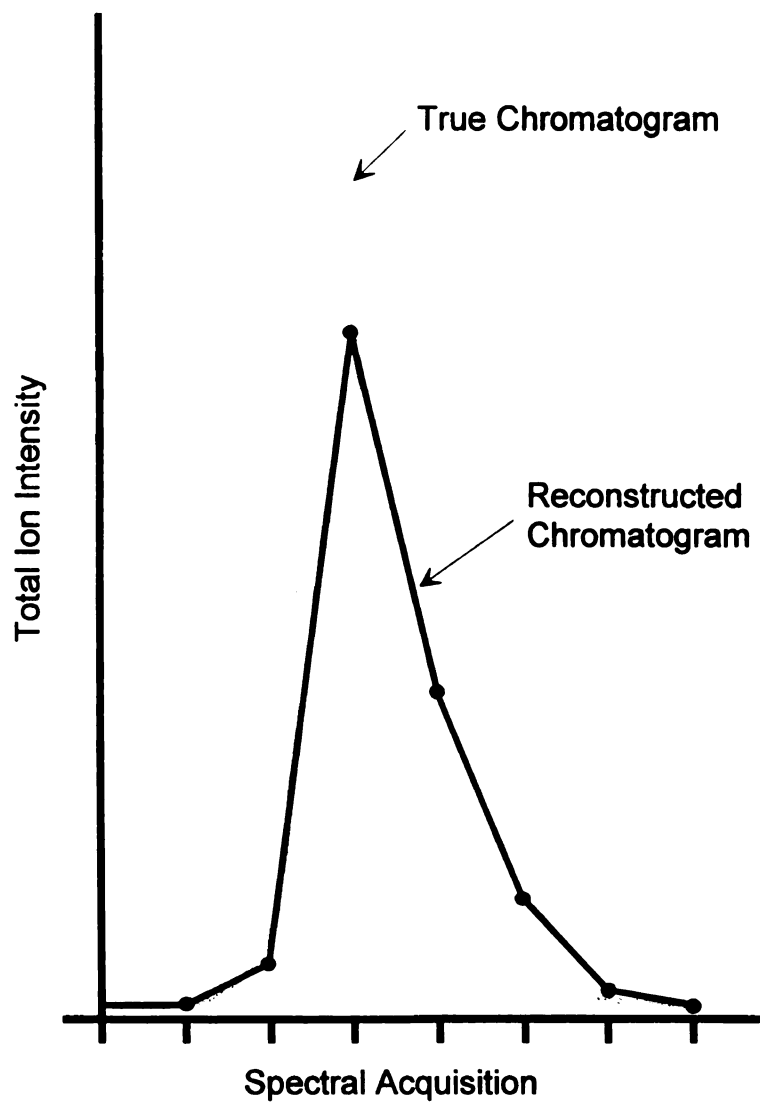
Figure 1-2. The effect of an inadequate spectral acquisition rate in reconstructing a true chromatographic profile. The gray line represents the actual chromatographic event while the black line represents the integration of the preceding acquisition interval.

maximum possible rates are: 1–2 scans/second for sector instruments, 2–5 scans/second for quadrupoles, and 5–10 scans/second for ion traps.

Two alternate methods are available which avoid this scan rate/performance tradeoff. First, the effective scan rate of a mass spectrometer can be increased by reducing the mass range being scanned. This has the effect of increasing the sampling rate of the ions within the range without diminishing the S/N. The second method incorporates the use of selected-ion monitoring (SIM), where the abundance of only a single or few select m/z's is monitored. This method provides a nearly continuous chromatographic profile and an enhanced detection limit compared with scanning, due to the increased S/N that arises from spending more time on the selected m/z measurements. As the mass to charge ratios chosen for monitoring must be pre-selected, however, the method is limited to the analysis of known compounds. For both methods, the primary drawback is that little or no information is available to identify unknown or unexpected compounds since most of the mass spectral information has been sacrificed.

The ideal solution to both the skewing and reconstruction problems would be to incorporate a non-scanning MS technique that simultaneously monitors the entire selected m/z range. By this method, known as *array detection*, the mass spectrometer would provide the increased S/N associated with SIM over the entire mass range being examined and the qualitative appearance of the mass spectra would be preserved.

(

r

t

t

o

av

ar

di

wa

the

tim

of

incr

sequ

A Historical Perspective

Given that current commercial GC-MS systems utilize MS techniques relying exclusively on scanning rather than array detection methods, it is interesting to note that the feasibility of GC-MS was first demonstrated in 1959 using an instrument that was capable of array detection—the time-of-flight mass spectrometer [3]. This mass spectrometer could monitor ions at rates in excess of 2000 per second and, as an array detector, eliminate any possibility of spectral skewing.

The major limitation to the technique at that time was the absence of a suitable data collection method. Mass analysis in time-of-flight mass spectrometry is accomplished by measuring the arrival times of ions striking the detector at the end of their "flight" through the mass spectrometer. The brief duration of the generated signal, referred to as a *transient* or transient waveform, may be as little as 100 μs for the entire mass range observed and only 10 ns for the ions representing a single m/z. The only electronic device available to monitor the output signal in these time-scales in 1959 was the oscilloscope, and mass spectral information could only be recorded by photographing the oscilloscope display.

By the early 1960s, a method of data collection using time-gated boxcar integration was developed. This method is known as *time-slice detection*, whereby a small portion of the information available in each transient is measured and recorded. By creating a fixed time delay prior to data collection from successive ion source extractions, the abundance of a single m/z could be continuously monitored. Alternatively, by incrementally increasing the delay prior to data collection from successive extractions, data for a sequentially generated (i.e. scanned) mass spectrum could be obtained [4]. The

implementation of time-slice detection reduced the effective spectral generation rate enough to enable the possibility of data recording by conventional methods. As a result, however, the advantages of array detection were sacrificed as the instrument was converted to a scanning device. The lack of a suitable data collection method combined with poor overall instrument performance and small dynamic range led to the eventual abandonment of TOF in favor of other MS techniques for GC applications, and few publications reporting the use of GC-TOFMS have since been reported [5–13].

Other mass analyzers, namely the magnetic sector and the quadrupole, have been more successfully coupled with GC. Magnetic-sector mass spectrometers were first coupled with GC in the early 1960s [14], and were capable of acquiring mass spectral information at rates ranging 0.1–1 scans per second. These rates were sufficiently fast to accurately detect packed-column eluates and slow enough to be recorded with a galvanic chart recorder. The development of the quadrupole mass spectrometer in the late 1960s helped generate significant interest in GC-MS by providing an economical instrument which had adequate sensitivity and mass resolution and was readily adapted to computers for instrument control and data acquisition [15]. The 1–2 scans per second acquisition rates available with these mass spectrometers made them well suited for use with open-tubular capillary columns which yield eluting times of only a few seconds. By the mid 1970s, GC-MS systems predominantly used quadrupole technology with acquisition rates of up to 5 scans per second and adequate sensitivity. More recently, the development of the quadrupole ion trap has further increased the spectral acquisition rates available by scanning mass spectrometers, with rates of 2–10 scans per second readily achievable.

e

t

r

cl

de

co

id

inf

nar

Chr

to c

type

tech

dete

suffic

The MSU Connection

Researchers at Michigan State University were first confronted with the limitations of commercial GC-MS technology in the early 1980s while investigating urinary organic acid metabolites in humans [16]. The experimental protocol in this "metabolic profiling" research yielded highly complex samples, components of which often partially co-eluted with other species. The initial investigations utilized packed columns in which the major components could be effectively analyzed because their eluting times were long relative to the mass spectrometer scan time.

A more thorough analysis of the urinary metabolites became possible as high-resolution capillary columns became available. Many more components could be chromatographically resolved using these columns, but the possibility of using MS detection was reduced as a consequence of the shorter elution times. While known components could be identified by chromatographic retention index using GC alone, the identification of unknown compounds, which required the obtaining of structural information by MS, was precluded in cases where the unknown analyte was temporally narrow or partially co-eluting with other compounds.

These researchers published a paper in 1983 entitled "Mass Spectrometry on the Chromatographic Time Scale: Realistic Expectations" describing the difficulties inherent to chromatographic detection by mass spectrometry [17]. In this publication the various types of mass spectrometers were examined and the attributes of scanning and array techniques for chromatographic detection compared. The authors concluded that array detection was the only method capable of collecting complete mass spectra at rates sufficient to provide both unskewed spectra and accurate chromatographic representation

for high-resolution capillary column GC-MS. Time-of-flight mass spectrometry, using its inherent capacity for array detection, was identified as the best suited candidate, having a potentially high spectral generation rate in addition to a wide dynamic range, adequate mass range, and reasonable cost. Consequently, MSU researchers devised a plan to accomplish GC-TOFMS with the goal of achieving a 100-Hz spectral generation rate over the range m/z 50–500 [18].

Part One of the Plan – Instrumentation For Time Array Detection

The first part of this plan addressed the same limitation that TOFMS faced when it was first used for GC-MS in 1959; namely the lack of appropriate data acquisition hardware. Maximal usage of the ion abundance information available in each TOFMS transient is obtained only when the entire generated transient signal is recorded; an acquisition method known as *time-array detection* (TAD).

Research at MSU has resulted in the design and construction of an integrating transient recorder (ITR) capable of continuously acquiring up to 10,000 complete transients per second [19,2021]. The ITR provides both high-speed data acquisition and time-array detection across the entire selected mass range. Furthermore, several successive transients can be summed in a time-locked registry to yield an integrated spectrum which is then electronically stored. This significantly reduces the overall data storage space requirement while maintaining the desired spectral generation rate for GC-MS and improves the S/N of each spectrum by a factor equal to the square root of the number of transients summed.

a

s

r

T

H

in

gr

si

ne

ad

ma

ea

wit

Fac

GC

Part Two of the Plan – Improvements to Mass Resolving Power

The second part of the MSU plan involved the development of a time-of-flight mass spectrometer capable of providing mass spectral information of sufficient quality to enable the use of TAD. The analysis of gas phase ions by TOFMS necessarily incorporates spatial and energetic variations which potentially diminish the mass resolving power. This resolving power, which is described more thoroughly in chapter two, is the capacity to distinguish ions of differing m/z and is increasingly difficult to achieve at higher m/z, eventually limiting the effective mass range of the mass spectrometer. Many early time-of-flight instrumental configurations utilized ion focusing methods for achieving sufficient mass resolution that are, unfortunately, mass-dependent. These methods resolve only a small portion of the analyzed mass range in each transient. However, the use of TAD requires mass-independent ion focusing, as ion abundance information over the entire mass range is collected with each and every transient.

Furthermore, these mass-dependent focusing techniques typically employ a low gradient electric field to initially extract ions from the ionization chamber, creating a situation where the effect of collisional broadening, due to the interaction of the ions with neutral molecules, further diminishes the achievable mass resolving power [22]. An adequate TOF mass spectrometer for GC-MS using TAD should provide at least unit mass resolution by a mass-independent ion focusing means over the entire mass range in each and every transient and minimize the effects of the collisional broadening inherent with gas chromatographic sample introduction. Research in the MSU Mass Spectrometry Facility has led to the development of such a TOF mass spectrometer for use in GC-MS [23].

Research Goals

As the development of the technology required to fulfill the plan initiated in 1983 nears completion, consideration must now be given to extending the use of TOFMS to other separation techniques such as liquid chromatography (LC) and capillary zone electrophoresis (CE) which share the same requirements for adequate mass spectrometric detection as GC, but utilize sample introduction techniques that are distinctly different. Specifically, these methodologies produce large sample volumes in the gas phase and thus place stringent requirements on ion source design and performance.

This dissertation describes, along with the development of the time-of-flight mass spectrometer designed for use in GC-MS with TAD, the development of an ion source which allows the study of the basic phenomena limiting mass resolving power; especially those phenomena which would be deleterious when sampling large ion volumes. Chapter 2 contains a discussion of the fundamental principles of mass analysis by time-of-flight mass spectrometry and the major instrument configurations that have been developed to provide improved mass resolving power. A description of the novel TOFMS system collaboratively developed at MSU is contained in Chapter 3 along with discussion of ion source developments and limitations. The core research of this author, the development of an ion acceleration model and an ion source that compensates for spatial variations in initial ion position is described in Chapter 4.

Chapter References

1. Enke, C. G.; Watson, J. T.; Allison, J.; Holland, J. F. In *Proceedings of the 37th ASMS Conference on Mass Spectrometry and Allied Topics*, Miami Beach, Florida, May 21–26, **1989**, 32.

2. Chesler, S. N.; Cram, S. P. *Anal. Chem.* **1971**, *43*, 1922.

3. Gohlke, R. S. *Anal. Chem.* **1959**, *31*, 535.

4. Gohlke, R. S. *Anal. Chem.* **1962**, *34*, 1332.

5. Ebert, Jr., A. A. *Anal. Chem.* **1961**, *33*, 1865.

6. McFadden, W. H.; Teranishi, R.; Black, D. R.; Day, J. C. *J. Food Sci.* **1963**, *28*, 316.

7. D'Oyly-Watkins, C.; Hillman, D. E.; Winsor, D. E.; Ardrey, R. E. In *Dynamic Mass Spectrometry*, Price, D.; Williams, J. E., Eds., Heydon & Son Ltd.: London, 1970; Vol. 1, pp 163–174.

8. Kirchgessner, W. G.; DiPasqua, A. C.; Anderson, W. A.; Delaney, G. V. *J. Forensic Sci.* **1974**, *19*, 313.

9. Dobson, R. L. M. *Energy Res. Abstr.* **1986**, *11*, Abstr. No. 41188.

10. Dobson, R. L. M.; D'Silva, A. P.; Weeks, S. J.; Fassel, V. A. *Anal. Chem.* **1986**, *58*, 2129.

11. Erickson, E. D.; Enke, C. G.; Holland, J. F.; Watson, J. T. *Anal. Chem.* **1990**, *62*, 1079.

12. Watson, J. T.; Schultz, G. A.; Tecklenburg, R. E.; Allison, J. *J. Chrom.* **1990**, *518*, 283.

13. Wilkerson, C. W.; Colby, S. M.; Reilly, J. P. *Anal. Chem.* **1989**, *61*, 2669.

14. Lindeman, L. P.; Annis, J. L. *Anal. Chem.* **1960**, *32*, 1742.

15. Finnigan, R. E. *Anal. Chem.* **1994**, *66*, 969A.

16. Holland, J. F.; Leary, J. L.; Sweeley, C. C. *J. Chrom.*, **1986**, *397*, 3.

17. Holland, J. F.; Enke, C. G.; Allison, J.; Stults, J. T.; Pinkston, J. D.; Newcome, B.; Watson, J. T. *Anal. Chem.* **1983**, *55*, 997A.

18. Allison, J.; Holland, J. F.; Enke, C. G.; Watson, J. T. *Anal. Instrum.* **1987**, *16*, 207.

19. Holland, J. F.; Newcome, B. N.; Tecklenburg, R. E.; Davenport, M.; Allison, J.; Watson, J. T.; Enke, C. G. *Rev. Sci. Instrum.* **1991**, *62*, 69.

20. Enke, C. G.; Holland, J. F. *United States Patent* No. 4,490,806, **1984**.

21. Holland, J. F.; Enke, C. G.; Davenport, M. R.; Janow, L. W. *United States Patent* No. 5,367,162, **1994**.

22. Futrell, J. H.; Tiernan, T. O.; Abramson, F. P.; Miller, C. D. *Rev. Sci. Instrum.* **1968**, *39*, 340.

23. Grix, R.; Tecklenburg, Jr., R. E.; Watson, J. T.; Holland, J. F.; Yefchak, G. E.; Gardner, B. D.; Allison, J.; Enke, C. G.; Wollnik, H. In *Proceedings of the 39th ASMS Conference on Mass Spectrometry and Allied Topics*, Nashville, Tennesee, May 21–26, **1991**, 154.

CHAPTER 2

THEORY AND INSTRUMENTATION DEVELOPMENT IN TIME-OF-FLIGHT MASS SPECTROMETRY

Introduction

In the most common form of time-of-flight mass spectrometry, ions created in the vacuum of an ion source are accelerated to constant energy and allowed to drift along an evacuated field-free flight tube where they separate into groups according to their mass-to-charge ratio (m/z), as shown in Figure 2-1. The time required for an ion extracted from the source to reach the detector is measured and used to calculate mass. This relationship between time (or velocity) and m/z can be explained in the following manner. The force F, exerted on an ion by an electric field is given by

$$F = qE = zeE \tag{2-1}$$

where E is the electric field given in volts/cm, and q, the charge on the ion (in coulombs) is the product of e, the elementary unit of charge, and z, the number of unit charges. The kinetic energy gained by an ion is equal to the work W performed on the ion by the electric field, and may be represented as

$$KE = W = F \cdot d \tag{2-2}$$

where d is the distance the ion travels through the electric field. Consequently, substituting the previous equations, it is shown that
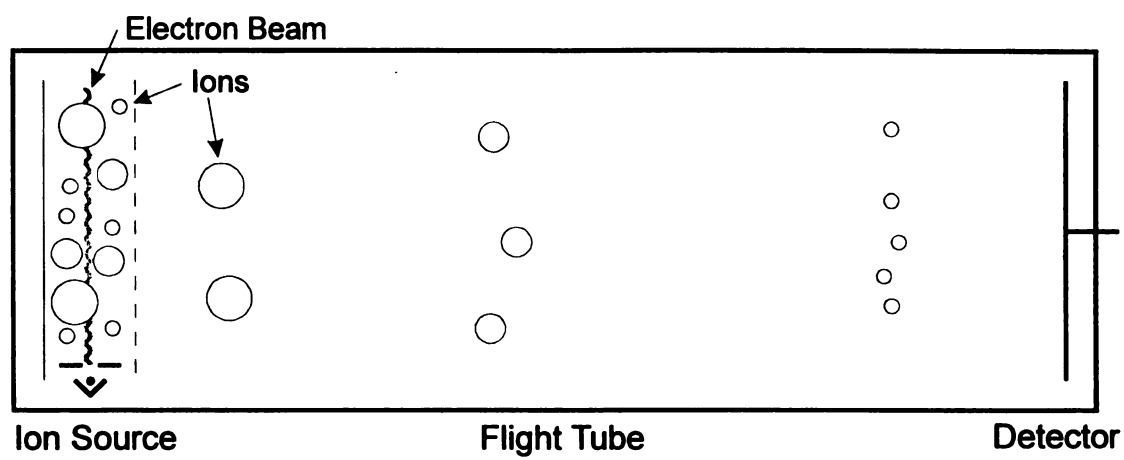
Figure 2-1. Conceptual diagram of *m/z* analysis by time-of-flight mass spectrometry.

$$KE = zeEd \tag{2-3}$$

The velocity of an ion may be found by incorporating the classical equation for kinetic energy

$$KE = \frac{1}{2}mv^2 \tag{2-4}$$

where m is the ion mass, and v is the velocity. Equations 2-6 and 2-7 can be combined and rearranged to solve for velocity

$$v = \sqrt{\frac{2zeEd}{m}} \tag{2-5}$$

which upon further rearrangement, and substitution of distance and time for velocity, it can be shown that

$$t = \frac{D}{\sqrt{2eEd}}\sqrt{\frac{m}{z}} \tag{2-6}$$

where t is the time of flight, and D is the flight distance from the ion source to the detector surface. This can be further simplified to

$$t = k\sqrt{\frac{m}{z}} \tag{2-7}$$

where k is the collection of constant values. Empirically, the measured flight time t_{meas} is

$$t_{meas} = t_{offset} + k\sqrt{\frac{m}{z}} \tag{2-8}$$

where t_{offset} is the offset time to account for any delays imposed by the measurement circuitry. This first-order relationship between time and $\sqrt{m/z}$ provides for a simple calibration of the time-of-flight mass spectrometer.

Early Development of TOFMS

The concept of time-of-flight mass spectrometry was first envisioned in 1946 by Stephens [1] as a means for monitoring chemical systems in which the composition was changing rapidly as a function of time. The first development of a TOF instrument was reported in 1948 by Cameron and Eggers [2], and was followed by reports on other instruments, including those developed by Keller in 1949 [3], by Wolff and Stephens in 1953 [4] and by Katzenstein and Friedland in 1955 [5]. These instruments provided high spectral generation rates of up to 5000 Hz, but exhibited poor sensitivity and were unable to distinguish between ions greater than m/z 100. TOFMS became a practical technique only through the innovations of Wiley and McLaren in 1955 [6] which extended the mass resolving power, and a commercially produced instrument based on their design became available from the Bendix Corporation in 1956 [7].

In spite of these developments however, TOFMS quickly became known as a technique of limited capacity, ideal only for some custom applications, and generally fell out of favor in the analytical laboratory as other types of mass spectrometers having higher resolving power and greater detectability were developed. Expanded interest in TOFMS did not revive until the mid 1970s with two developments; 1) plasma [8] and laser desorption techniques in which, through pulsed ionization of an analyte on a planar surface, some of the factors limiting mass resolving power could be eliminated, and 2) the

ion mirror or "reflectron" by Mamyrin [9] which could compensate in a mass-independent manner for the energetic limitations to mass resolving power.

The Need for Resolving Power

Throughout the development of TOFMS, the improvement of mass resolving power has been a primary objective. The need for this is three-fold. First, the resolving power determines the extent to which ions having different m/z may be differentiated by the mass spectrometer, which in turn affects the extent to which an analyte can be defined by its mass spectrum. Secondly, the m/z range is largely affected by the resolving power. For gas chromatographic applications a mass range requirement of 1–600 u is desirable, and GC applicable analytes can range up to 1000 u. For liquid chromatography, analytes of up to 2500 u are observed and for other applications such as laser desorption, a mass range of 10,000 u or more may be required. Finally, with time-of-flight there is a unique relationship between resolving power and detectability. Other forms of mass spectrometry enhance the resolving power by removing ions having a slight difference in m/z or in energy than those ions of interest. Consequently, ion transmission is decreased and detectability is diminished. In time-of-flight mass spectrometry there is a direct correlation between resolving power and detectability, meaning that as the resolving power is increased, the temporal distribution of each iso-mass ion population becomes more narrow and there is actually an increase in S/N as shown in Figure 2-2.
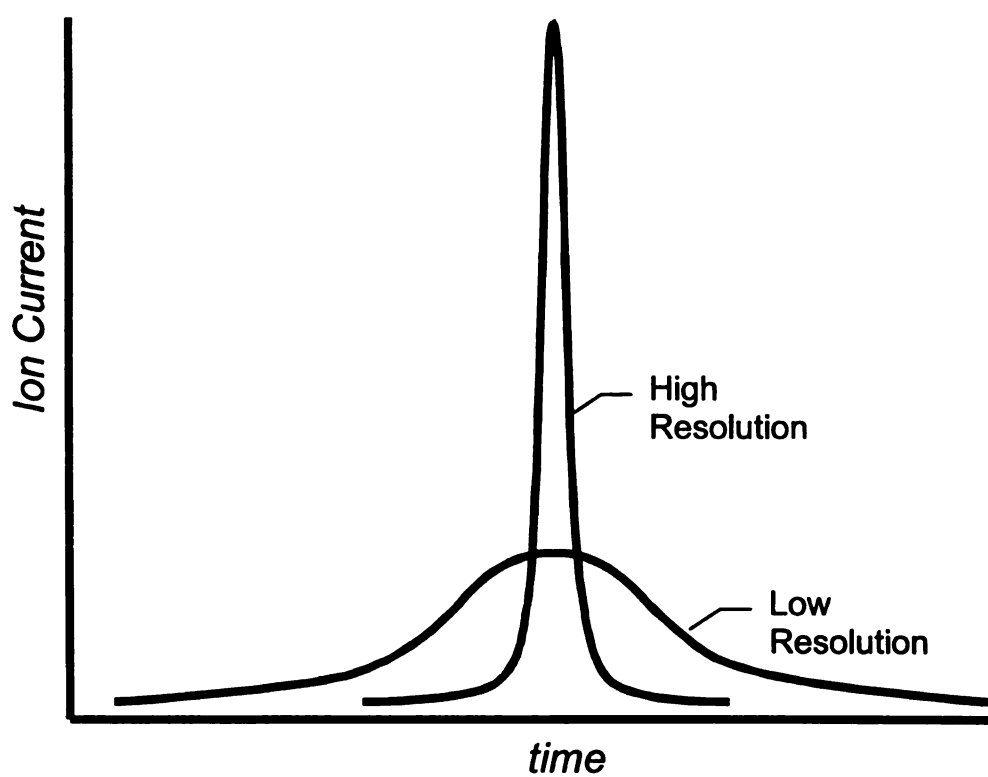
Figure 2-2. Comparison of ion temporal distribution under low and high resolution conditions. For time-of-flight mass spectrometry, in contrast with other mass spectrometric forms, as the temporal distribution is narrowed, the *S/N* increases.

Definitions of Resolving Power and Mass Resolution

There are several related definitions defining the term resolving power, R, but only two methods, as illustrated in Figure 2-3 are common. The first method, or "mass method," is derived from a plot of ion intensity versus m/z, and is defined as

$$R = \frac{m}{\Delta m} \qquad (2\text{-}9)$$

where m is the m/z of the peak being examined ($z = 1$) and Δm is defined as

$$\Delta m = \frac{d_m}{d_{(m+1)-m}} \qquad (2\text{-}10)$$

where $d_{(m+1)-m}$ is the measured distance between adjacent m/z peaks and d_m is the peak width at an amplitude defined as a percentage of the peak height. Typically, this amplitude is defined as 50%, or *full width at half maximum* (FWHM).

The second method, or "time method," is derived from a plot of ion intensity versus time, and is defined as

$$R = \frac{t}{2\Delta t} \qquad (2\text{-}11)$$

where t is the average ion flight time of the m/z peak, and Δt is the arrival time distribution at a defined percentage of the peak height. In practice, when equivalent peak height percentages are used, the results of equations 2-1 and 2-3 are equal.
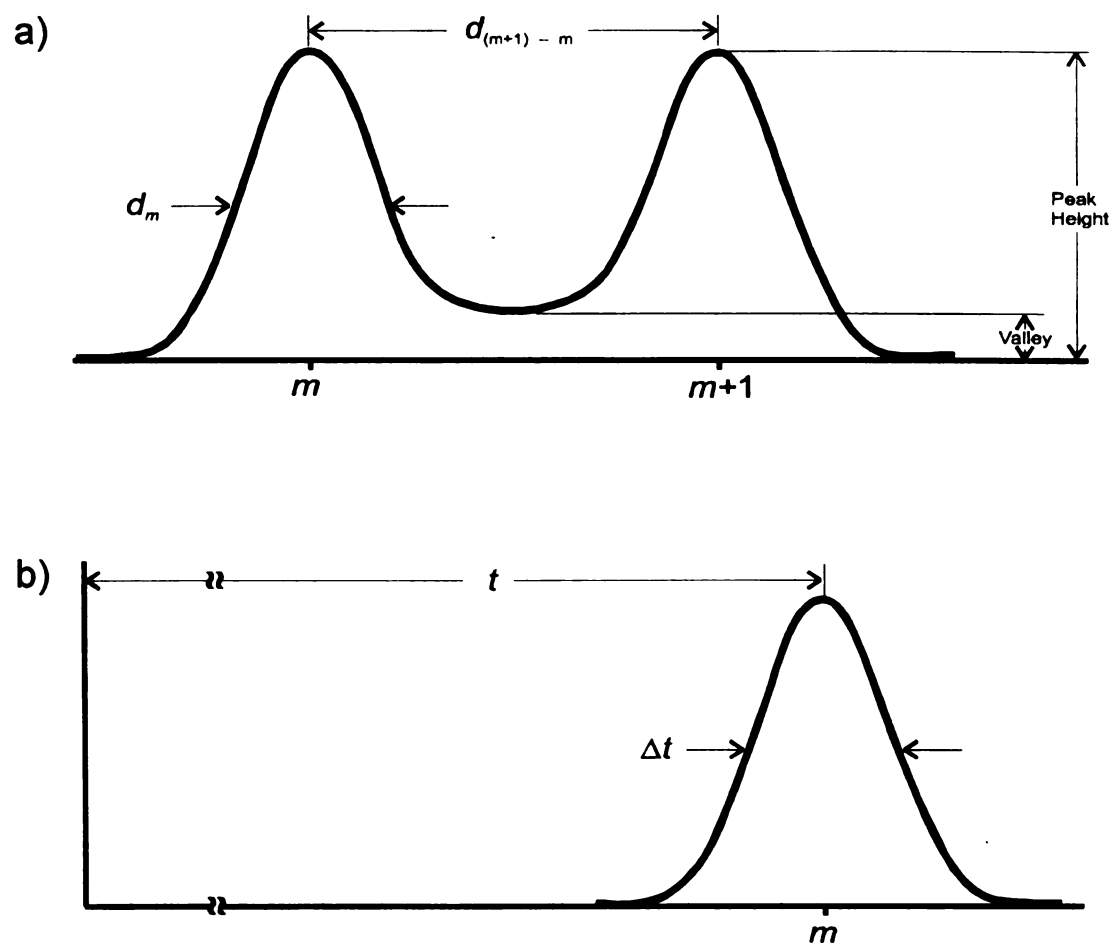
Figure 2-3. Measurement of mass resolving power by a) the mass method, and b) the time method.

Two other terms are also used in defining *m/z* differentiation: resolution and unit mass resolution. *Resolution* is inversely related to resolving power. A mass spectrometer having a resolving power of 500 has a resolution along the mass axis of one part in 500. The term *unit mass resolution* is used to define the maximum *m/z* for which the peak is separated from adjacent peaks. The separation is determined by the percent valley or overlap between the peaks; typically 10%.

Problems Limiting Resolving Power

In principle, nearly infinite resolving power could be attained if all ions in each iso-mass group would arrive at the detector simultaneously. And while this ideal circumstance could be achieved if 1) all the ions possessed identical (or no) internal energy or motion; 2) all started from the same point, and 3) all were accelerated to identical kinetic energy, any one of these conditions is rarely achieved and the resolving power is consequently diminished. Therefore, some mechanism or combination thereof must be used to compensate for the effects of variations in ion starting conditions in order attain sufficient resolving power.

For a gaseous sample, there is both a distribution of initial ion starting positions and a thermal Maxwell-Boltzman distribution of ion energies (~0.1 eV) that is manifested as a distribution of ion detection times within each iso-mass group. The manifestations of these distributions are often referred to as the *space* and *energy effects*. The energy effect also has a distinct detrimental component known as the *turn-around effect*, whereby those ions having a thermal energy vector directed against the accelerating field travel away from the ion source exit before being turned around. This results in ions of the same *m/z*,

same initial position, and same magnitude of thermal energy, exiting the ion source at different times and consequently leading to a difference in arrival-times at the detector.

The three ion starting parameters are modeled in Figure 2-4. The effect of each case can be compared with the reference ion of the same mass located at the initial position s_0, with no internal energy. The energy, U_{s_0}, applied to the reference ion is

$$U_{s_0} = s_0 E \tag{2-12}$$

which represents the total kinetic energy of the reference ion. It is assumed that ions originating from the same plane, orthogonal to the flight axis, receive equal kinetic energy when the accelerating field is applied.

In the first case S, an ion initially located at a position $s_0 + \delta s$, receives a total energy directly proportional to its initial position when the accelerating electric field is applied. The energy applied to this ion will differ from U_{s0} by the relationship

$$U_s = \frac{s_0 + \delta s}{s_0} U_{s_0} \tag{2-13}$$

Ions located farther from the ion source exit receive greater energy than those ions closer to the exit and overtake the less energetic ions at a distance $2s_0$ from the ion source exit; a phenomenon known as *space focusing*. The location along the flight axis where this occurs, in this case $2s_0$, is traditionally known as the *space focus plane* and represents the position along the flight path where R_s, that portion of the resolving power attributable to space focusing, is the highest. (The fact that the space focus plane is not an infinitely thin plane, but rather a region where ions exhibit a temporal minimum is the basis for the research described in Chapter 4.)

In the case of U+, an ion having some initial energy δU directed toward the detector is compared to the reference ion located in the same plane. While both ions receive a total energy of U_s as a consequence of their location within the source, the ion having the initial thermal motion leaves the source with a final energy of $U_s + \delta U$, achieves a greater velocity and arrives at the detector before the reference ion. Methods correcting for this variance are known as *energy focusing* methods, discussed below. In the special case of U–, the initial energy δU is directed away from the detector, and the ion initially travels against the electric field before being turned around and accelerated out of the source. For two ions of the cases U+ and U– where both ions have the same magnitude of internal energy but in opposite directions, each ion will leave the source with identical energy. However, the U– ion will arrive at the detector later due to the *turn-around time* in the ion source.

The resolving power is independently degraded by each of the starting parameters, with the overall resolving power representing the combined effect of the space and energy resolutions. The total resolving power, R, is defined as

$$\frac{1}{R} = \frac{1}{R_S} + \frac{1}{R_{U+}} + \frac{1}{R_{U-}} + \frac{1}{R_{electronics}} \qquad (2\text{-}14)$$

While not a fundamental parameter of ion motion, the term $R_{electronics}$ is included here to acknowledge that in practice, if all ion space and energy effects can be corrected or eliminated, the ultimate limitation to R is that imposed by the speed and precision of the detector and electronics circuitry.
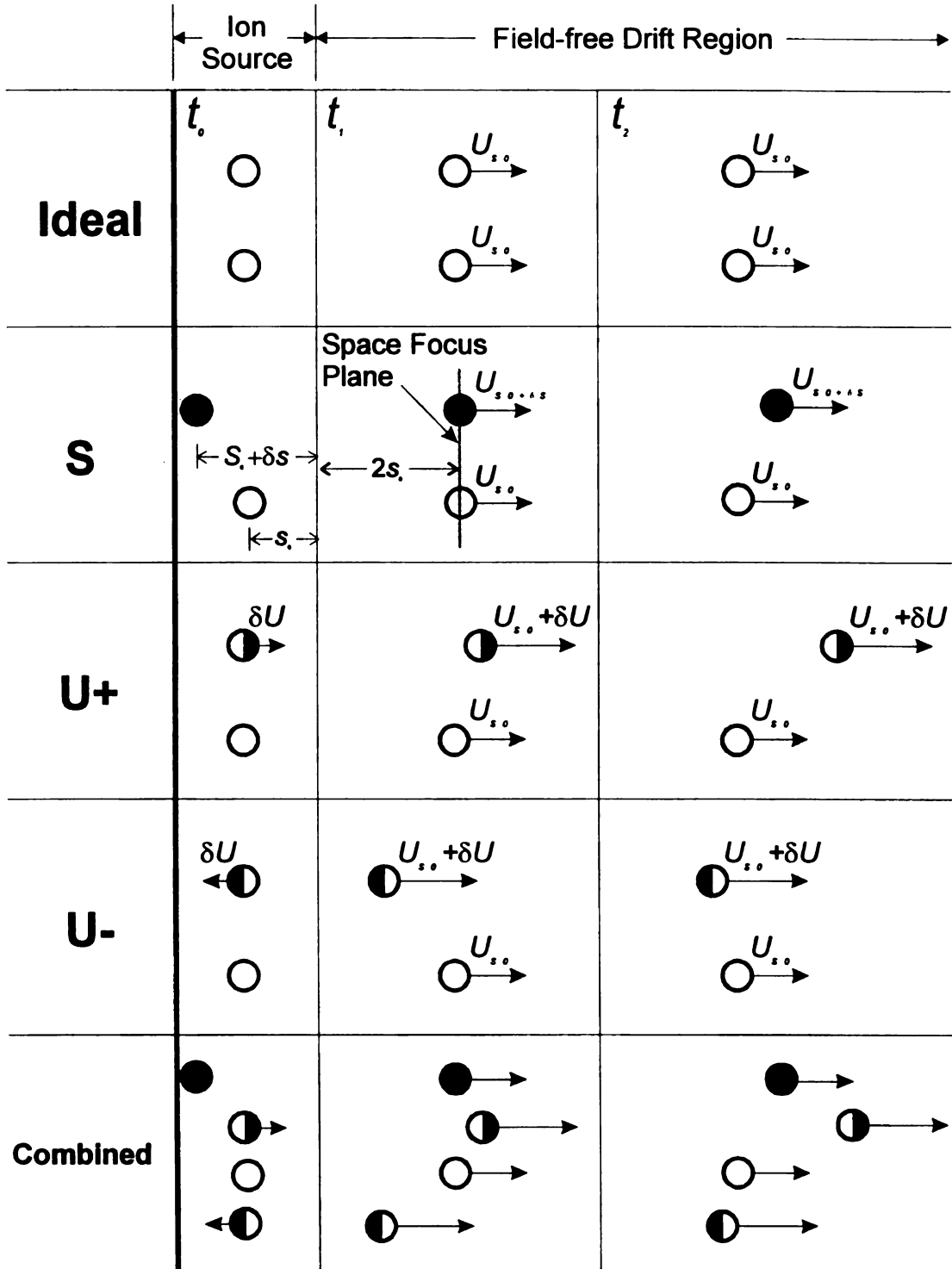
Figure 2-4. Models of ion behavior patterns leading to diminished resolving power, where ions initially located beyond s_0 (●) or possessing thermal energy (◑,◐) are compared with a reference ion (○). Arrows indicate direction and relative magnitude of thermal energy. Relative positions are shown at three times: that of ion formation (t_0), arrival at the space focus plane (t_1), and later in the field-free region (t_2). Adapted from [10,11].

Methods for Improving Resolving Power

The Wiley/McLaren Ion source

The first major improvements to resolving power were accomplished by Wiley and McLaren [6], who incorporated two design features that yielded vastly significant improvements to both mass resolving power and overall mass range. Their first innovation was the development of the two-field ion source. Earlier ion sources used a single electric field for ion extraction that imposed a tradeoff between energy and space focusing. In order to maximize energy resolution, it was desirable to use a high electric field strength and accelerate the ions to their final velocity quickly. However, this required an axially short ion source geometry, and as the detector must consequently be placed only a short distance $(2s_0)$ from the ion source in order to achieve a space focus condition, little time was available for mass separation. The total flight time could only be increased by either lowering the electric field strength (and consequently the energy resolution), or lengthening the flight path by moving the detector well beyond the space focus region. Since the dominant parameter limiting resolving power was the initial energy spread, the latter option was required. Wiley and McLaren found that by using a two-field ion source, illustrated in Figure 2-5, the space focus region could be located farther than $2s_0$ from the ion source at a distance which is a function of the two accelerating electric field strengths. Thus, while the low amplitude first accelerating field slightly reduced the energy resolution, the ability to achieve both space focusing and an increase in the total flight time for all ions yielded an overall increase in R.
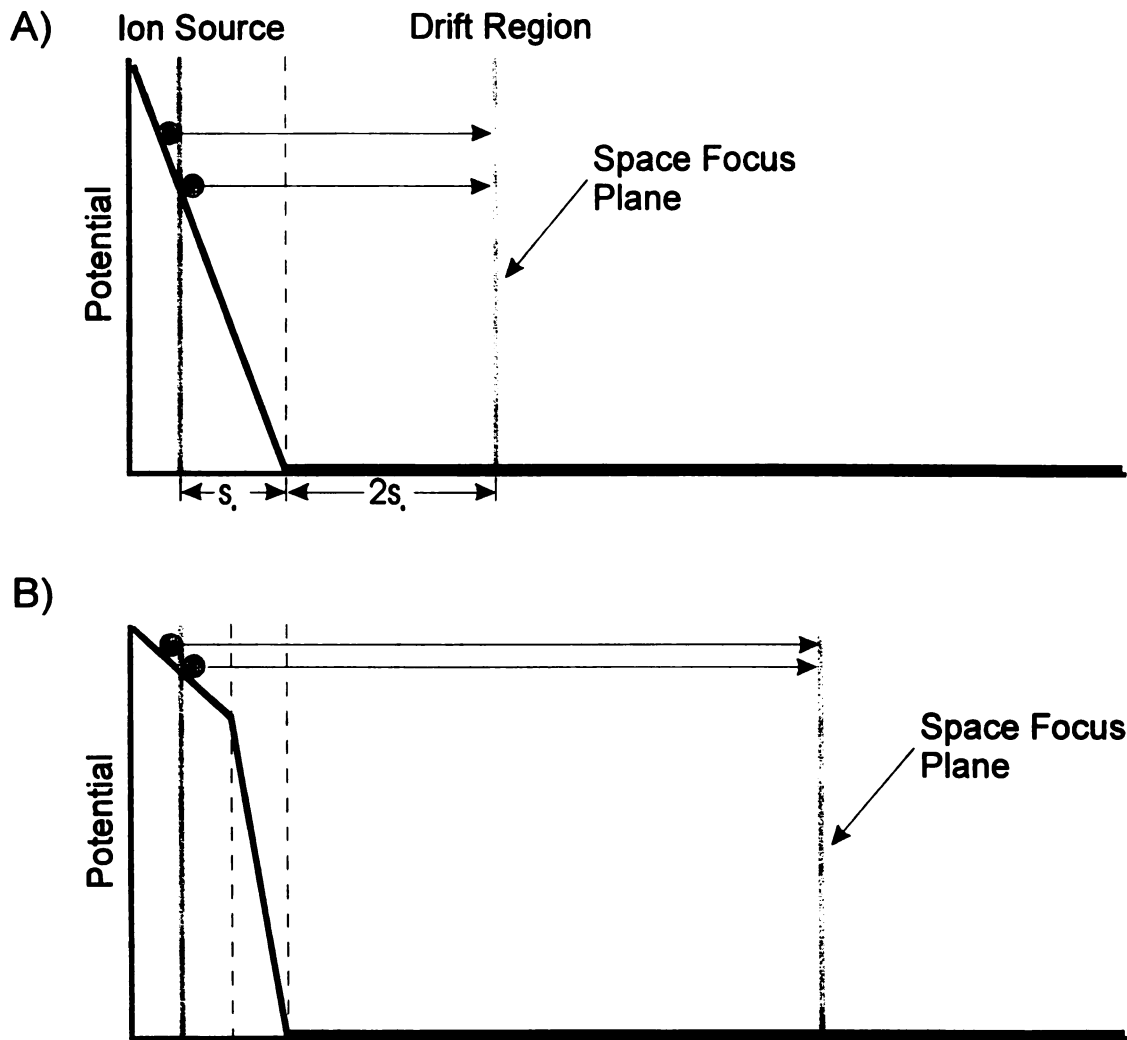
Figure 2-5. Comparison of single (A) and dual field (B) ion accelerating methods. The dual field method allows the space focus plane to be located beyond the $2s_0$ position.

Wiley and McLaren's second innovation provided additional focusing by introducing an adjustable time delay between the formation of ions and the application of the accelerating field. During this time, ions move to new locations in the ion source due to their thermal energies and, upon extraction, receive total kinetic energies dependent on these new locations. This energy focusing method, known as *time-lag focusing*, essentially attempts to transform the energy distribution of the initial ion population into a spatial distribution, thus reducing the temporal effect of the energy distribution at the space focus plane. Unfortunately, the optimal time lag is mass dependent, requiring that the lag time be varied with successive extractions in order to record a wide mass range. However, using these methods, Wiley and McLaren increased the mass resolving power to ~300, with the turn-around effect becoming the dominant limiting factor.

Subsequent Ion Source Methods for Improving Resolving Power

Since the work of Wiley and McLaren, a number of approaches have been pursued in an attempt to compensate for the initial energy spread in electron impact ion sources. Sanzone proposed a multiple-field ion source to provide both space focusing and compensation for the turn-around effect, but theoretical analysis indicated that no improvement to mass resolving power could be expected beyond that provided by the Wiley-McLaren two-field model [12]. Marable and Sanzone later attempted to minimize the turn-around effect with the technique of impulse-field focusing (IFF) [13], in which a short duration, high amplitude electric field pulse was applied to the ionization region just prior to the extraction pulse. This initial pulse added a bias to the thermal energy distribution of the ion population, causing all ions to move toward the ion source exit prior to extraction and, in essence, reduce the effect of the initial energy distribution on

mass resolving power. While Sanzone and coworkers obtained some initial results using this technique and were able to achieve a mass resolving power of 450, pursuit of this technology was limited by an inability to create voltage pulses of sufficiently short duration and large amplitude [14].

Sector Focusing

Other methods for energy focusing have been proposed using magnetic sectors [15] and electric sectors [16–18]. Several of these designs have been constructed, including one incorporating a toroidal electric sector and two field-free regions [19], and another incorporating four tandem electric sectors and having a reported resolving power of ~700 [20,21].

An electric sector has also been used in energy filtering [22]. In this instrument, an ion beam generated from a continuous source was directed into an electric sector. A narrow energy range of ions was then directed into a time-of-flight mass analyzer, converted into discrete ion packets using a beam modulation technique, and mass analyzed. The use of a continuously generated ion beam eliminated the turn-around effect associated with pulsed ionization and the filtering minimized the total energy spread. However, while this technique yielded resolving powers of up to 900, ion transmission was diminished. In an effort to regain ion transmission, beam modulation was used to introduce ion packets into a time-of-flight instrument directly from a continuous ion source [23] without energy filtering. While transmission improved, this instrumental configuration achieved a resolving power of only 700.

Dynamic Fields

In contrast with using static electric or magnetic fields, it is also possible to use dynamic fields, whereby the potential applied to some portion of the flight path is varied over time. Muga [24] proposed a velocity compaction technique in which a synchronized, continuously increasing potential is applied to the drift region subsequent to ion extraction. This increases the velocity of all ions as they travel toward the detector. However, those ions farthest from the detector in a given iso-mass packet experience a greater increase in energy, allowing them to catch up to those ions closer to the detector, and thus decrease the temporal distribution of the ion packet. Yefchak [25] modeled a similar technique called dynamic field focusing (DFF), where the synchronized potential was increased only on the latter portion of an initial drift region. Modeling of this technique indicated that a resolving power of >2000 should be achievable in a linear time-of-flight mass spectrometer. Kinsel and Johnston [26] proposed the technique of post source pulse focusing as a simple variation of time-lag focusing where a voltage pulse could be applied to a short field-free region located after the ionization and acceleration regions. Properly timed, the pulse could be applied once the ions of interest had entered the region and thus provide discrete focusing. The technique was postulated to increase mass resolving power to >1000.

The Ion Mirror

Probably the singularly most effective innovation for improving mass resolving power comes from the development of the *reflectron* or *ion mirror* mass-independent energy focusing device first reported by Mamyrin in 1973 [27–29]. This device, illustrated in Figure 2-6, is simply a series of electrostatic diaphragms that provide a retarding electric

field with enough potential to "reflect" ions. Ions with different kinetic energies penetrate the mirror to different depths before being turned around. While all ions leave the mirror with exactly the same magnitude of energy they entered with, those ions possessing greater energy travel farther into the mirror and experience a time delay as a result of the increased flight path, compensating for their higher velocity in the field-free region. Instruments incorporating an ion mirror in the flight path produce a second space-focus plane having a higher resolving power than the first space-focus plane due to the additional energy focusing.

The simplest type of ion mirror is the single-field mirror that contains a homogeneous electric field. Ions penetrate the electric field and are eventually repelled back into the field-free drift region. The single-field ion mirror provides what is known as first-order focusing; a reference to the mathematical expressions used to describe focusing. The more commonly used two-field mirrors, are capable of second-order focusing, which yields a comparatively higher resolving power. Wollnik [30] described a grid-free, and thus non-linear-field mirror capable of yet higher-order focusing along with increased ion transmission.

The addition of the ion mirror in time-of-flight instrumentation has greatly improved the achievable resolving power and has been incorporated into a variety of instrument configurations. Mamyrin was initially able to achieve a resolving power of ~3000 using a 2-stage mirror. Schlag incorporated a 2-stage mirror into a multi-photon ionization time-of-flight instrument and achieved a resolving power of 3900 [31]. Della Negra used an ion mirror with a ^{252}Cf ionization time-of-flight instrument and achieved a resolving power of 2500 [32]. Schlag later achieved a resolving power of 10,000 in a multi-photon

ionization instrument [33]. Yang and Reilly achieved a resolving power of 11,000 using an ion mirror in a laser desorption time-of-flight instrument where the laser was directed from behind the sample [34]. Standing [35], who reported a resolving power of 3200 for a linear secondary ion mass spectrometry (SIMS) instrument, was able to further increase resolving power to 10,000 by incorporating a single-field ion mirror. Using a two-field mirror in a laser ionization time-of-flight instrument, Bergman and co-workers were able to obtain a resolving power of 35,000 [36].

The Effect of Ionization Method

The dramatic increases in resolving power obtained when incorporating the ion mirror are partly due to the fact that the ionization techniques employed minimize either the initial spatial or energetic distribution of the ions being examined. Ionization techniques such as SIMS [37], ^{252}Cf-plasma desorption [38], and matrix-assisted laser desorption ionization (MALDI) [39], ionize solid phase samples on a planar surface and thus minimize the initial spatial distribution of ions. The turn-around time is also eliminated because the surface matrix prevents ion motion against the accelerating field. Resolving powers of several thousand have been reported using these techniques in linear time-of-flight instruments, with resolving powers increased to 10,000 or more when combined with an ion mirror.

In another approach, molecules entering the ionization chamber are largely collimated into a molecular beam, reducing the range of thermal motion orthogonal to the beam axis to well below that expected from the typical Maxwell-Boltzman distribution. Ions are then formed in the beam using laser ionization and extracted along an axis perpendicular to the molecular beam. Thus, the initial spatial distribution is minimal due to the highly
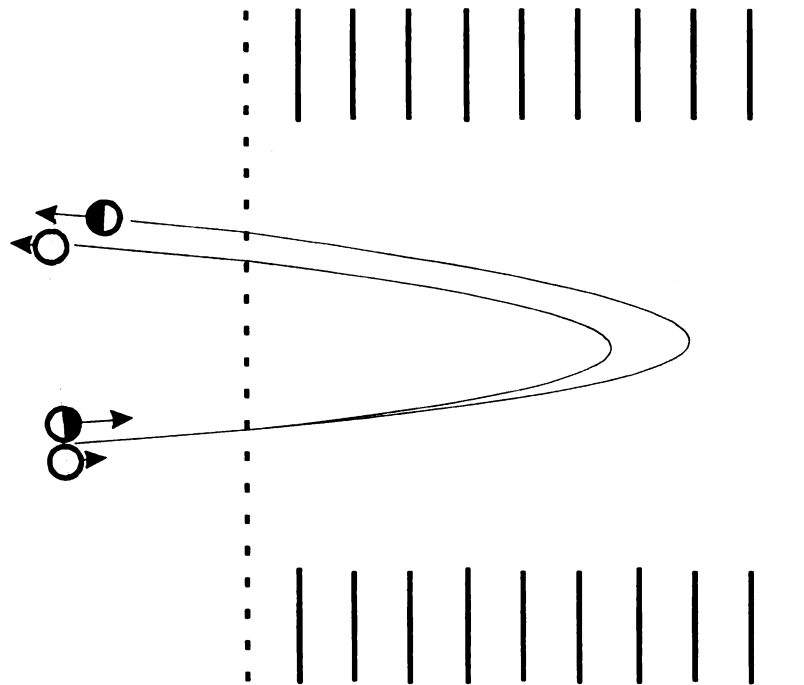
Figure 2-6. Single field ion mirror illustrating the flight path taken by two iso-mass ions having different total energies. The ion with the greatest energy penetrates the mirror the farthest before being reflected toward the detector, and thus experiences an increased flight path as well as a temporal delay.

focused laser beam and the significant reduction in the energy spread yields a higher resolving power. Using this technique, Reilly reported a resolving power of ~4700 [40].

Techniques such as those employed with gas and liquid sample introduction methods result in gas phase ionization where there is a distribution of both initial ion locations and kinetic energies, producing a need for both space and energy focusing if resolving powers similar to the planar ionization methods are to be approached. While the addition of ion mirror optics provides excellent increases in resolving power when the space or energy effect is encountered alone, the combined effects cannot be simultaneously compensated for using a single static ion optical device [41,42]. One possible solution would be the incorporation of multiple ion optical devices that would independently compensate for distinct components of the initial ion conditions. It is the intent of this dissertation to examine the feasibility of using another solution, a non-linear electric field within the ion source to accelerate the ions over the region of initial ion location, in order to provide improved space focusing and, consequently, an increase in resolving power. This development has the potential, when combined with other focusing techniques such as the ion mirror and impulse-field focusing, to provide complete correction for the initial ion behavior of gas phase samples.

Summary

This chapter outlines the basic theory of time-of-flight mass spectrometry and the major achievements that have resulted in improved mass resolving power in time-of-flight instrumentation. While these improvements have dramatically increased the resolving power in instrumental configurations that ionize samples from planar surfaces and other similarly confined ionization volumes, only relatively low resolving powers are

currently achievable when analyzing gas phase samples such as those produced in gas or liquid chromatographic analyses. An ion optical mechanism for overcoming one of the primary limitations to resolving power, the initial spatial distribution, is the focus of this dissertation.

Chapter References

1. Stephens, W. E. *Bull. Am. Phys. Soc.* **1946**, *21*, 22.

2. Cameron, A. E.; Eggers Jr., D. F. *Rev. Sci. Instrum.* **1948**, *19*, 605.

3. Keller, R. *Helv. Phys. Acta*, **1949**, *22*, 386.

4. Wolff, M. M.; Stephens, W. E. *Rev. Sci. Instrum.* **1953**, *24*, 616.

5. Katzenstein, H. S.; Friedland, S. S. *Rev. Sci. Instrum.* **1955**, *26*, 324.

6. Wiley, W. C.; McLaren, I. H. *Rev. Sci. Instrum.* **1955**, *26*, 1150.

7. Wiley, W. C. *Science*, **1956**, *124*, 817.

8. Mcfarlane, R. D.; Torgerson, D. F. *Int. J. Mass Spectrom. Ion Phys.* **1976**, *21*, 81.

9. Mamyrin, B. A.; Karataev, V. I.; Shmikk, D. V.; Zagulin, V. A. *Zh. Eksp. Teor. Fiz.* **1973**, *64*, 82.

10. Yefchak, G. E. *Doctoral Dissertation*, Michigan State University, 1990.

11. Cotter, R. J., *Anal. Chem.* **1992**, *64*, 1027A.

12. Sanzone, G. *Rev. Sci. Instrum.* **1970**, *41*, 741.

13. Marable, N. L.; Sanzone, G. *Int. J. Mass Spectrom. Ion Phys.* **1974**, *13*, 185.

14. Browder, J. A.; Miller, R. L.; Thomas, W. A.; Sanzone, G. *Int. J. Mass Spectrom. Ion Phys.* **1981**, *37*, 99.

15. Poschenrieder, W. P. *Int. J. Mass Spectrom. Ion Phys.* **1971**, *6*, 413.

16. Bakker, J. M. B. *Int. J. Mass Spectrom. Ion Phys.* **1971**, *6*, 291.

17. Poschenrieder, W. P. *Int. J. Mass Spectrom. Ion Phys.* **1972**, *9*, 357.

18. Kilius, L. R., Hallin, E. L., Chang, K. H., Litherland, A. E. *Nucl. Instrum., Meth.* **1981**, *191*, 27.

19. Steffens, P., Niehuis, E., Friese, T., Greifendorf, D., Benninghoven, A. *J. Vac. Sci. Technol. A* **1985**, *3*, 1322.

20. Sakurai, T.; Matsuo, T.; Matsuda, H. *Int. J. Mass Spectrom. Ion Phys.* **1985**, *63*, 273.

21. Sakurai, T.; Fujita, Y.; Matsuo, T.; Matsuda, H. *Int. J. Mass Spectrom. Ion Phys.* **1985**, *66*, 283.

22. Pinkston, J. D.; Rabb, M.; Watson, J. T.; Allison, J. *Rev. Sci. Instrum.* **1986**, *57*, 583.

23. Yefchak, G. E.; Schultz, G. A.; Allison, J.; Enke, C. G.; Holland, J. F. *J. Am. Soc. Mass Spectrom.* **1990**, *1*, 440.

24. Muga, M. L. *Anal. Instrum.* **1987**, *16*, 31.

25. Yefchak, G. E.; Enke, C. G.; Holland, J. F. *Int. J. Mass Spectrom. Ion Phys.* **1989**, *87*, 313.

26. Kinsel, G. R.; Johnston, M. V. *Int. J. Mass Spectrom. Ion Phys.* **1989**, *91*, 157.

27. Karataev, V. I.; Mamyrin, B. A.; Shmikk, D. V. *Sov. Phys. Tech. Phys.* **1972**, *16*, 1177.

28. Mamyrin, B. A.; Karataev, V. I.; Shmikk, D. V.; Zagulin, V. A. *Sov. Phys. JETP* **1973**, *37*, 45.

29. Mamyrin, B. A.; Shmikk, D. V. *Sov. Phys. JETP* **1979**, *49*, 762.

30. Grix, R.; Kutscher, R.; Li, G.; Grüner, U.; Wollnik, H. *Rapid Comm. Mass Spectrom.* **1988**, *2*, 83.

31. Boesl, U.; Neusser, H. J.; Weinkauf, R.; Schlag, E. W. *J. Phys. Chem.* **1982**, *86*, 4857.

32. Della-Negra, S.; LeBeyec, Y. *Int. J. Mass Spectrom. Ion Phys.* **1984**, *61*, 21.

33. Walter, K.; Boesl, U.; Schlag, E. W. *Int. J. Mass Spectrom. Ion Phys.* **1986**, *71*, 309.

34. Yang, M.; Reilly, J. P. *Int. J. Mass Spectrom. Ion Phys.* **1987**, *75*, 209.

35. Tang, X.; Beavis, R.; Ens, W.; Lafortune, F.; Schueler, B.; Standing, K. G. *Int. J. Mass Spectrom. Ion Phys.* **1988**, *85*, 43.

36. Bergmann, T.; Martin, T. P.; Schaber, H. *Rev. Sci. Instrum.* **1989**, *60*, 792.

37. Chait, B. T.; Standing, K. G. *Int. J. Mass Spectrom. Ion Phys.* **1981**, *40*, 185.

38. Macfarlane, R. D.; Torgerson, D. F. *Int. J. Mass Spectrom. Ion Phys.* **1976**, *21*, 81.

39. Hillencamp, F., Karas, M., Beavis, R. C., and Chait, B. T. *Anal. Chem.* **1991**, *63*, 1193A.

40. Opsal, R. B.; Owens, K. G.; Reilly, J. P. *Anal. Chem.* **1985**, *57*, 1884.

41. Stein, R. *Int. J. Mass Spectrom. Ion Phys.* **1974**, *14*, 205.

42. Stein, R. *Int. J. Mass Spectrom. Ion Phys.* **1994**, *132*, 29.

CHAPTER 3

THE MICHIGAN STATE UNIVERSITY M-TOF

Introduction

While the integrating transient recorder project described in Chapter 1 was being completed, attention was focused on developing a time-of-flight mass spectrometer that would complement the capacity for high-speed data acquisition. Previous attempts at developing time-of-flight instrumentation, while successfully illustrating novel concepts, had failed to provide both mass independent focusing and the detectability required for cutting-edge chromatographic analyses. An acquired linear CVC 2000 [1] time-of-flight instrument utilizing a two-field Wiley/McLaren ion source geometry and time-lag focusing was capable of generating only scanned mass spectral information and exhibited relatively poor detectability [2]. A beam-deflection time-of-flight instrument successfully demonstrated the performance of the ITR, but with only marginal detectability [3]. A proposed DFF modification to the CVC 2000 could possibly have provided sufficient mass resolving power along with a concomitant increase in detectability, but the project was dropped due to the high costs projected for completion of the electronics circuitry.

During this period, one of the Mass Spectrometry Facility directors delivered a lecture at an American Society for Mass Spectrometry meeting [4] in which the research progress to date was described as well as the fundamental requirements for adequate time-of-flight instrumentation compatible with the ITR. This lecture led to a meeting with Professor Hermann Wollnik, who described a time-of-flight mass spectrometer [5] developed in his laboratory in Giessen, Germany, in which a novel electron ionization source was

combined with an ion mirror for improved detectability and mass-independent ion focusing. It was reported that resolving powers near 20,000 had been achieved with this instrument at a base pressure of 1×10^{-10} torr. Subsequently, a collaboration was established whereby a time-of-flight mass spectrometer would be sent to the MSU Mass Spectrometry Facility for adaptation as a chromatographic detector and an ITR would be sent to the laboratory in Germany. The collaboration was initiated by an exchange of post-doctoral associates, with Dr. Ron Tecklenburg first traveling to the Wollnik laboratory to learn the performance and operation of the time-of-flight mass spectrometer, and Dr. Raimund Grix arriving at MSU soon after the mass spectrometer was delivered. A second collaboration with Meridian Instruments, Inc., enabled Dr. Grix to remain working in the MSU Mass Spectrometry Facility for several years.

Duty Cycle Requirements

The time-of-flight mass spectrometer developed by the Wollnik research group incorporated two unique features. First, the ion mirror providing mass independent focusing was of a gridless non-linear field design and was reported to possess high-order focusing properties [6]. Second, and eventually more important to the success of GC-TOFMS, was a reported capacity for ion storage between source ion extraction events.

The significance of these two features lies in the potential effect they have on duty cycle. There are two types of duty cycle relevant to mass spectrometry. One of these, the *scanning duty cycle,* is an assessment of the efficiency of measurement along the mass (m/z or u) axis. For scanning mass spectrometers, this is the ratio of the mass range being detected at any instant to the total mass range of the analysis. For example, if the resolution of measurement is 0.2 u and the range being scanned is 500 u, the scanning

duty cycle is 0.04% and at any given instant only 1/2500 of the information along the mass axis is being measured. Previous TOF instruments, with their mass-dependent focusing, employed time-slice detection (described in Chapter 1) and were thus essentially scanning instruments. With the availability of the ITR, m/z information could be acquired over the entire mass range of interest for each transient, significantly increasing the duty cycle. This potential could only be realized however, if ions over the entire mass range were simultaneously in temporal focus, and the ion mirror provided this feature.

The second duty cycle, the *sampling duty cycle*, is a measurement of the efficiency of sample utilization. This is an important consideration for TOF instruments since they employ a cycle of ion generation, instantaneous ion extraction and subsequent m/z analysis. Previous commercial TOF instruments used pulsed ionization, typically 1 μsec, followed by a 99 μsec analysis, yielding a duty cycle of only 1%. This is adequate for a steady state sample, but for dynamic samples, such as a chromatographic eluent, severe undersampling can occur. Even for an instrument using continuous ionization, most of the ions formed during the 99-μsec extraction and analysis time are lost to the vacuum system and neutralization processes. The ion source technology developed by Dr. Grix in the Wollnik laboratory was reported to have ion storage times of up to several msec with storage efficiencies of up to 20% [5]. Additionally, the process providing the ion storage also caused "ion bunching" that lowered both the initial ion energy and spatial distributions in the source and enhanced the mass resolving power; also contributing to improved detectability.

That both of these features were simultaneously required is apparent when it is considered that the overall duty cycle of a TOF instrument is the product of both the scanning and sampling duty cycles. In the example above, $1/2500 \times 1/100 = 0.0004\%$, which is significantly lower than the duty cycle available with other forms of mass spectrometry. For a TOF instrument to be suitable in GC-MS, a significantly higher duty cycle was required.

The M-TOF

The time-of-flight mass spectrometer initially delivered to MSU was quickly replaced by an improved design more amenable to chromatographic sample introduction. This instrument, referred to as the M-TOF (where the M stands for "mirror"), illustrated in Figure 3-1, was the result of a collaborative effort involving a number of professors, post-doctoral associates and graduate students. This authors' responsibilities included the mechanical design and engineering. The M-TOF consisted of a vacuum system having two essentially separate chambers to facilitate differential pumping between the relatively higher pressure ion source region and the lower pressure analyzer and thus preserve the mass resolving power. Both chambers were vacuum pumped using 180 L/sec turbomolecular pumps, each backed by an isolated roughing pump. The gridless ion mirror was attached to the lower flange of the analyzer chamber, while the custom built channel-plate detector assembly was attached to the upper analyzer chamber flange. Half of the ion source was mounted to the upper flange of the source chamber, along with the electrical feedthrough, while the remainder of the ion source was mounted to the inside of the ion source chamber. An Einzel lens and deflection plate assembly were located in the connecting tube between the two chambers. A viewport on the front of the ion source

chamber facilitated positioning of the chromatographic column end, which entered the vacuum chamber through a separate feedthrough/flange assembly. The instrument had a 1.65-m overall ion flight path length. The system was operated with the analyzer drift region at ground potential, and the ion source configured to provide approximately 1000 V total ion energy. Typical ion optical element voltages are listed in Table 3-1.

Electrode	Potential (Volts)
G3	820
G3 when pulsed	950
G2	820
Filament	755
Pushers	760
G1	255
G0	0
Einzel Lens	-600
Mirror Back	1000

Table 3-1. Typical voltages used in operating the M-TOF.

Ion Storage and the Grix Source

A cross-sectional view of the cylindrically symmetric ion source developed in the Wollnik laboratory is shown in Figure 3-2. Electrons generated by an annular filament are directed into the center of the source between two gridded electrodes (G2 and G3) by two ring electrodes called "pushers". During ion storage, the potential applied to G2 and G4 are similar and slightly positive with respect to G3. This provides a potential well in the vicinity of G3 where ions could be retained between ion extractions, and the

Interface

Ion Source

Gaseous Sample

Turbo Pump

Einzel Lens

Steering Plates

Detector

Signal to ITR

Ion Flight Path

Turbo Pump

Ion Mirror
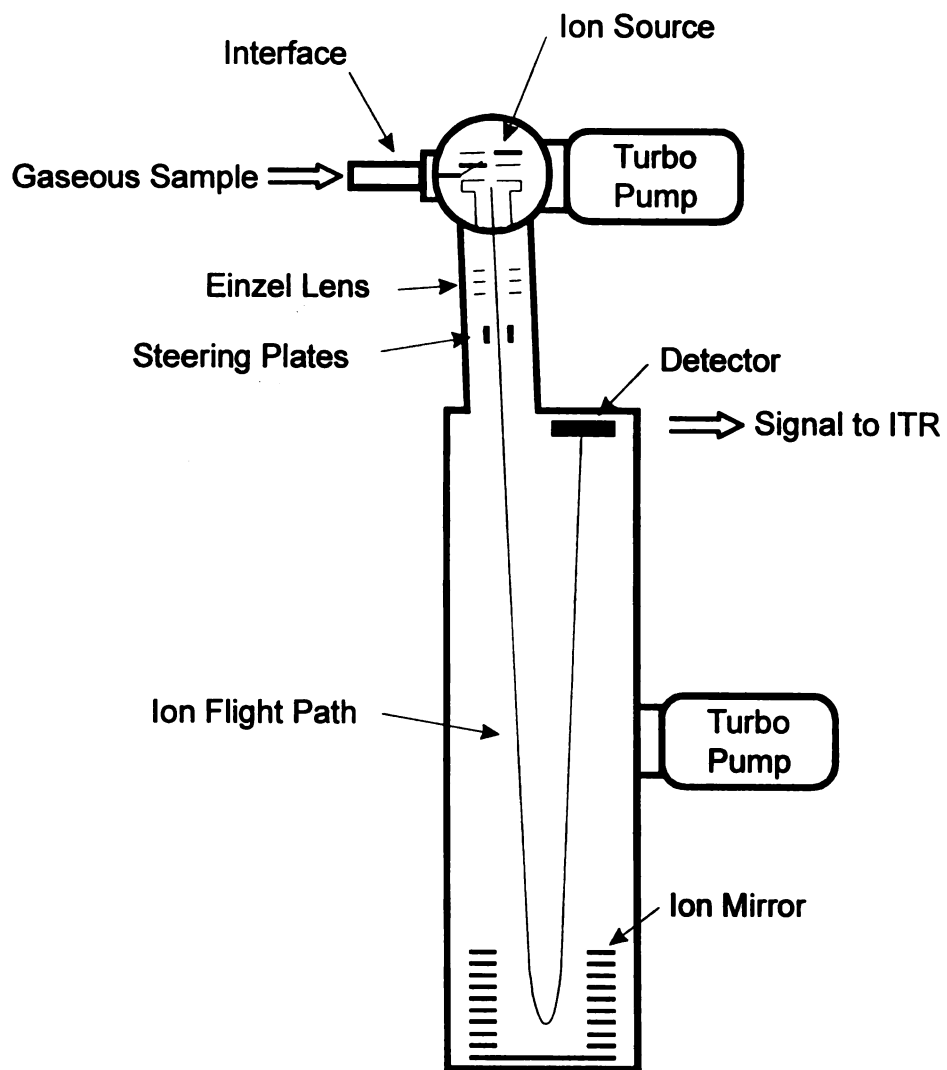
Figure 3-1. M-TOF mass spectrometer.

potential depth of the well could be varied to optimize this trapping capability. An extraction pulse applied to G3 repels the stored ions through G2 and G1 into the analyzer for m/z analysis.

Early in the development of the ion source at MSU by Dr. Grix, questions arose challenging the hypothesis that G3 was the location of ion storage. This was partially due to the fact that, in principle, the limited transmission of the grid material should have removed a large fraction of the generated ions as they pass through the grid multiple times during storage. Additionally, it was observed that ion detectability remained high even when the potential applied to G3 during ion storage was higher than that of G2 and G4. It should thus be impossible for the ion storage to occur at G3 under these conditions. Subsequent experiments with and without the G3 electrode in the ion source yielded similar detectabilities and storage characteristics, verifying that G3 was not the essential storage element and that the ion source did not function as originally described by the inventors [7].

A more likely explanation for ion storage was that a potential well was being formed by the continuously generated electron beam. It was observed that ion storage and detectability were significantly more dependent on the potentials applied to the pusher electrodes and the alignment of the pusher/filament assembly. Early evidence for electron beam ion storage mechanism was first provided by Studier [8] in 1963, in a paper describing a time-of-flight ion source wherein, using continuous ionization, a 300-fold increase in detectability was achieved over that attained using pulsed ionization. Further support came from Baker and Hasted [9], and consequently, the Studier configuration was used as the model for further ion source developments in the facility.

a)

b)
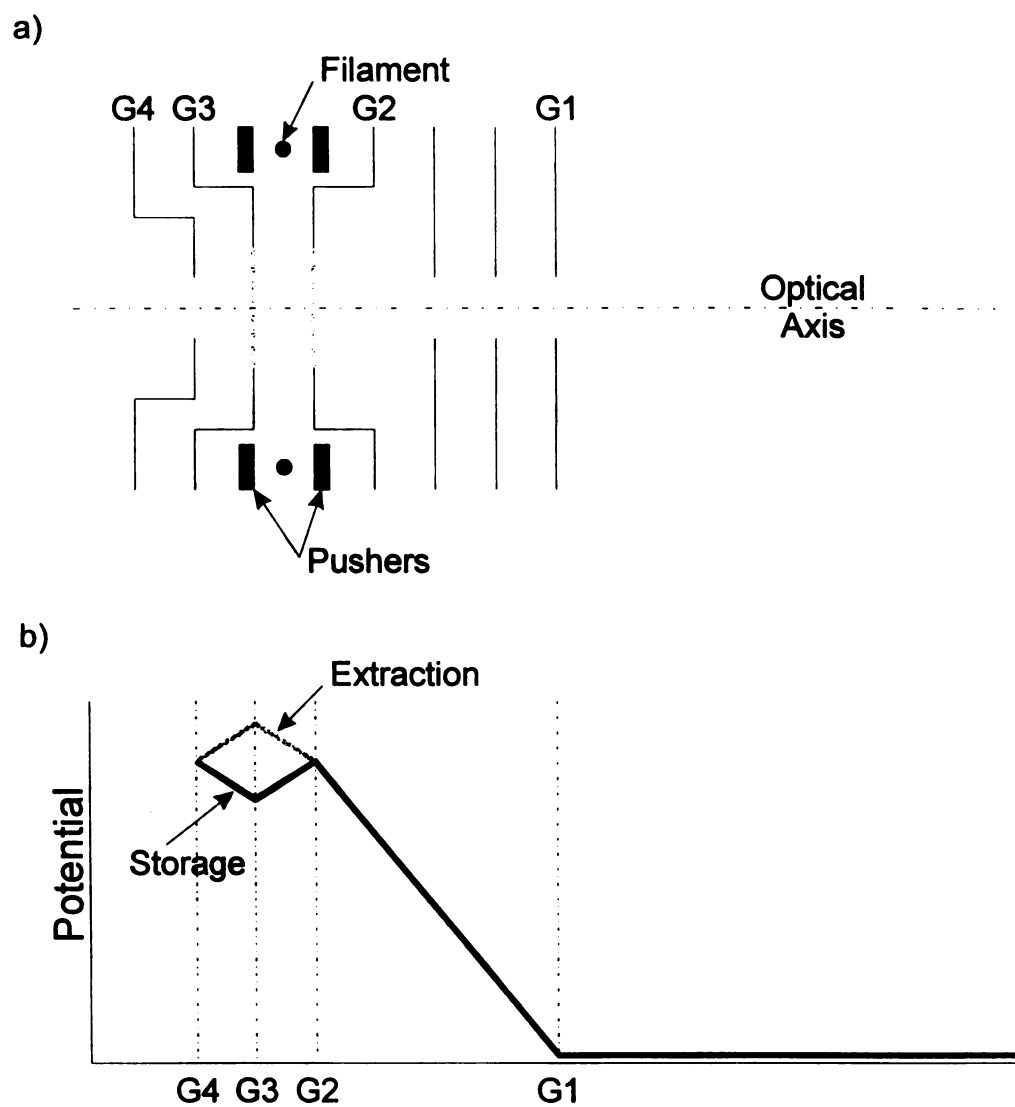
Figure 3-2. Cross sectional view (a), and potential diagram (b), illustrating the operation of the original Grix/Wollnik ion source.

The second source developed by Dr. Grix utilized an advanced design, that eliminated the previous G3 electrode and retained the annular filament and electron beam pushers. In this design however, the repelling electrode (now G3), the filament and the pushers were mounted on a removable flange and the G2, G1 and G0 electrodes were mounted in the ion source chamber. This ion source is depicted in Figure 3-3, and illustrates the heated conduit through which GC capillary column was inserted. Optimal chromatographic detectability was obtained when the column end was flush with the G2 electrode surface.

The M-TOF performance [10] with this Grix ion source was, at times, phenomenal. Mass resolving powers of 1500 were achievable, as illustrated in Figure 3-4, and an ultimate detectability of 5 fmol bromobenzene (780 pg) was attained, as illustrated in Figure 3-5. However, it eventually became clear that when operational, rather remarkable results could be attained, and when not, as was often the case, the ion source required extensive attention. This attention could apparently only be provided by Dr. Grix, and even under his expert care, it often took many hours of mechanical adjustment and electrical tuning of both the ion source and mirror to effect a functional recovery.

Subsequent Ion Sources

When the limitations to the Grix/Wollnik ion source configurations were fully recognized, a series of experiments aimed at achieving a more reproducible and stable ion source configuration was begun. These experiments were conducted primarily by this author and Dr. George Yefchak who, after graduation from MSU, was employed by Meridian Instruments to guide aspects of the research that would eventually lead to a commercial product. Dr. Yefchak had previously developed a theoretical model describing the ion storage process [7], and conducted initial experiments suggesting
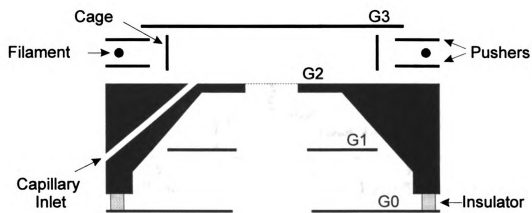
Figure 3-3.   The Grix M-TOF ion source.

Low Mass

High Mass

(a)

(b)
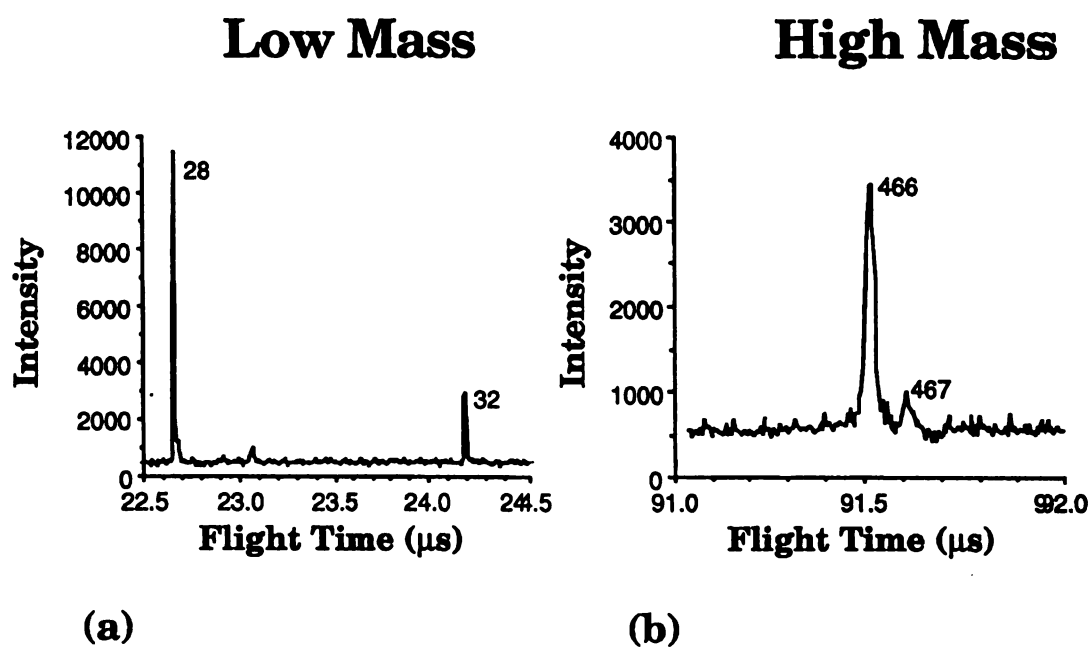
Figure 3-4. Demonstration of M-TOF resolving power for a) residual gas ions where, with a 12 nsec FWHM, R=920 and b) tris(heptafluoropropyl)-8-triazine where, with a 30 nsec FWHM, R=1500.
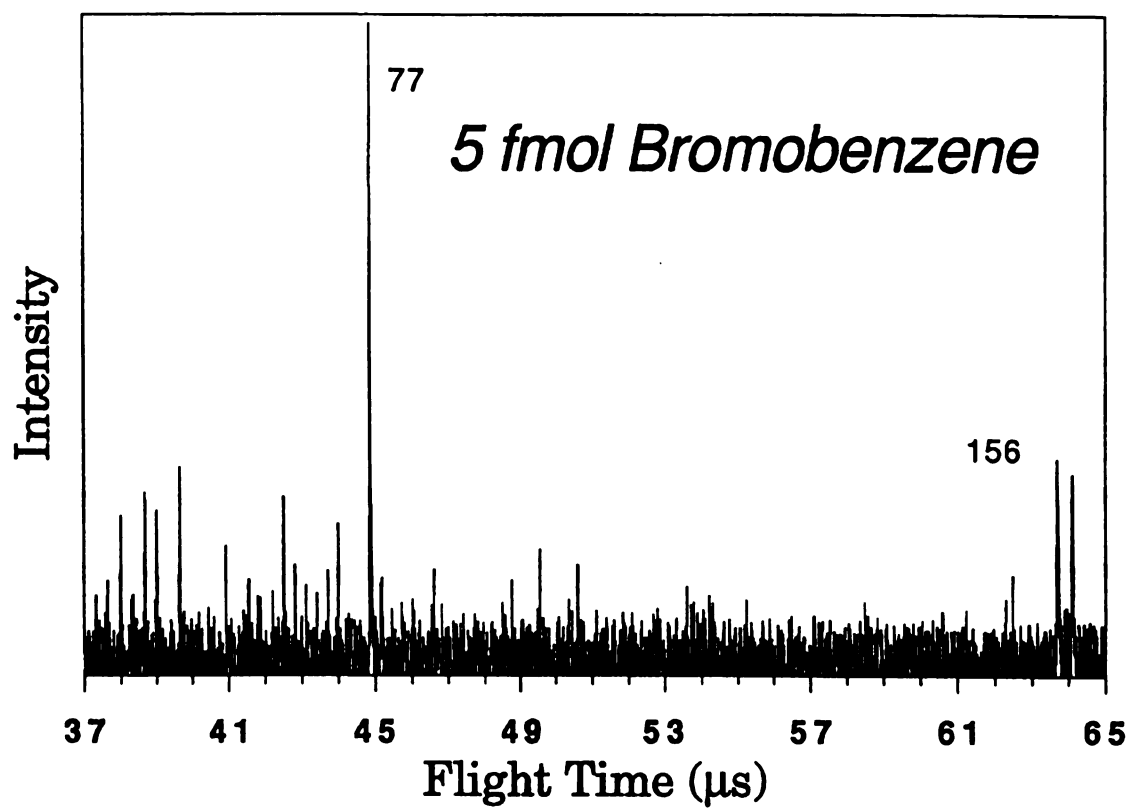
Figure 3-5. M-TOF detectability using the Grix ion source.

that the storage process may be mass-dependent, as well as pressure dependent [11,12]. These results led to a comparison of ion storage capabilities for the various ion source configurations and formed the basis for benchmark performance evaluations.

The theoretical model postulates that the number of ions, n, in the storage region follow the rate equation

$$\frac{dn}{dt} = k_F - k_L n \qquad (3\text{-}1)$$

where t is time, and k_F and k_L are the formation and loss rate constants, respectively. Integration of Equation 3-1 yields

$$n(t) = \frac{k_F}{k_L}\left(1 - e^{-k_L t}\right) \qquad (3\text{-}2)$$

It is important to distinguish between ion storage, as used in describing time-of-flight ion source behavior, and ion trapping. With ion trapping, a given ion may have an extended residence time within the trap volume, such as is observed in ion trap mass spectrometers. With ion storage, no evidence of extended ion residence times is observed, either through evidence of ion-molecule reactions or otherwise. The concept merely describes a steady-state, or "leaky bucket" ion population model in which enhanced storage levels are achieved when ion loss rates are minimized. A theoretical plot describing this model is shown in Figure 3-6. An increase in the observed ion population occurs as the storage time between ion source extractions is increased, until a steady-state ion population is achieved.
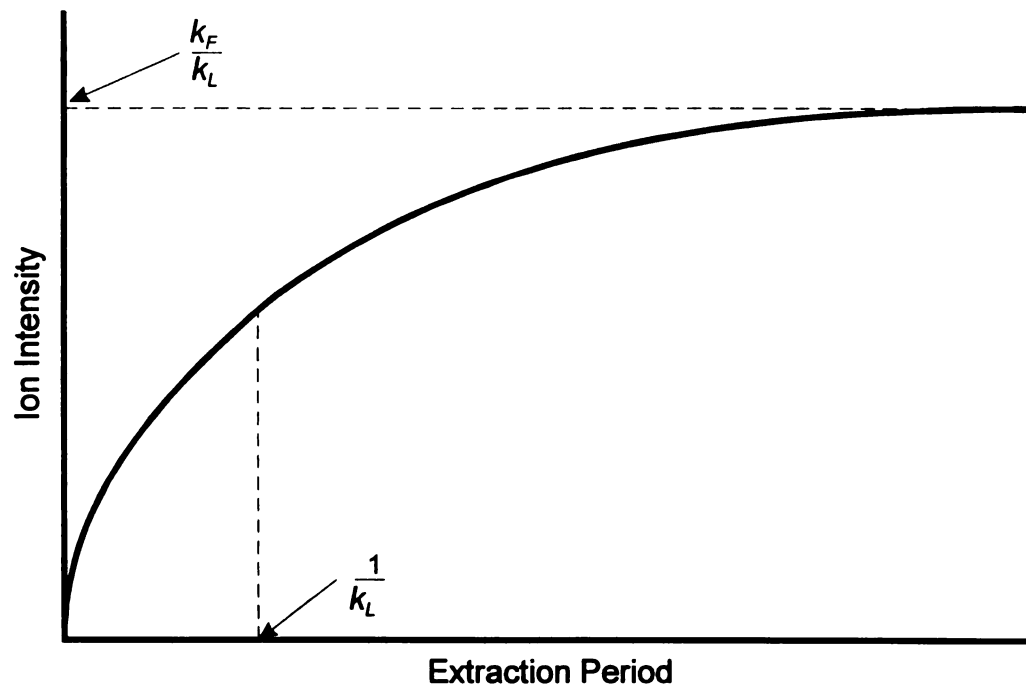
Figure 3-6. Trend for ion population growth curves.

The experimentation with non-Grix style ion sources began by evaluating a rather small unmodified Finnigan quadrupole ion source that, while exhibiting a low resolving power of ~50, showed a capacity for ion storage. This author then constructed a series of larger ion sources through which to explore the actual mechanism of ion storage and to develop a more rugged and reliable mechanical design. A summary of results obtained with these sources is given in Table 3-2. A variety of ion source physical parameters were tested, including several having multiple linear filaments and several incorporating an isolating "cage" that provided a field-free region around the ion optical volume. Of the various configurations explored, those having a more extensive cage and those having more filament surface (i.e. more electron flux) showed the best storage characteristics, and exhibited the best resolving power and detectability. The best achieved detectability was 1.6 pg bromobenzene, observed using a time-synchronized oscilloscope for detection readout.

While the use of linear filaments and the field isolating electrodes provided a more robust ion source configuration, the reliability of these ion sources remained marginal and exhibited day to day fluctuations in performance. Shortly after these experiments were completed however, in a collaboration with Meridian Instruments, Inc., it was ascertained that the inclusion of rare-earth magnets and additional electron beam steering electrodes had a significant positive impact on performance consistency. This knowledge became instrumental in developing the ion sources presently used.
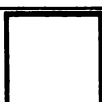
Geometry	$1/k_L$	k_F	R
a)	0.19	11,900	1300
b)	0.32	1,700	1200
c)	0.17	650	900
d)	0.08	2,400	900
e)	0.07	1,000	600
f)	--	--	600

Table 3-2.   Comparison of various ion source configurations. For each cross sectional view, the gray lines represent filaments, while the dark lines represent field cages and electron beam focusing electrodes.

Further Developments

As work progressed in developing the ion source technology required for GC-TOFMS, funding priorities shifted at the National Institutes of Health, which was the primary federal funding agency sponsoring this research. Consequently, funds for this research significantly diminished. However, Meridian Instruments, Inc. had acquired the licenses for the ITR from MSU and, being interested in developing a commercial GC-TOFMS product, continued to financially support much of the research. This research led to the production of a viable GC-TOFMS system, the commercial rights to which were sold to LECO Corporation in 1995. A research project by this author, utilizing the LECO FCD-650 time-of-flight mass spectrometer, is included as Appendix A.

Summary

The research conducted at the MSU Mass Spectrometry Facility has yielded a significant advance to the state of the art in mass spectrometric detection for cutting-edge gas chromatographic analyses. A gas chromatographic analysis record of 55 compounds in 14 seconds has been achieved, and a number of terms are now an accepted and common part of the scientific nomenclature.

While there was no consensus regarding the mechanism of ion storage, and while the equipment developed in the laboratory exhibited a low working efficiency, further engineering led to the development of a powerful commercial product. As such, the entire project represents a major success for all who were involved: MSU, the members of the Mass Spectrometry Facility, the National Institutes of Health who sponsored the research, and for the American model of moving good ideas from the academic setting to the broader public arena. It was also this work in ion source development that prepared this author for developments described in the next chapter.

Chapter References

1. CVC Products, Inc., Rochester, New York.

2. Erickson, E. D.; Enke, C. G.; Holland, J. F.; Watson, J. T. *Anal. Chem.* **1990,** *62,* 1079.

3. Schultz, G. A.; Chamberlin, B. A.; Sweeley, C. C.; Watson, J. T.; Allison, J. *J. Chrom.*, **1992,** *590,* 329.

4. Enke, C. G. In *Proceedings of the 36ᵗʰ ASMS Conference on Mass Spectrometry and Allied Topics,* San Francisco, CA, June 5–10, **1988,** 363.

5. Grix, R.; Grüner, U.; Li, G.; Stroh, H.; Wollnik, H. *Int. J. Mass Spectrom. Ion Proc.* **1989,** *93,* 323.

6. Grix, R.; Kutscher, R.; Li, G.; Grüner, U.; Wollnik, H. *Rapid Comm. Mass Spectrom.* **1988,** *2,* 83.

7. Yefchak, G. E. *Doctoral Dissertation,* Michigan State University, 1990.

8. Studier, M. H. *Rev. Sci. Instrum.,* **1963,** *34,* 1367.

9. Baker, F. A.; Hasted, J. B. *Phil. Trans. Roy. Soc. London,* **1966,** *261,* 33.

10. Grix, R.; Tecklenburg, Jr., R. E.; Watson, J. T.; Holland, J. F.; Yefchak, G. E.; Gardner, B. D.; Allison, J.; Enke, C. G.; Wollnik, H. In *Proceedings of the 39ᵗʰ ASMS Conference on Mass Spectrometry and Allied Topics,* Nashville, Tennesee, May 21–26, **1991,** 154.

11. Yefchak, G. E.; Puzycki, M. A.; Allison, J.; Enke, C. G.; Grix, R.; Holland, J. F.; Li, G.; Wang, Y.; Wollnik, H. In *Proceedings of the 38ᵗʰ ASMS Conference on Mass Spectrometry and Allied Topics,* Tucson, AZ, June 3–8, **1990,** 540.

12. Seeterlin, M. A. *Doctoral Dissertation,* Michigan State University, 1993.

CHAPTER 4

NON-LINEAR ION ACCELERATION

Introduction

As energy correcting devices such as the ion mirror continue to develop and improve in their focusing properties, the major detriment to resolution arises from energetic variations due to spatial displacement and temporal variations due to ion turn-around. While ion turn-around can be virtually eliminated with the newer surface ionization techniques, it remains a major variable in methods employing three-dimensional ionization volumes. In these applications, the effect of ion turn-around can be reduced by higher source extraction fields. This is a common practice which, unfortunately, exacerbates the spatial displacement problem. Additionally, many recent applications encourage the increase of either the ion source dimension itself or the source dimension/total flight distance ratio, a situation which also emphasizes the need for better spatial corrections. Consequently, the major objective of this study is to evaluate prior efforts to correct for temporal variations due to displacement along the optical axis at the moment of ion formation, to postulate a non-linear field model to accomplish this end, and to confirm the efficacy of the model with experimental results.

The Wiley/McLaren 1ˢᵗ Order Space Focus Model

Wiley and McLaren's innovations using the two-field ion source brought recognition of a location along the flight path where the temporal spread of an iso-mass ion packet is minimal, which in terms of space focusing is the optimal location for ion detection. This

location since known as the *space focus plane*, and the strengths and limitations of the Wiley and MeLaren innovations along with the model on which they are based can be evaluated by examining the processes that determine when the ions arrive at the detector.

Ion motion through an electric field

Figure 4-1 illustrates the two-linear-field ion source model implemented by Wiley and McLaren[1]. An ion with initial energy U_0, beginning at a position s, axially located within the ion source, will increase its energy as it is accelerated through the electric fields until it achieves a final energy U, upon leaving the ion source. The time required for an ion to reach the detector can be determined using the analytical equations for motion and force.

The kinematic equation for motion in space along a straight line with constant acceleration has the basic form

$$x = x_0 + v_0 t + \frac{1}{2} a t^2 \tag{4-1}$$

where x is position, x_0 is the initial position, v_0 is the initial velocity, a is acceleration and t is time. Since the distance $d = x-x_0$, Equation 4-1 can be rearranged to

$$\frac{1}{2} a t^2 + v_0 t - d = 0 \tag{4-2}$$

and solved for t using the quadratic equation solution to yield

$$t = \frac{-v_0 \pm \sqrt{v_0^2 + 2ad}}{a} \tag{4-3}$$

where only the + second term will be applied since the second term is always larger
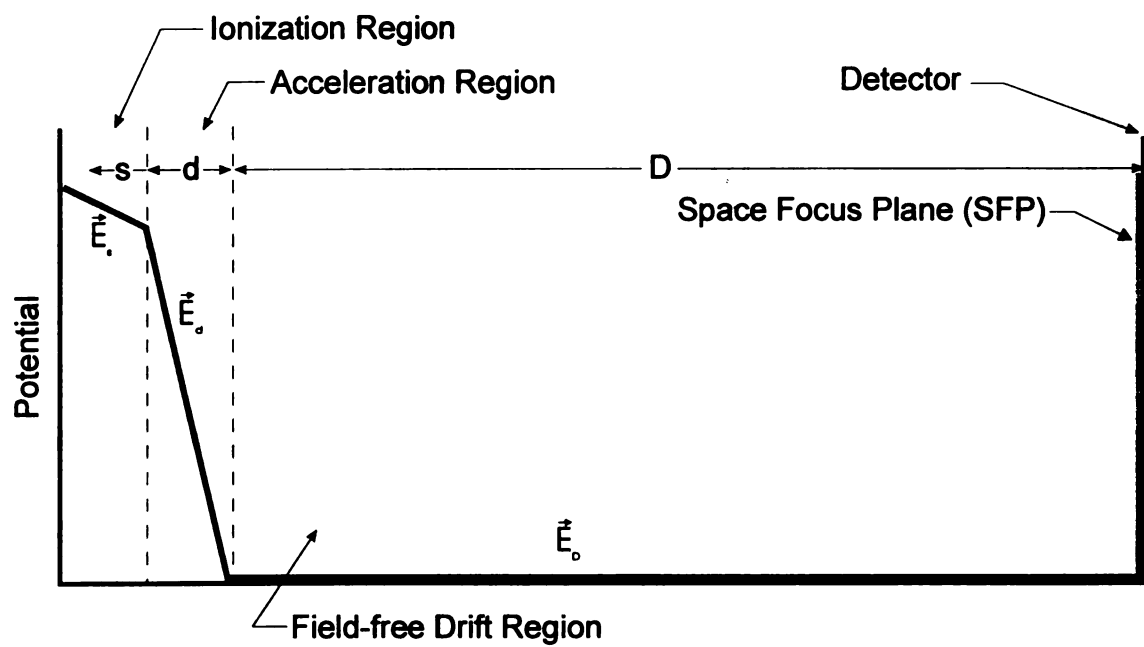
Figure 4-1. Two-field acceleration geometry implemented by Wiley and McLaren.

than the first and time is always positive. Equation 4-3 can be applied to time-of-flight analysis by substituting for v and a using the following fundamental relationships. Given that

$$U = \frac{1}{2}mv^2 \tag{4-4}$$

where U is the ion total kinetic energy, m is mass and v is velocity, the equation can be solved for velocity, v, giving

$$v = \sqrt{\frac{2U}{m}} \tag{4-5}$$

Likewise, the analytical equation for force,

$$F = ma = qE \tag{4-6}$$

can be solved for acceleration, a, to form

$$a = \frac{qE}{m} \tag{4-7}$$

(The term q is used here rather than ze to preserve the Wiley/McLaren nomenclature, which includes dimensional units of cm, μsec, eV, and mass units u). Substituting the equations for a and v into Equation 4-3, yields an expression for t that is a function of U_0 and initial ion position

$$t(U_0,d) = 1.02\left(\frac{\sqrt{2m}}{qE}\right)\left(\sqrt{U_0 + qdE} - \sqrt{U_0}\right) \tag{4-8}$$

which forms the basis of the equations Wiley and McLaren used to compute the flight time for ions accelerated using the two-field ion source.

The flight time through the first accelerating field in the two-field ion source is thus

$$t_s = 1.02 \left(\frac{\sqrt{2m}}{qE_s} \right) \left(\sqrt{U_0 + qsE_s} - \sqrt{U_0} \right) \qquad (4\text{-}9)$$

and is proportional to the square root of the energy applied to an ion plus or minus the square root of the energy already possessed by the ion depending on whether the initial energy is with or against, respectively, the applied energy.

As the ion travels through the second electric field it acquires additional energy. The time of flight through the second electric field is determined in similar fashion to that of the first electric field, and is thus

$$t_d = 1.02 \left(\frac{\sqrt{2m}}{qE_d} \right) \left(\sqrt{U_0 + qsE_s + qdE_d} - \sqrt{U_0 + qsE_s} \right) \qquad (4\text{-}10)$$

which, as was shown with Equation 4-9, is proportional to the square root of the energy applied to the ion minus the energy already possessed by the ion.

The time t_D required to transit the field-free region D from the ion source exit to the detector is a function of the total ion energy, and is thus

$$t_D = 1.02 \frac{D\sqrt{2m}}{2\sqrt{U_0 + qsE_s + qdE_d}} = 1.02 \frac{D\sqrt{2m}}{2\sqrt{U}} \qquad (4\text{-}11)$$

Finally, the total time required for an ion beginning at position s to reach the detector is the sum of each of these times

$$t = t_s + t_d + t_D \qquad (4\text{-}12)$$

Space Focusing

Space focusing depends on the fact that an ion located closer to the exit in the ion source acquires less energy, and consequently a lower velocity, than an ion located farther back in the ion source. The less energetic ion exits the source first but is subsequently overtaken by the more energetic ion at the space focus plane. While the ion arrival time at the space focus position is a function of total ion energy and m/z, ideal space focusing requires that the arrival time be totally independent of initial ion position s.

Mathematically Described

In evaluating an ion possessing no internal energy ($U_0=0$) and beginning at position s from an ion population centered about s_0, there should ideally be no change in arrival time at the space focus plane with respect to s.

$$\left(\frac{dt}{ds}\right)_{0,s_0} = 0 \qquad (4\text{-}13)$$

Unfortunately, when using linear, homogeneous electric fields to obtain Equation 4-12 as derived above, the result of Equation 4-13 is not zero.

Evidence for this can be easily obtained using the equations derived above to evaluate two ions beginning from two different axial locations, s_1 and s_2, in a single-field ion source. Since the time required for both ions to arrive at the space focus plane should be equal according to the Wiley/McLaren model, the equations for the total flight time of both ions (Eq. 4-12) can be set equal to each other. The combined equation can then be solved for D.

$$D = 2\sqrt{s_1 s_2} \qquad (4\text{-}14)$$

Likewise, since the two ions being evaluated must travel the same distance D, the same equations can also be rearranged to solve for D and set equal to each other. By subsequently solving for t, one obtains

$$t = \sqrt{\frac{2m}{qE}} \frac{s_1 - s_2}{\sqrt{s_1} - \sqrt{s_2}}$$

(4-15)

In Equations 4-14 and 4-15 it is seen that both D and t depend on the values of s_1 and s_2, which would not be the case if, under the conditions of constant linear acceleration, $dt/ds=0$ at the space focus position.

Wiley and McLaren evaluated deviations from ideal space focusing in the following manner. Assuming that $U_0=0$ and $s=s_0$, the following substitutions

$$U = qs_0 E_s + qdE_d$$

(4-16)

$$k_0 = \frac{s_0 E_s + dE_d}{s_0 E_s}$$

(4-17)

can be implemented into Equation 4-12, yielding

$$t(U_0, s_0) = 1.02 \sqrt{\frac{m}{2U}} \left(2s_0 \sqrt{k_0} + \frac{2\sqrt{k_0}}{1 + \sqrt{k_0}} d + D \right)$$

(4-18)

The location of the space focus position for ions beginning at $s=s_0 \pm \frac{1}{2}\delta s$ can be determined by setting the derivative of t with respect to s equal to 0, to obtain

$$D = 2s_0 k_0 \sqrt{k_0} \left(1 - \frac{1}{k_0 + \sqrt{k_0}} \frac{d}{s_0} \right)$$

(4-19)

Deviations from ideal space focusing can then be determined using a series expansion of $t(0,s)$ about s_0.

Graphically Illustrated

Graphically, ion behavior using linear field acceleration is illustrated in Figure 4-2. Here, five ions having equal m/z and no internal energy are accelerated through the ion source with the total energy acquired by each ion being a function of the initial location. It can be seen that ions 1 and 2, originating from positions closest to the ion source exit, arrive at an axially co-planar location earlier than the remaining ions, and at a location in front of the defined space focus plane. Likewise, those ions originating from positions farthest from the ion source exit (ions 4 and 5) achieve a co-planar relationship beyond the defined space focus plane and at a later time. Only those ions originating from positions near the center of the ionization region arrive at the prescribed space focus plane co-temporally. Never are all of the ions either co-temporal at a given plane or co-planar at a given time. However, as postulated by Wiley and McLaren, under conditions where the spatial displacement is minimal, a reasonable first order approximation of space focusing can be achieved.

This single field model was used by Wiley and McLaren to evaluate and describe space focusing, and provided the theoretical basis for the two-field source used in their mass spectrometer design. The addition of the second, shallow-gradient electric field in the ionization region allowed them to place the space focus plane at the detector surface, even with the detector located several meters from the source. The gain was a significant increase in resolving power, although the temporal characteristics of the space focus plane were diminished from that of the single-field source.
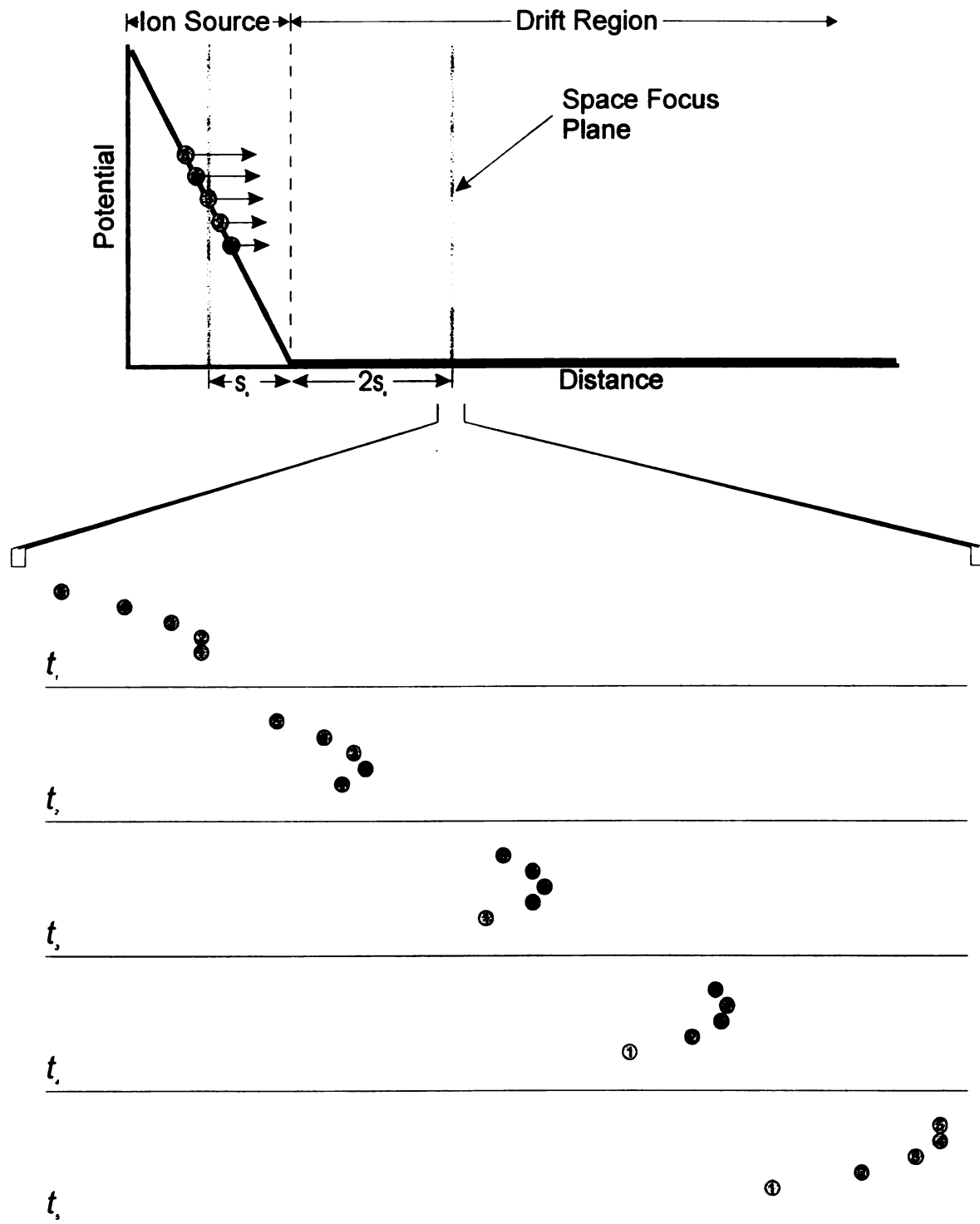
Figure 4-2. Illustration of ion behavior at the space focus plane using single linear-field acceleration.

The fact that the single-field model provides better space focusing than the two-field model if further validation of the conclusion that linear fields can provide only a first-order approximation of perfect space focusing. This is intuitively understandable since linear physical displacements produce linear energy variations which result in second order velocity changes that linearly affect the resulting time measurements. Thus, with linear fields the space focus plane is in reality not a well defined plane. The region of minimum temporal spread is displaced along the ion optical axis in relation to the position of origin in the ion source, and the overall width of the temporal minimum dimension increases with the range of the physical displacement along that axis in the ion source. Clearly, to achieve the higher levels of resolution desired for many modern applications of TOFMS, an alternate acceleration scheme must be employed.

Ideal Space Focusing

Given that linear accelerating fields do not provide complete space focusing, and that there is a non-linear relationship between energy and ion velocity, it is reasonable to propose that some form of non-linear acceleration may provide improved space focusing. Indeed, there have been several attempts at incorporating non-linear acceleration into TOF mass spectrometer design, and these can be classified as either *dynamic* or *static* in nature.

Dynamic Non-linear Fields

In the dynamic non-linear field model, the field imposed on the ions is static over space at any given moment and may be homogeneous. However, as the field is temporally changing, the force applied to the ions is effectively non-linear in time. The first reported use of a dynamic field occurred with the IFF technique, described in

Chapter 2. With IFF, a two-step-in-time electric field was generated in the ion source, with the first relatively high amplitude pulse rapidly accelerating the ions prior to application of the extraction field. The velocity compaction technique proposed by Muga [2], the dynamic field focusing technique proposed by Yefchak [3], and post-source pulse focusing [4] also represent the incorporation of non-linear fields in which additional time-dependent acceleration is applied at a location well beyond the ion source where the ions have achieved a substantial separation in space. This has the advantage of allowing the additional acceleration to be tailored to a limited mass range, as opposed to IFF, where all ions are accelerated using the same field.

Static Non-linear Fields

In the static field model, non-linear field gradients are held constant in space throughout the time of ion transit. A number of references exist using non-linear post-source fields to correct for the initial energy spread [5–10], however little has been published regarding the use of non-linear static fields for space focusing. Stein [11] proposed, but did not experimentally verify, that the only field capable of providing perfect axial space focusing would be one in which the force was directly proportional to the distance from the detector. Rockwood presented information at several scientific conferences [12,13] describing a TOF mass spectrometer using an "inverted perfectron" parabolic potential accelerating field for space-time focusing of electrospray generated ions. A diagram illustrating a series of gridless diaphragms along the entire length of the flight path can be found in the author's extended abstract, but no detailed description or evaluation of the perfectron has been published. Hulett and co-workers [14] developed a quadratic potential time-of-flight mass spectrometer for measuring the m/z of ions

generated from the interaction of organic molecules and positrons in a Penning trap. The ions thus formed were accelerated by the application of a quadratic field that extended to the detector and varied with the square of the distance from the detector. This single non-linear field configuration is a special case of non-linear acceleration that takes advantage of the second order relationship between energy and velocity. By placing the detector at the end of the acceleration region, a simple quadratic field was suitable in compensating for initial position. However, a significant disadvantage for this configuration was that the relatively short flight path (61 cm) yielded a relatively short flight time. Consequently, the spectrometer had a resolving power of approximately 10, and ions above mass ~100 were completely unresolved. A second disadvantage for this design was that only the farthest 20% of the ionization volume provided sufficient energy to the ions for detection.

It is apparent that the single parabolic field, illustrated in Figure 4-3, can provide complete space focusing. However, the two shortcomings described above make such an accelerating field inappropriate for a practical, functioning mass spectrometer. First, while in principle, iso-mass ions beginning from any axial point along the flight path of the parabolic field should arrive at the detector simultaneously, those ions beginning from positions close to the detector lack sufficient energy to produce secondary electrons on the detector surface and thus diminish detectability. Practically, only a portion of the parabolic field will provide the required energy. Unfortunately, this is also the region having the greatest electric field gradient, and thus the greatest dispersion as well. Second, parabolic designs do not provide a sufficiently long flight path for adequate separation between ions of successive m/z, and do not allow for the inclusion of
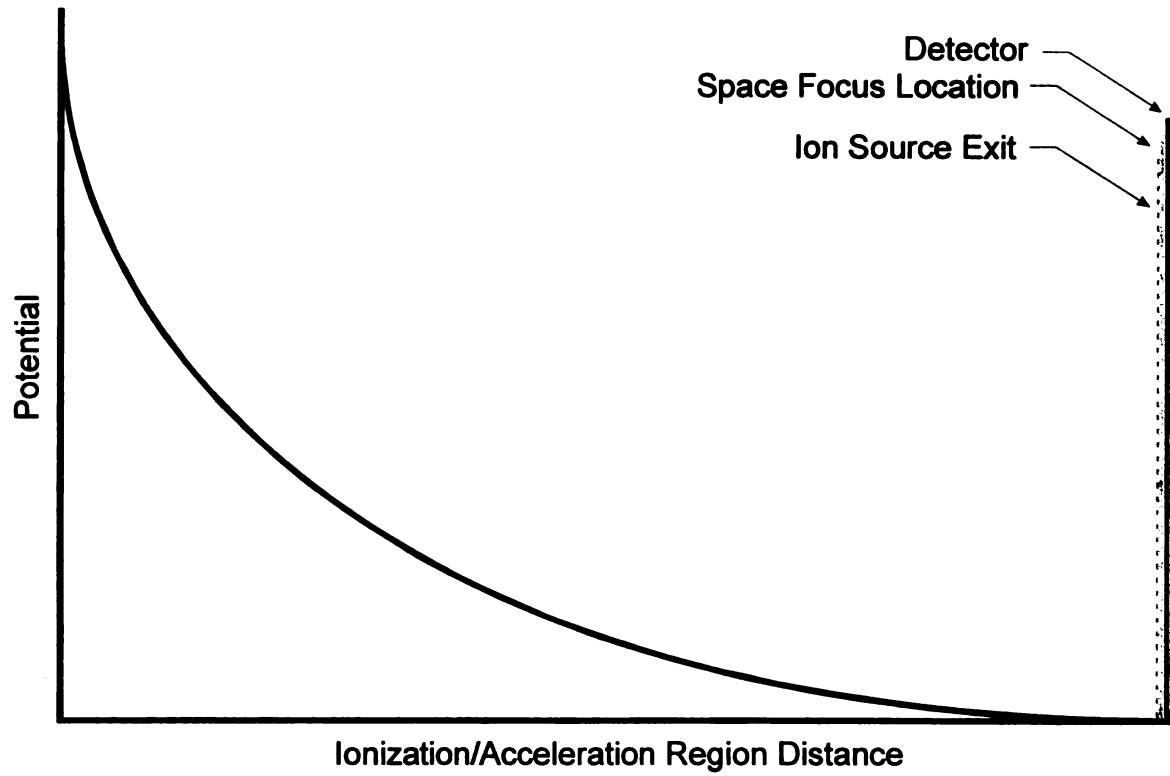
Figure 4-3. Potential profile of a non-linear parabolic field. The entire flight path contains the non-linear potential.

additional energy correction devices such as the ion mirror along the flight path. As will be shown below, an operationally more practical design would include a linear acceleration field to increase overall ion energy for better and more uniform detection, as well as a non-linear region to compensate for initial ion position. This configuration alters the ideal quadratic field of the ion source described by Hulett into various polynomial forms which are a function of ion optical parameters and structural dimensions. The following theoretical modeling and experimental results will confirm that complete space focusing can be realized with the combination of a non-linear field in the ionization region follower by a subsequent linear accelerating field.

Non-parabolic Non-linear Fields

Addition of a linear acceleration region into the overall source design alters the non-linear field in the ionization region from parabolic to polynomial. As illustrated in Figure 4-4, the particular non-linear electric field profile required in a given ion source and mass spectrometer design can be determined by evaluating a series of linear electric fields which, if relatively short in comparison to the overall ion source geometry yield an effectively non-linear electric field. First, using Equations 4-8 and 4-11, the linear accelerating field required to provide the expected time of flight for ions of a given m/z, beginning at the ionization/acceleration region boundary, must be determined. Next, a second, linear electric field segment is calculated for the same ions beginning from a pre-determined distance within the ionization region. Using Equations 4-9, 4-10, and 4-11, the correct second electric field accounts for the fact that the ions will also be accelerated by the previously calculated first electric field. Subsequently the third linear electric field segment is calculated in similar fashion for the same ions, beginning slightly farther back
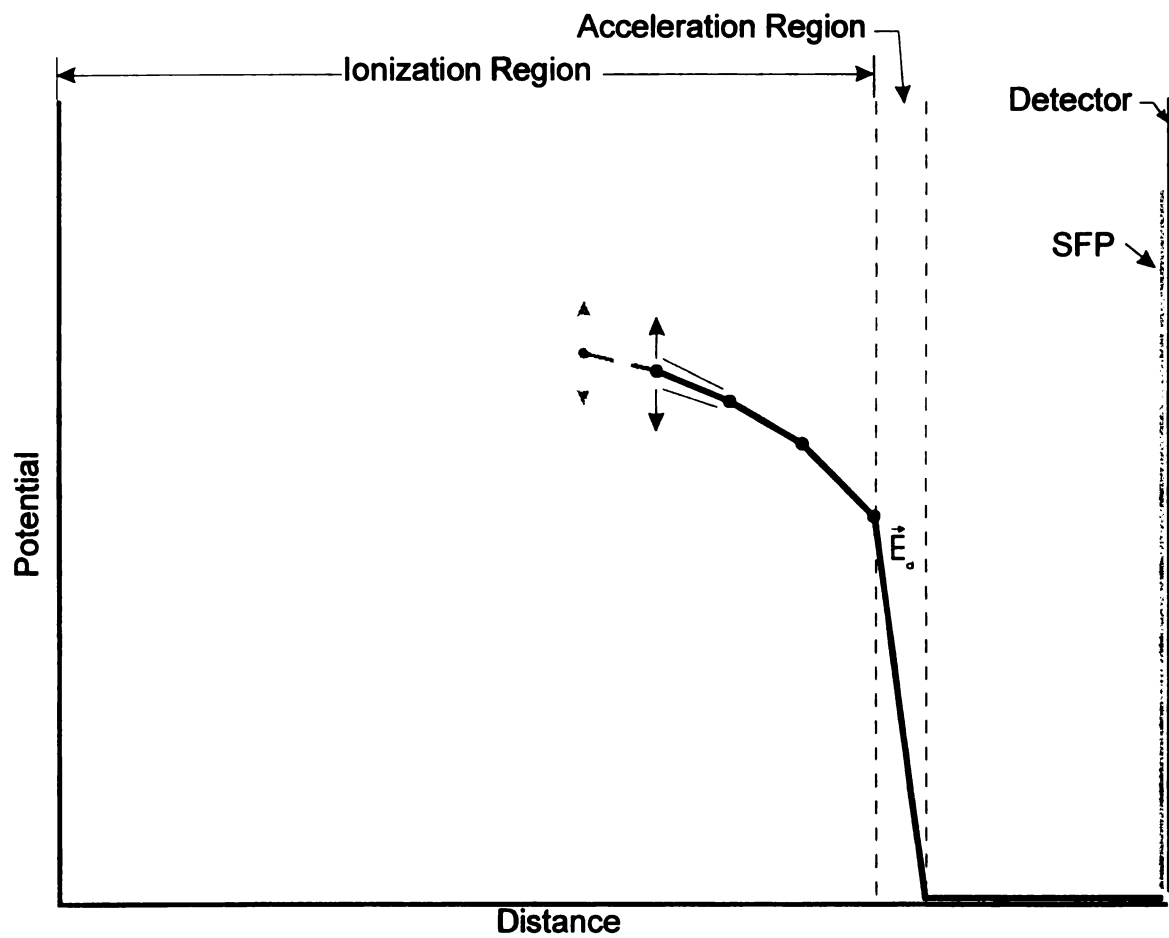
Figure 4-4. Graphical illustration of the method for calculation of the appropriate non-linear field required for ideal space focusing where the detector is some distance from the ion source exit and a linear acceleration region is included. Each electric field segment is calculated by successive approximation.

in the ionization region, incorporating an equation similar to Equation 4-10 that accounts for the third electric field and the fact that the ion will be subsequently accelerated by the both of the previously calculated electric fields. Determination of the nth electric field occurs in the same manner. As the time of flight for an ion beginning anywhere in an ion source having n fields is

$$t = \sqrt{\frac{2m}{q}} \left[\sum_{n=1}^{l} \frac{\sqrt{U_0 + q\sum_{j=n}^{l} x_j E_j} - \sqrt{U_0 + q\sum_{k=n+1}^{l} x_k E_k}}{E_n} + \frac{D}{2\sqrt{\sum_{i=1}^{l} x_i E_i}} \right]$$ (4-20)

where the indexes i, j, k and l, serve as computational counters, the final electric field segment n can be easily determined. Equation 4-20 is merely a continuation of the derivation of Equation 4-8, and the validity of this approach to non-linear field determination was recently verified by Yefchak [15]. As shown in Figure 4-5, the idealized non-linear field profile is sigmoidal. The non-linear field in the region farthest from the ion source exit retains a quasi-parabolic shape, with a diminishing rate of change in the electric field moving toward the exit. This is followed by an inflection in the electric field profile and subsequently, a narrow region just before the ionization/acceleration region boundary, where the rate of change in the electric field increases sharply.
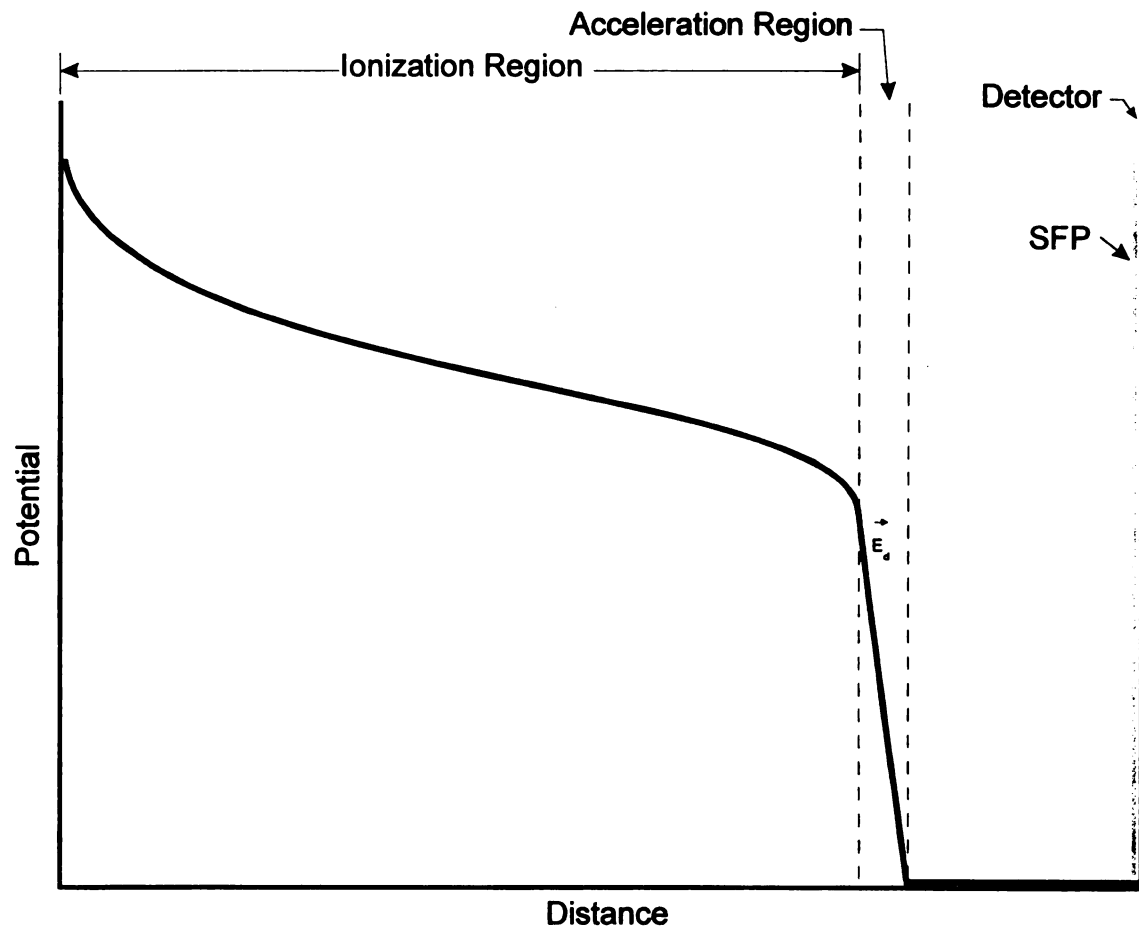
Figure 4-5. Non-parabolic non-linear acceleration scheme employing a linear acceleration region in combination with a non-linear ionization region.

In order to evaluate the electric field parameters for non-linear ion acceleration with a given ion source configuration, a computational program based on Equation 4-20 was written in the C++ programming language. This program, listed in Appendix A as TOFSOURC3.CPP, calculates the electric field and absolute axial voltages required within the ionization region to provide ideal space focusing. These fields are determined using a successive approximations algorithm where the value for a given electric field segment is repeatedly modified until the desired flight time for a given ion is achieved to within a specified tolerance. The program is designed to allow the incorporation of multiple fields, with the accelerating region having a distinct axial dimension and the ionization region having mono-incremental field segments. Operation of the program occurs by inputing values for the total flight time t, drift region distance D, accelerating region length d, step size between ionization region increments, mass, and charge. The program is then compiled and an output data file generated, in txt format, listing the axial position and electric field requirement.

Three major parameters, flight time, drift distance, and acceleration region length, effect the overall ion source theoretical voltage profile. Figure 4-6 illustrates the effect of varying the total flight time, using an ion source configuration having a 0.50 cm accelerating region length and a 153 cm drift length. As the required flight time is reduced from 30 μsec to 15 μsec, the required potential within the ion source increases, as expected. Importantly, the overall shape of the non-linear ionization region potential is specific to the physical dimensional parameters, with only the amplitude being directly related to the desired flight time. The effect of varying the physical dimensions is illustrated in Figure 4-7 and Figure 4-8. The effect of varying the distance between the

ion source exit and the space focus plane at the detector under the condition of constant flight time is illustrated in Figure 4-7. For a flight time of $t=8$ μsec and an acceleration region distance of $d=0.50$ cm, an increase in drift region distance requires a greater initial ion source potential, as expected. Additionally, the overall potential profile in the ionization region is significantly different for each case. In the D=5 cm case, the inflection point in the potential profile occurs close to the ion source exit at $\sim s=1$ cm. For the D=50 cm case, the inflection point is significantly farther back in the ion source at $\sim s=8$ cm. The presence of an inflection point in each profile is typical of non-linear acceleration when a secondary linear accelerating region is included. Finally, the dependence of the potential profile on the linear accelerating region length is illustrated in Figure 4-8 where, as the accelerating region length is increased, the potential profile of the non-linear region becomes less sigmoidal and more parabolic in function.

As indicated above, the theoretical calculations, even under broad parameter perturbations, confirm that complete space focusing should be able to be achieved with a non-linear ion source region followed by a linear acceleration region. Practically, this appears to be achievable over a range of physical dimensional parameters, which implies that the design of the potential profile as well as the ion optical parameters could be tailored to meet specific mass spectrometer design and performance requirements. This flexibility represents a significant advantage over strictly parabolic-field designs.

a)
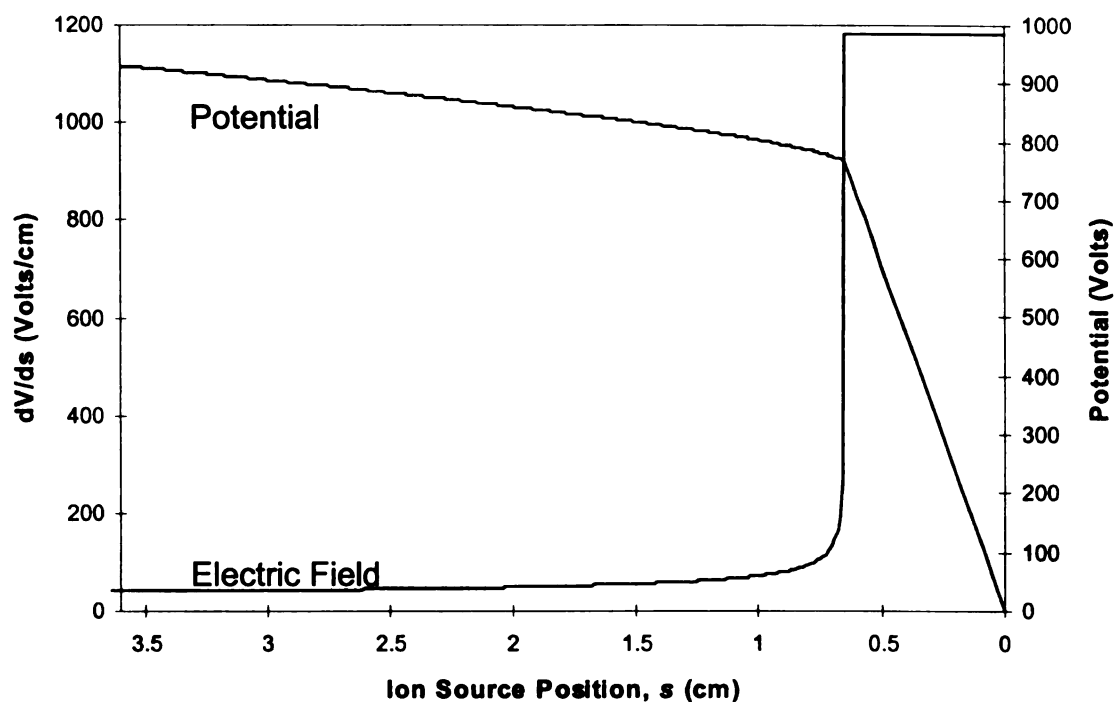
b)
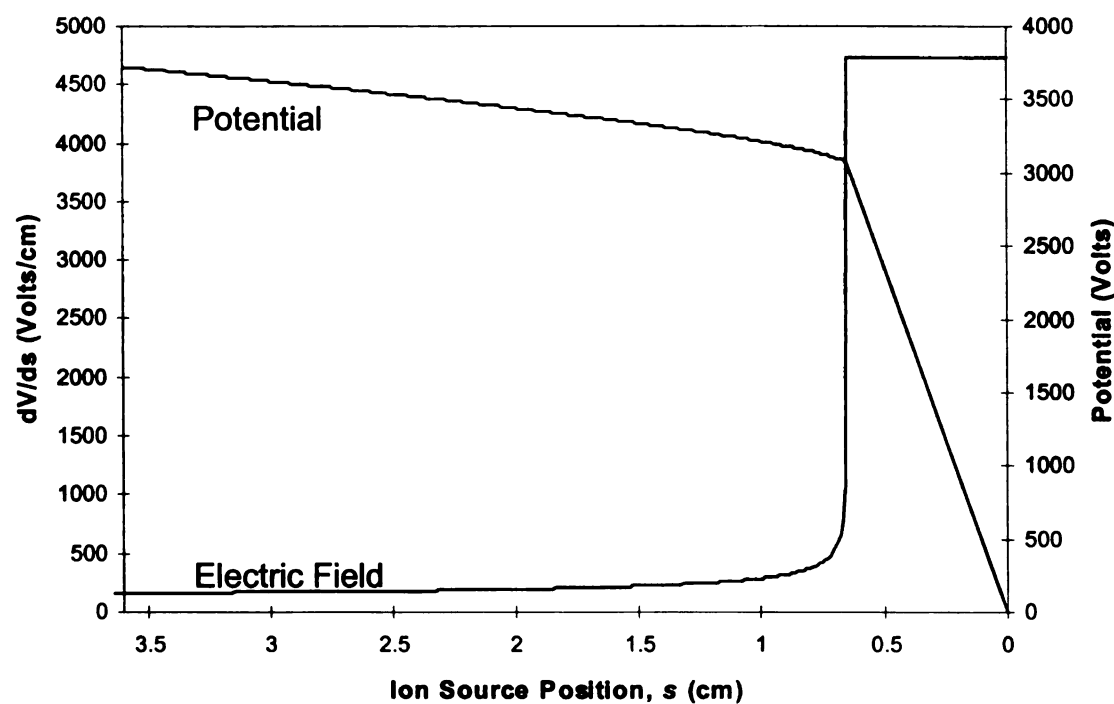
Figure 4-6. Calculated electric potential and field gradients required to achieve complete space focusing at specific ion flight times for m/z 56, D=153 cm, d=0.50 cm, for a) t=30 msec and b) t=15 msec.

a)
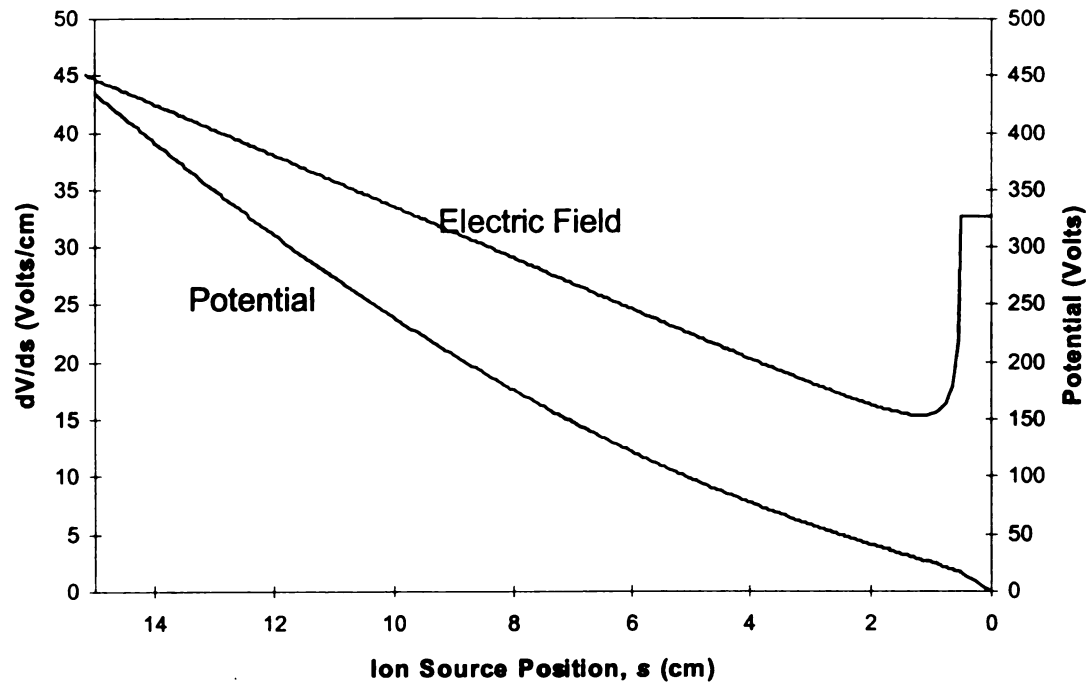
b)
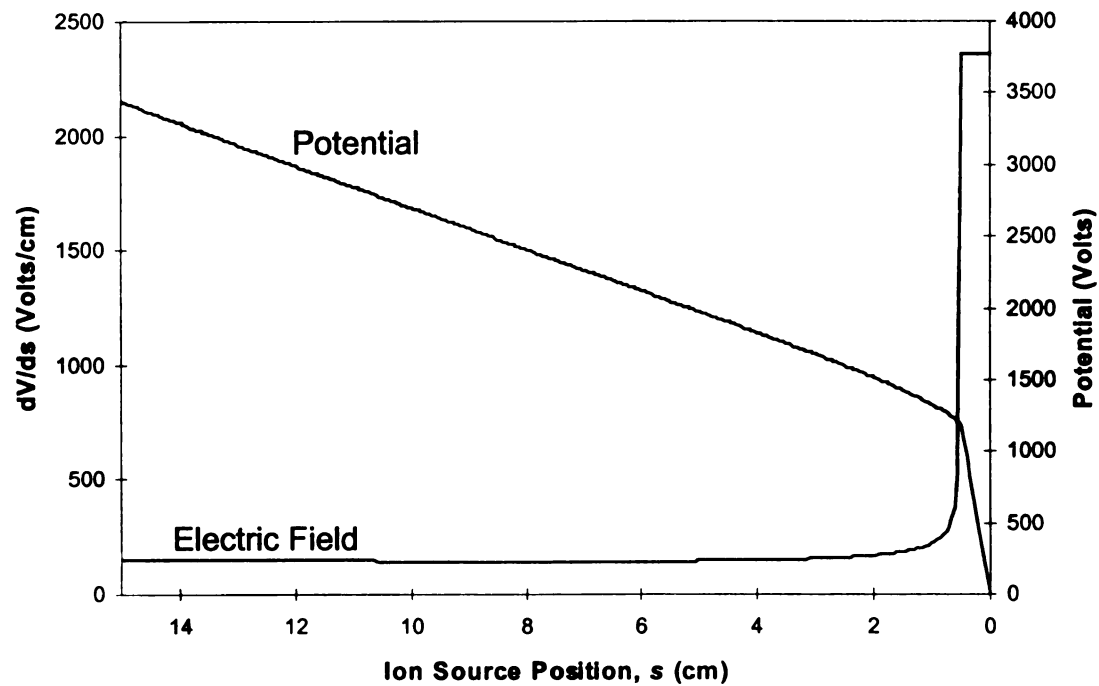
Figure 4-7. Calculated electric potential and field gradients required to achieve complete space focusing at specific drift region distances for m/z 56, t=8 msec, d=0.50 cm, for a) D=5 cm and b) D=50 cm.

a)
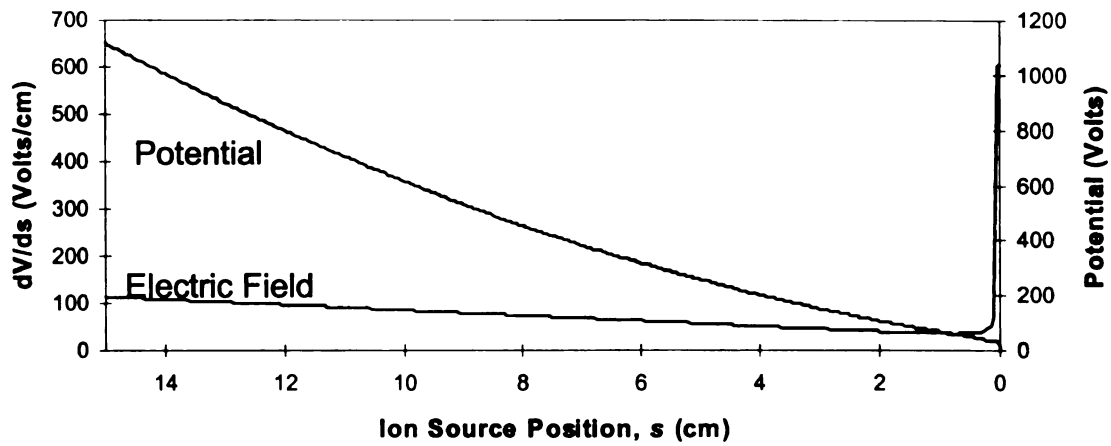
b)
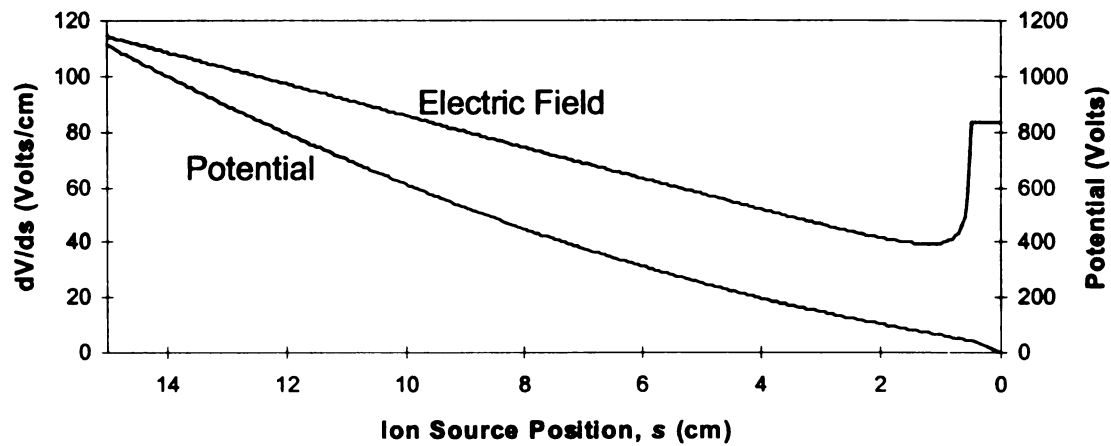
c)
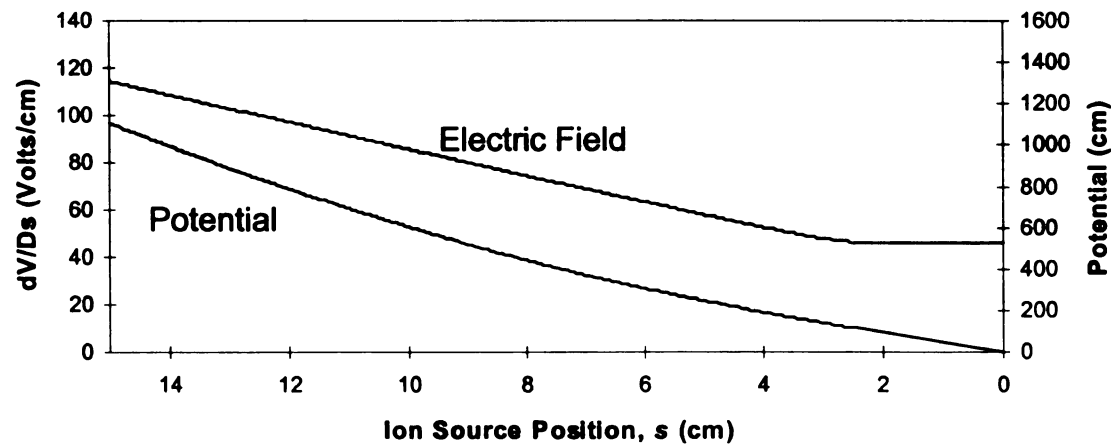
Figure 4-8. Calculated electric potential and field gradients required to achieve complete space focusing with specific ion source acceleration region dimensions, for *m/z* 56, D=153 cm, t=5 msec, where d= a) 0.05 cm, b) 0.5 cm, and c) 2.5 cm.

Experimental

A mass spectrometer suitable for evaluating the theoretical models of linear and non-linear ion acceleration was designed and fabricated in house by this author. The system consists of a linear time-of-flight mass spectrometer with an open-geometry ion source through which laser induced photo-ionization can be achieved at specific locations within the ionization region of the source to selectively probe and evaluate ion acceleration behavior. The ion source consists of multiple closely spaced ring electrodes electrically biased using voltage divider circuits to generate linear fields and, by means of a series of short, linear, electric field segments, an approximation of non-linear fields.

Experimental Apparatus

Vacuum System

The mass spectrometer, illustrated in Figure 4-9., was designed as a test platform for a variety of ion source configurations. The ion source chamber consisted of a stainless steel 6-way cross (6 ¾" tube diameter, MDC Manufacturing Co.) with Conflat style flanges, and was vacuum pumped using a 800 L/s (N_2) diffusion pump (Edwards, model 160). The analyzer region consisted of a 2-meter length of 6 ¾" diameter stainless tube vacuum pumped using a 322 L/s (N_2) diffusion pump (Edwards, model 100). Both diffusion pumps were backed by a single roughing pump (Alcatel, model 1020). A 1 ½" diameter aperture was located between the ion source housing and analyzer region to facilitate some measure of differential pumping between the two vacuum regions during analysis. Vacuum was measured using two Bayer-Alpert style vacuum gauges, one located at the ion source housing and one located near the throat of the analyzer region diffusion pump, using a Hewlett Packard 5945A
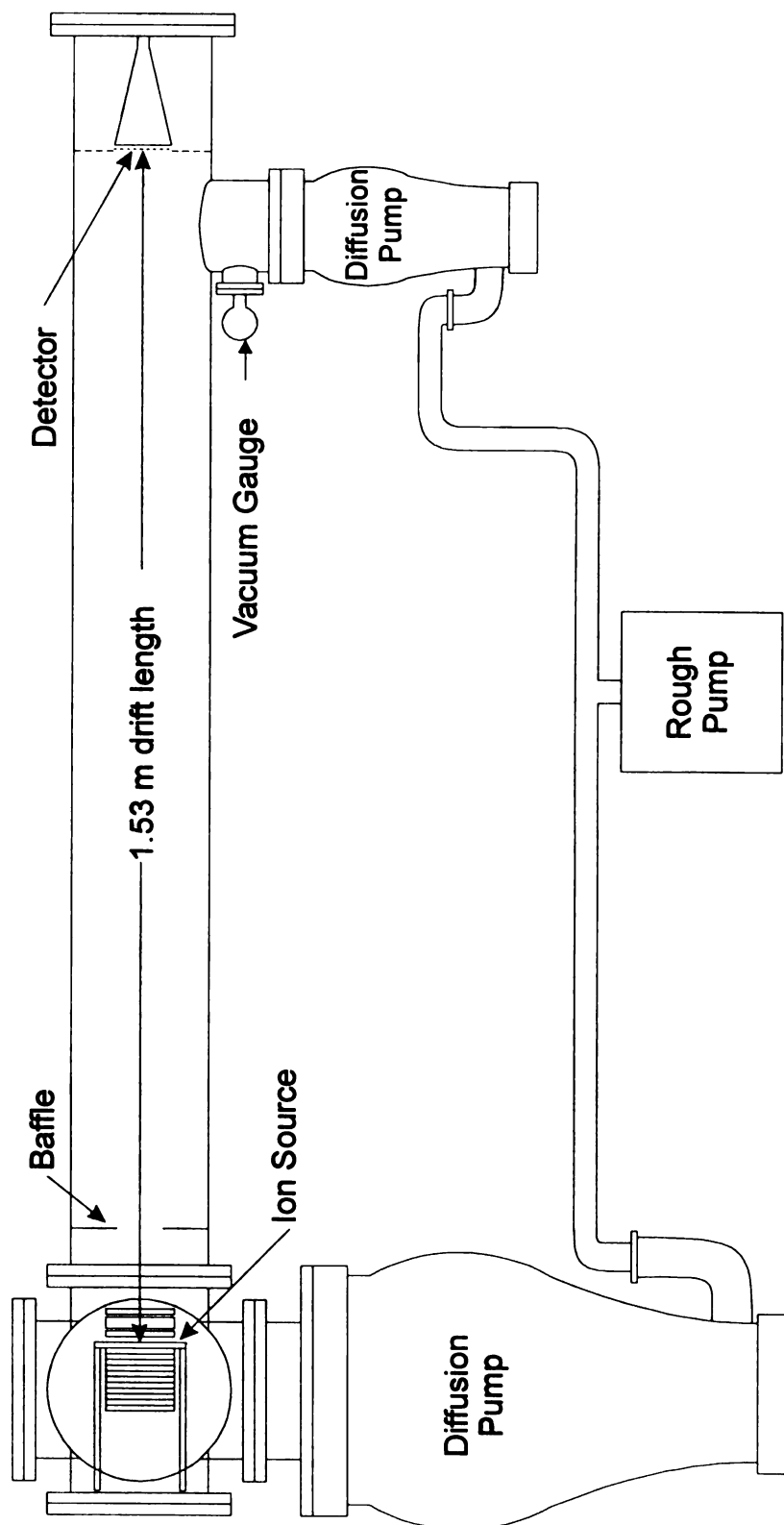
Figure 4-9.

Figure 4-9. Time-of-flight mass spectrometer; configuration and vacuum assembly.

gauge controller. Under normal operating conditions with no analyte being introduced into the vacuum system, the base pressures achieved were 2×10^{-7} torr and 9×10^{-8} torr for the ion source and analyzer regions, respectively.

Detector

The detector, located at the end of the analyzer region just beyond the diffusion pump flange, consisted of a micro-channel plate chevron assembly (Galileo Electrooptic) mounted on a Conflat style flange. All electrical connections were made through this flange, and the entire detector assembly was electrically shielded from the analyzer region using a 6.50" diameter screen, gridded to facilitate vacuum pumping, and a 1.50" diameter center aperture covered with 90% transmission electroformed grid mesh (Buckbee Mears) to minimize ion transmission loss. The voltage applied to the detector for the experiments described below was -1350 V.

Ion Source Platform

The ion source mounting platform, as shown in Figure 4-10, consisted of a 6.00 inch diameter brass stage mounted 6.25 inches from the ion source flange. The stage had a 1.06" diameter mounting ring for ion source attachment located on the flange side, and an Einzel lens and deflection plate assembly located on the analyzer side. All electrical connections for the ion source, Einzel lens, and deflection plates were made through the ion source flange.

Laser and Optical System

Gas phase analyte molecules were photo-ionized using a laser and a series of optical elements to direct and shape the beam. The system consisted of a Quanta-Ray GCR-11

Nd:

prov

outp

dura

A

optic

adjus

cylinc

betwe

targete

5-mm

throug

chamb

was m

in Figu

laser b

optical

Nd:YAG laser with a model HG-2 harmonic generator and model DHS-2 splitter set to provide a laser wavelength of 355 nm. The laser was fired at a rate of 10 Hz with an output power of 45 mJoules as measured with an Ophir laser power meter. The firing duration was approximately 5–6 nsec.

An optical rail, mounted on an ion source chamber flange, housed the beam guiding optical components, which consisted of two high-reflection aluminum mirrors on adjustable mounts and a vertically oriented cylindrical lens on a fixed mount. The cylindrical lens focused the beam into a slit image which made it narrow enough to pass between the ion source electrodes and increased the photon density in the space being targeted for ionization. The adjustable mirrors provided the flexibility for guiding the 5-mm diameter collimated beam from the laser, located on a separate portable cart, through the cylindrical lens and ultraviolet transmitting viewport into the ion source chamber. One mirror and the cylindrical lens were mounted on a sliding assembly which was moveable along a single axis oriented in parallel with the ion optical axis, as shown in Figure 4-10. The optical path could thus be adjusted so as to place the focal line of the laser beam at the axial center of the ion source while precisely positioning it along the ion optical axis at pre-selected points of ionization.

F
be
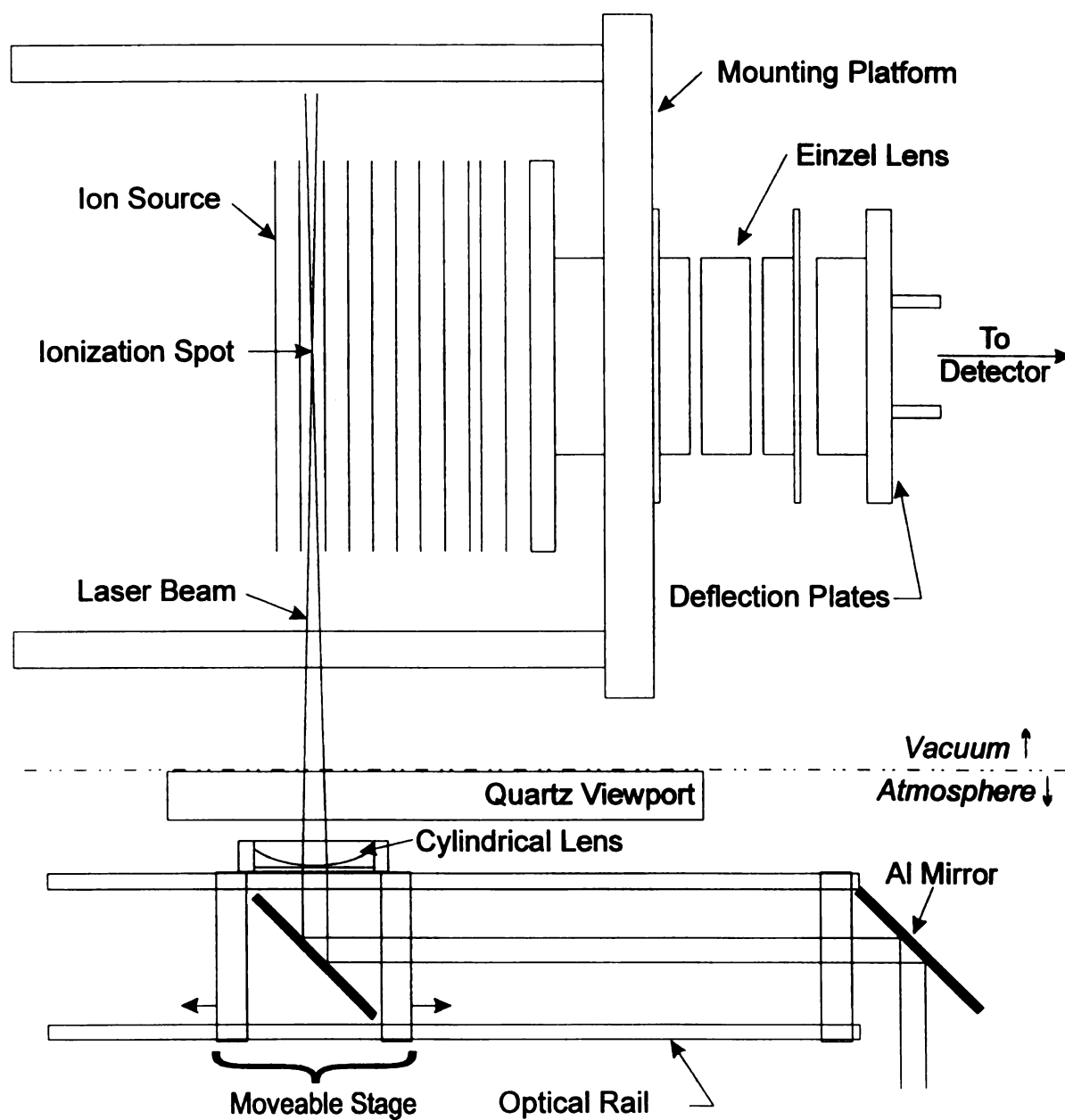
Figure 4-10. Laser optical and ion optical assemblies. The ionization spot is positioned between ion source electrodes by adjustment of the moveable stage along the optical rail.

Ion So

The

from 0.(

machin

diaphra

within t

used on

except

the bacl

The sou

except

region e

Samp

The

(approx

needle

which c

ion sou

interloc

Powe

The

voltage

voltage

Ion Source

The ion source electrodes consisted of 3.00" outer diameter diaphragms constructed from 0.017" thickness stainless steel sheet, cut into rings by the MSU physics department machine shop using a wire EDM. Two inner diameters were used; 0.50" for the diaphragms at each end of the accelerating region and 1.75" for the diaphragms used within the ionization and acceleration regions. Electroformed grid mesh identical to that used on the detector assembly was spotwelded over the opening in each diaphragm except for one in the accelerating region which was left grid free. The final electrode at the back of the ion source was solid. The ion source assembly is shown in Figure 4-11. The source electrodes were mounted in a stack separated by 0.100" ceramic spacers except for the spacer separating the accelerating region electrode and the first ionization region electrode, which was 0.030" thick sapphire.

Sample Inlet

The sample introduction assembly was constructed using a small glass sample vial (approximately 2 mL volume) with a ¼" diameter neck swaged to a vacuum capable needle valve. The valve was attached to a 12" length of ¼" diameter stainless tubing, which completed the assembly. Sample was introduced to the vacuum environment of the ion source housing by inserting the stainless tubing through a direct probe vacuum interlock and opening the needle valve.

Power Supplies

The detector power supply was a Bertam Associates, Inc. Model 603-50N 5 kV high voltage supply. The Einzel lens was supplied by a Gamma High Voltage Research high voltage power supply, model RC10-5N/VM 5 kV . The deflection plates were powered
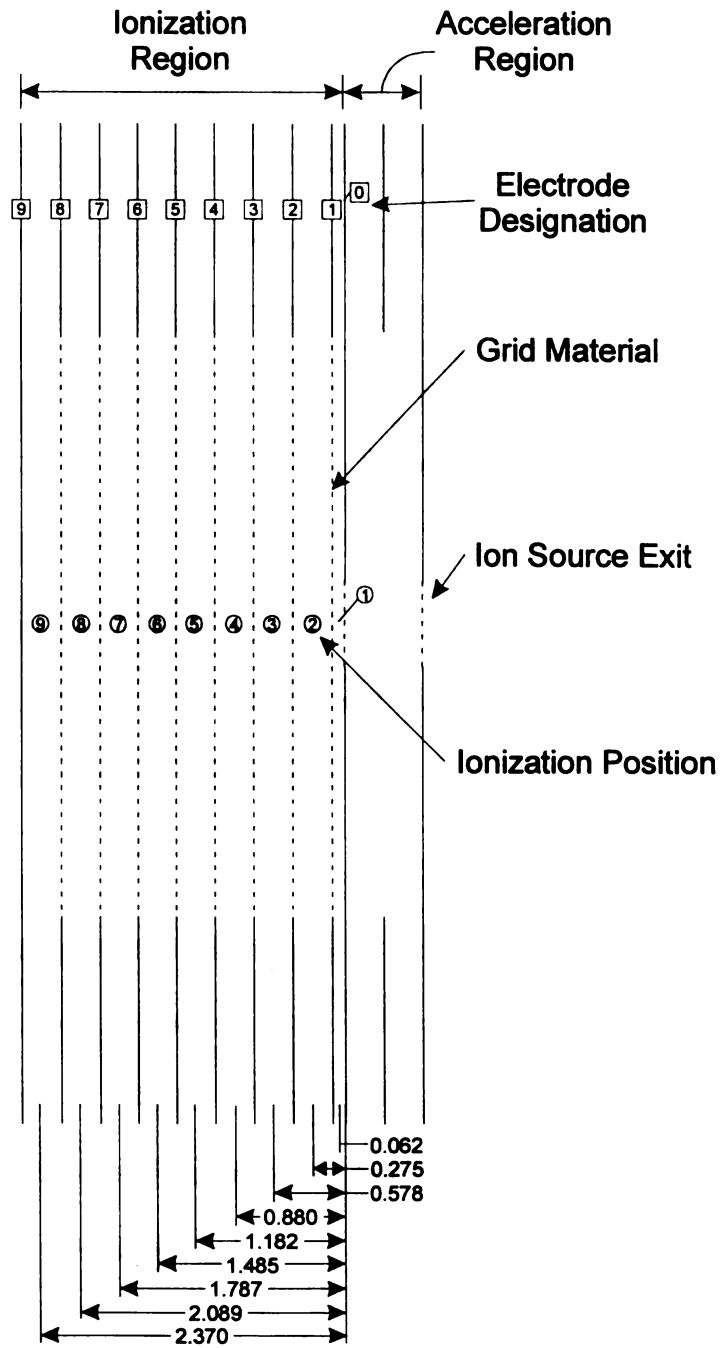
Figure 4-11. Ion source assembly. Measurements shown are in cm.

using a Hewlett Packard 6207B DC 0–160 V, 0–0.2 A power supply. Ion source voltages were supplied using a Glassman model ER, 3 kV, 100 mA high voltage power supply. The output of this power supply was connected to the voltage dividers described below.

Voltage Dividers

Two voltage dividers were constructed using a resistor network. The linear divider, as shown in Figure 4-12a, supplied a linear electric field to both the acceleration electrodes and the electrodes in the ionization region. The voltage applied to the electrode dividing the ionization and acceleration regions could be varied using a 500-kΩ potentiometer, allowing the ratio of the two electric fields to be varied and thus enabling the space focus location to be optimized at the detector.

The non-linear divider, shown in Figure 4-12b, also used a resistive network with fixed resistors providing the base divisions, and potentiometers included for the ionization region electrodes to allow fine tuning of the required voltages.

Transient Recorder

Data were collected using a 500-MHz, 2.5-GS/sec Tektronix TDS 620B, two-channel digital real-time oscilloscope. The oscilloscope was used in a variable delay mode set to observe the dominant ion peak, with a 16-shot moving average of successive laser pulses being recorded over a 2-μsec time window. Each data set was saved as an ascii file and downloaded to diskette for subsequent analysis.
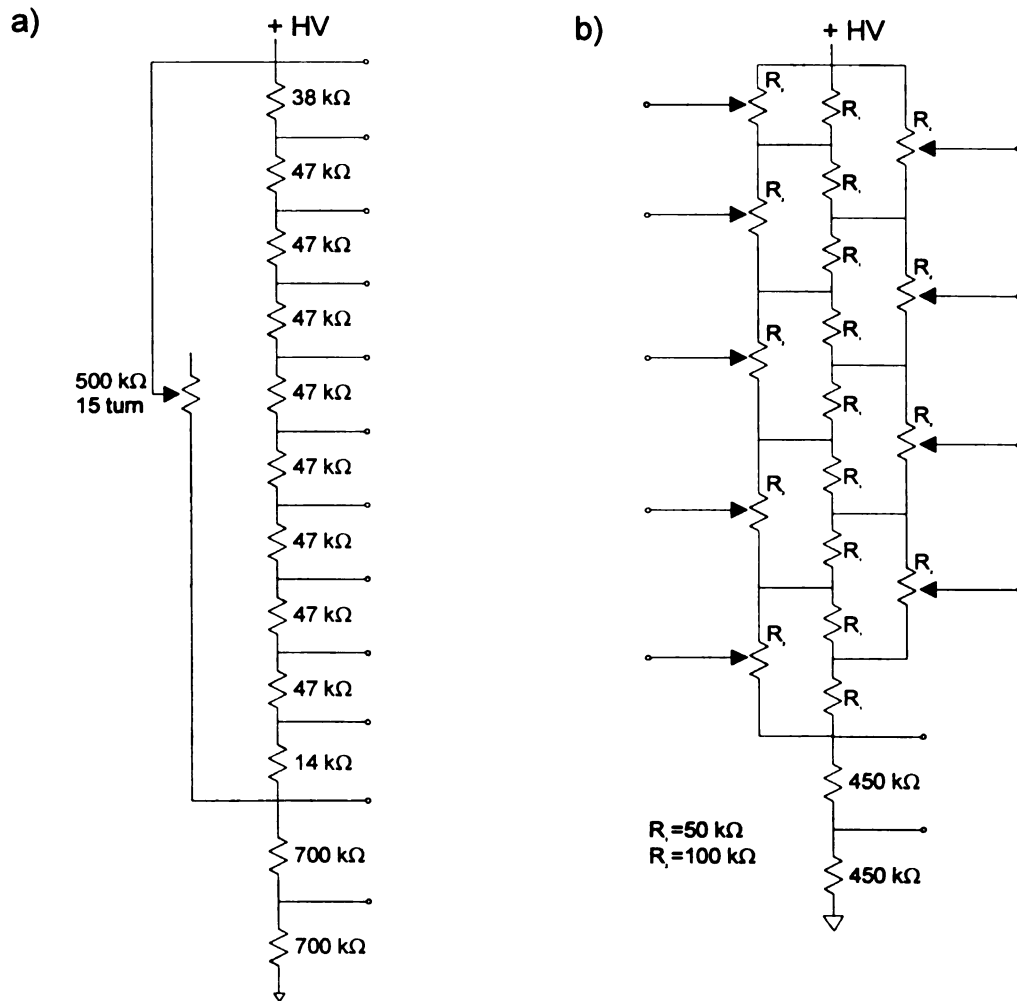
Figure 4-12. Resistive divider networks used for a) linear and b) non-linear ion source configurations.

E

Li

fie

ar

fo

A

ac

io

al

po

N

ap

in

a

v

o

f

ta

s

a

a

Electric Field Calculations

Linear Configuration

A program calculating the ion arrival-time distribution expected when using a linear field ion acceleration model was written in MathCad 4.0 [16] and used to compute the arrival-time profiles expected over a series of ionization/acceleration electric field ratios for the instrument configuration described above. This program is included in Appendix A as LINEAR.mcd. Given a set of analytical parameters (m/z, d, D, accelerating voltage, total voltage), the program calculates the fight time for a selected ion beginning at the acceleration field/ionization field boundary as well as anywhere along the ionization region axis. It then generates a graph of arrival time vs. initial ion position as well as a tabular output file.

Non-linear Configuration

A second program calculating the series of electric fields required to provide the approximation of ideal space focusing was also written using MathCad 4.0 and is included in Appendix A as NONLINEAR.mcd. This program is based on Equation 4-20, and is similar to the program TOFSORC3 in that it calculates both the electric field and voltage required for each ion source segment. However, this program calculates the series of linear electric fields required to provide co-temporal flight times for ions beginning from a pre-selected set of inter-electrode positions. Both the electrode spacing and the targeted inter-electrode ionization position are specified prior to calculation. The program subsequently calculates the arrival times expected for ions originating over the entire axial space between electrodes. Each of the mass spectrometer dimensional parameters are included in the program (analyzer path length and ion source dimensions) as are the

analytical parameters (mass, charge, and accelerating voltage). The program first calculates the flight time of a given ion having no internal energy and located along the analytical axis of the ion source at the acceleration/ionization field boundary. The program then successively calculates the optimal electric field required for each ionization region given the optimal electric fields calculated for all previous ionization region segments.

Experimental Method

The experiments were conducted using the laser to photo-dissociate gas phase analyte molecules located within the designated ionization region of the ion source. $Fe(CO)_5$ was chosen over an organic molecule as the analyte due to its combination of relatively high ionization cross section, relatively low first ionization potential (7.9 eV) [17], and its volatility at room temperature. The time-of-flight mass spectrum of femtosecond laser photo-induced dissociation of $Fe(CO)_5$ at $\lambda=400$ nm has recently been reported [18], and Fe^+ was described as the predominant ion species after 500 femtoseconds irradiation time.

The analyte was leaked into the ion source housing through the direct inlet assembly, yielding vacuum levels of 3×10^{-5} torr in the ion source housing and 6×10^{-6} torr in the flight tube. The laser was then fired at 10 Hz with the moveable mirror and cylindrical lens set to aim the laser beam between two of the ionization region electrodes. The arrival time of the dominant peak in the spectrum was measured using the oscilloscope. Once the oscilloscope had collected a minimum of 16 transients and averaged them, the laser beam was blocked, the data recorded, and the mirror and lens assembly moved a pre-measured distance to allow the sampling of the ionization space between the next electrodes. Nine locations within the ion source were sampled in each data set.

The ion peak shown in Figure 4-13 exhibits a flight time corresponding closely to the expected average arrival time of singly charged ^{56}Fe, which accounts for 91.8% of the isotopic abundance of Fe. For an accelerating voltage of 1629 V and total potential of 1887 V the expected arrival time was 21.35 μsec starting from ionization region position 5. The measured arrival time under these conditions was 21.20 μsec. Also observed are smaller peaks at 20.82 μsec and 21.39 μsec which correspond to ^{54}Fe and ^{57}Fe and account for 5.8% and 2.1% of the Fe isotope abundances, respectively. While the system remained uncalibrated during the analyses and thus any electronic timing offsets were unaccounted for, the experimental goals did not require explicit knowledge of any ion peak identity. It was sufficient to monitor the same peak throughout the experiment, regardless of the m/z.

Evaluation of linear configuration

Three sets of data were collected with the ion source configured to provide linear electric fields at three different ionization/acceleration electric field ratios. The expected arrival time distributions were calculated by the LINEAR program, using the analytical parameters listed in Table 4-1. A minimum acceleration field potential of 1600 volts was required to achieve an observable detector signal, and thus served as the lower limit for all experiments. The data correspond to the measured arrival time of the peak apex for m/z 56 ions. Example graphs of the original recorded data are shown in Figure 4-14 and illustrate the difference in arrival times observed among the various sampled ionization regions.
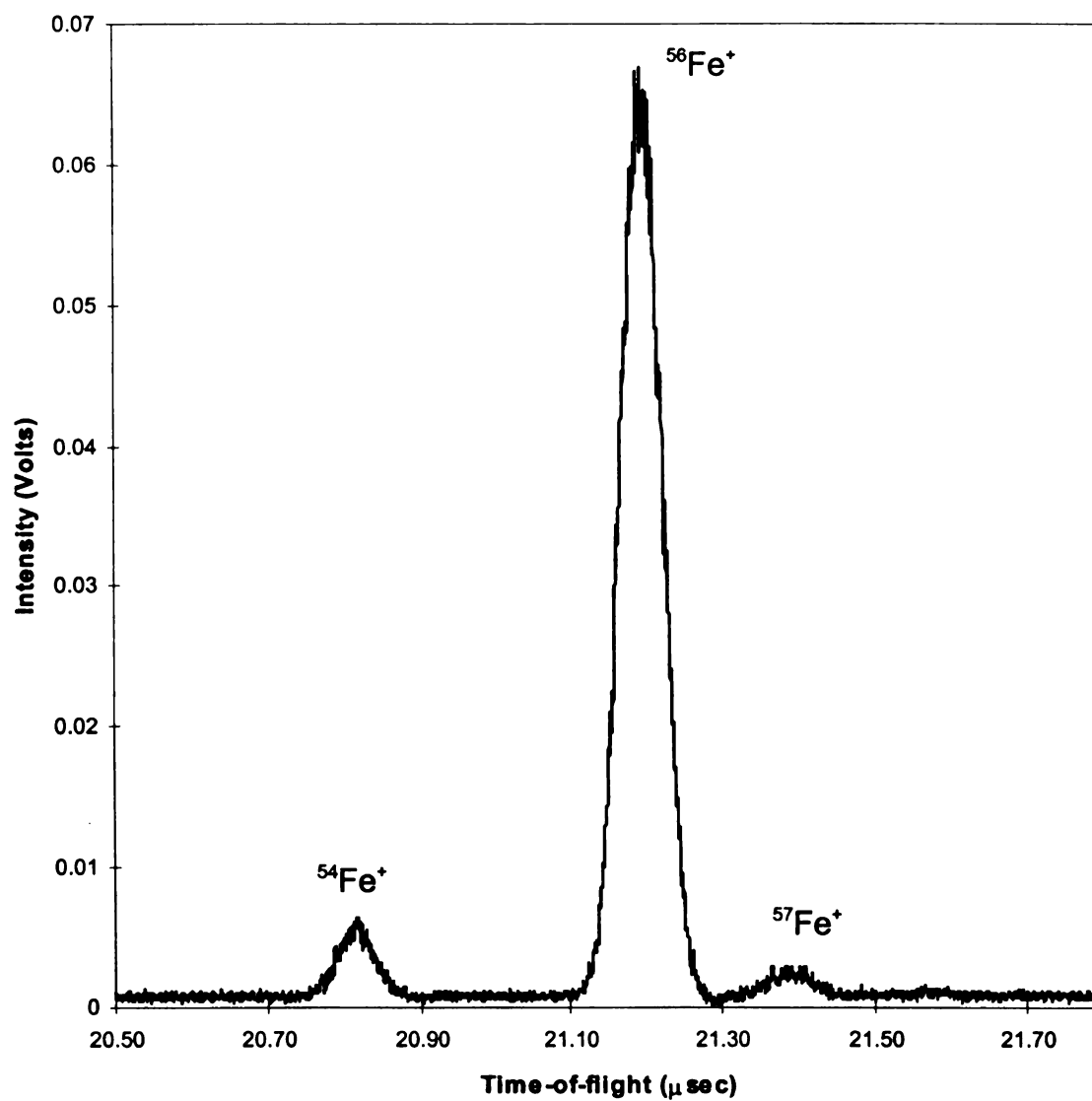
Figure 4-13. Typical mass spectrum of Fe^+ isotopes using the linearly configured ion source. The resolving power is ~180.

Mass, *m*	56 u
Charge, *z*	1
Drift Distance, *D*	153 cm
Acceleration Region Distance, *d*	0.648 cm
Total Potential, *V1*	1887 V

Table 4-1. Analytical parameters used to calculate the voltages and electric fields required to provide linear acceleration.

Using the analytical equations for ion motion (Equation 4-12), the predicted arrival time distributions of *m/z* 56 ions, along with the experimentally obtained data, are plotted in Figure 4-15 as a function of initial ionization location and ionization region/acceleration region ratio. These ratios are listed in Table 4-2.

Accelerating Voltage	Back Plate Voltage	Electric Field Ratio
1605	1887	21.96
1629	1887	24.36
1710	1887	37.27

Table 4-2. Electric field ratios used with linear acceleration experiments.

The theoretical traces exhibit a curvature due to the arrival time distribution expected when using a multi-linear-field ion source configuration. The magnitude of this curvature is a function of the electric field ratio which controls the axial location for space focusing. The curve corresponding to the electric field ratio of 37.27 exhibits an increase in ion arrival time as the initial position is moved back in the source, which is a consequence of the space focus region being positioned beyond the detector surface. The curve identified
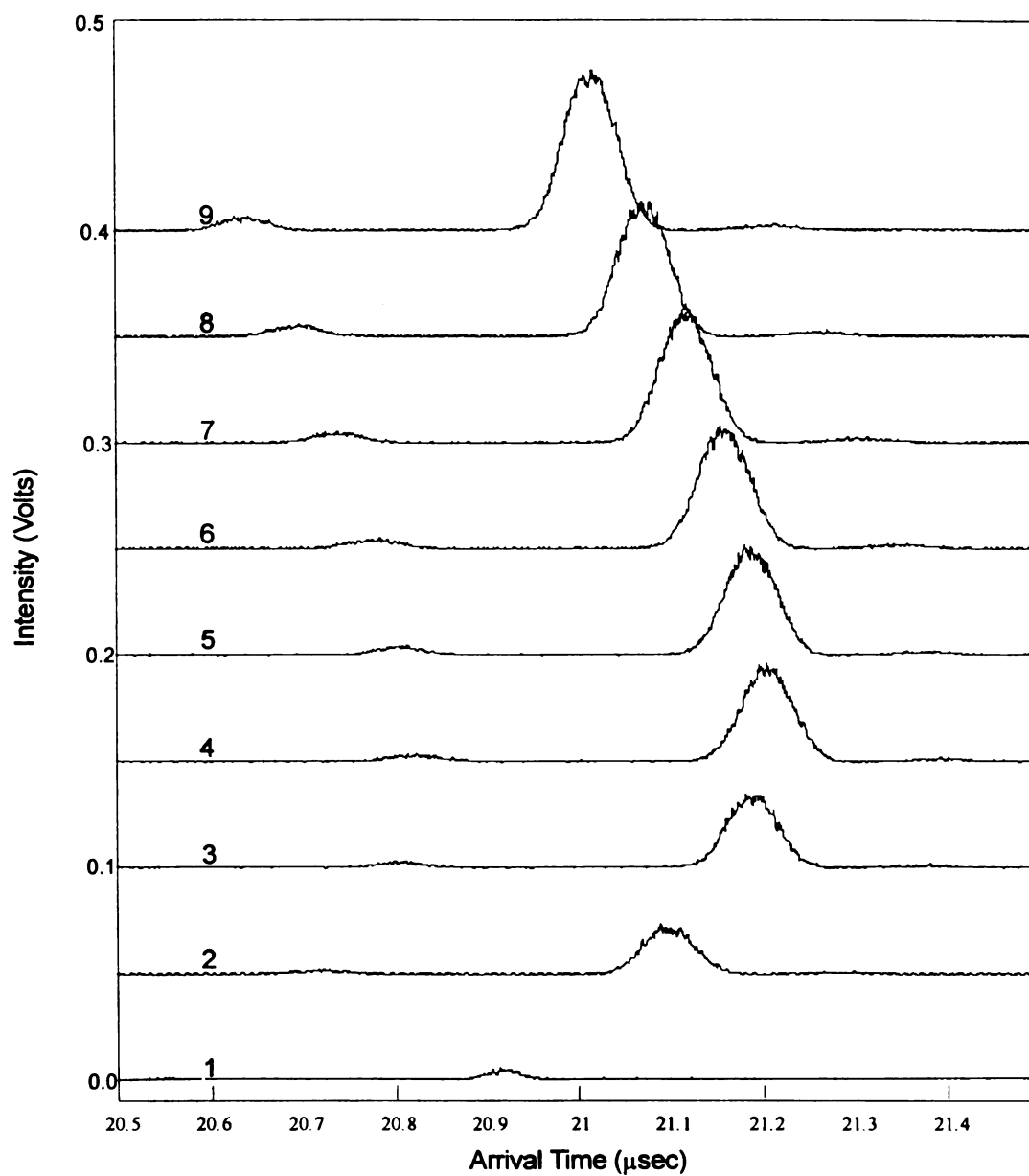
Figure 4-14. Arrival time distributions for Fe$^+$ ions originating from various ion source locations. The ion source was configured for linear acceleration, with 1639 V applied to the acceleration region and 1887 V applied to the source backplate.

as having an electric field ratio of 21.96 shows a generally opposite trend where, while the ion arrival time increases initially as the position moves back in the ionization region, a maximum arrival time occurs fairly close to the ionization region exit and the ion arrival time subsequently decreases as the initial position is located farther back in the source. This trend of ion arrival time decreasing with increased initial position is expected when space focusing occurs some distance before the detector location. The optimum ion arrival time distribution, shown in Figure 4-15 as the 24.36 ratio, exhibits the minimum absolute arrival time range over the entire ionization region, with a total temporal distribution of 227 nsec. This is achieved when the ion source electric field ratio is optimized, and corresponds closely to the optimal ratio predicted by Wiley and McLaren.

In each case, the experimentally derived data agree closely in overall curvature with the theoretical data. This strongly supports the first-order space focus model and is the first data to confirm the predictions of ion behavior originally proposed by Wiley and McLaren. Only two minor discrepancies are present, and neither of these diminish the strength of the data obtained. First, the arrival times for the experimentally derived data were on average approximately 160 nsec earlier than predicted, which might be attributable to either an offset in the electronics circuitry or a discrepancy between the measured and actual flight-path distance. To aid in the comparative evaluation, this offset was added to the arrival time observed in each data set. Second, it is also observed that while the experimental data exhibit the same overall curvature as the theoretical data, the experimental data appear to be shifted to the left . This could easily be attributed to any misalignment of the laser beam, which if not oriented orthogonal to the ion source, would result in the ionization position being axially displaced.
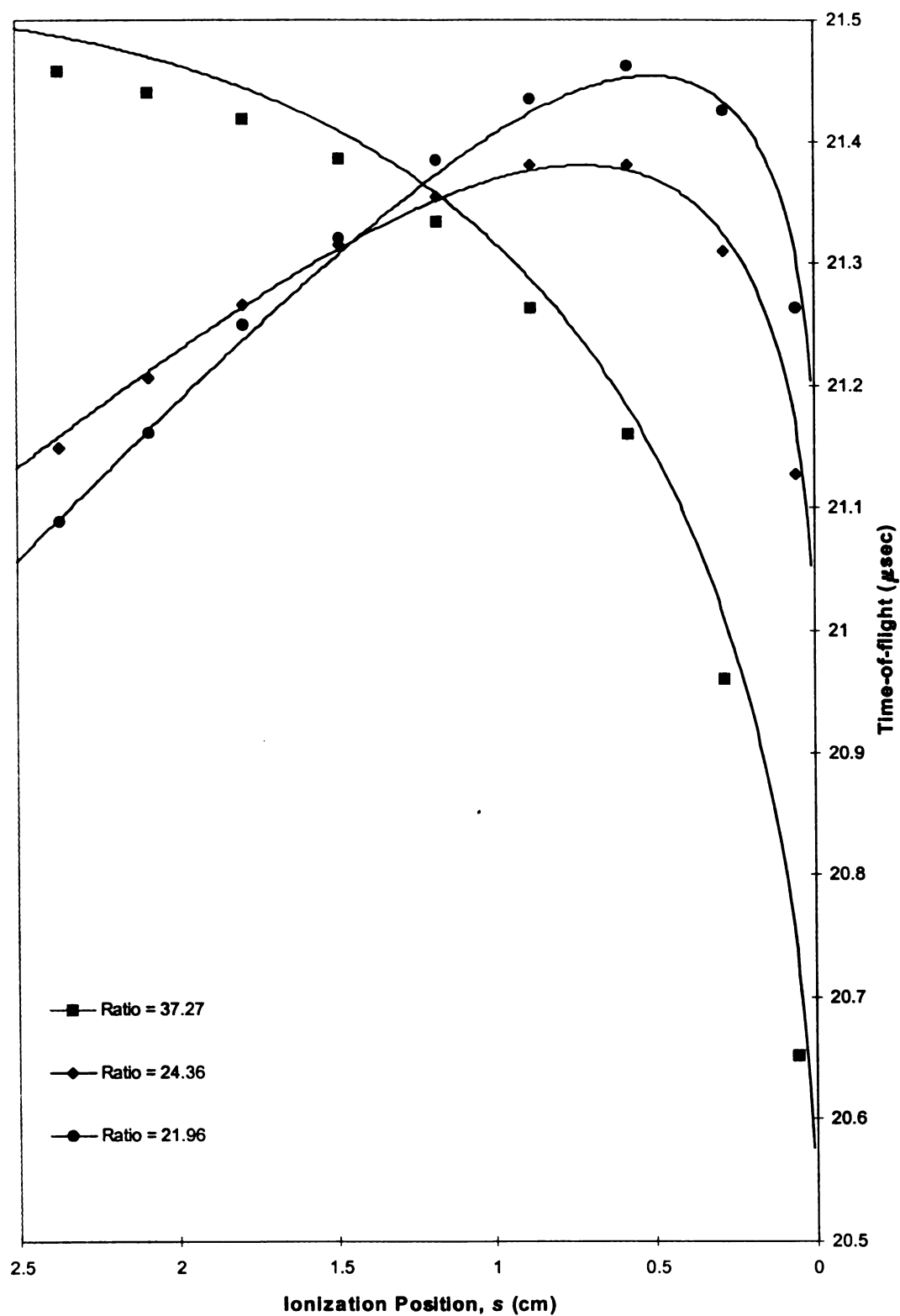
Figure 4-15. Theoretical and experimental ion arrival time data for *m/z* 56, D=153 cm, d=0.648 cm, at three acceleration field/ionization field ratios.

Evaluation of Non-linear Configuration

Expectation Using A Multiple-field Non-linear Approximation

The multiple-field ion source used for these experiments represents an approximation of a truly non-linear field design. This design is utilized because it is simple to construct and allows suitable flexibility necessary for initial evaluation. The assumption is made that using multiple linear field segments will not significantly alter the required ideal non-linear potential profile, and that the overall performance will not be significantly diminished as a result. This assumption is based on the premise that the linear field segments are relatively short in comparison with the axial ion source length and thus impose only minimal deviation. A comparison of the ideal and actual potential profiles is shown in Figure 4-16. The ideal profile was generated using the TOFSORC3 program with 0.0001-cm increments over the 2.499-cm ionization region length. The voltage profile used in the evaluation was calculated with the NONLINEAR program using the ionization region electrode spacing dimensions of between 0.124 and 0.303 cm, as described previously. As shown, the potentials in both cases are virtually identical. More revealing however, is the comparison of electric field gradients, also shown in Figure 4-16. The electric field profile present in the experimental design is a step-function with the step boundaries occurring at the ion source electrode positions. The difference between the ideal and actual electric fields is most pronounced over the first ionization region, and it is here that the greatest experimental deviation resulting from a non-ideal electric field may be expected.
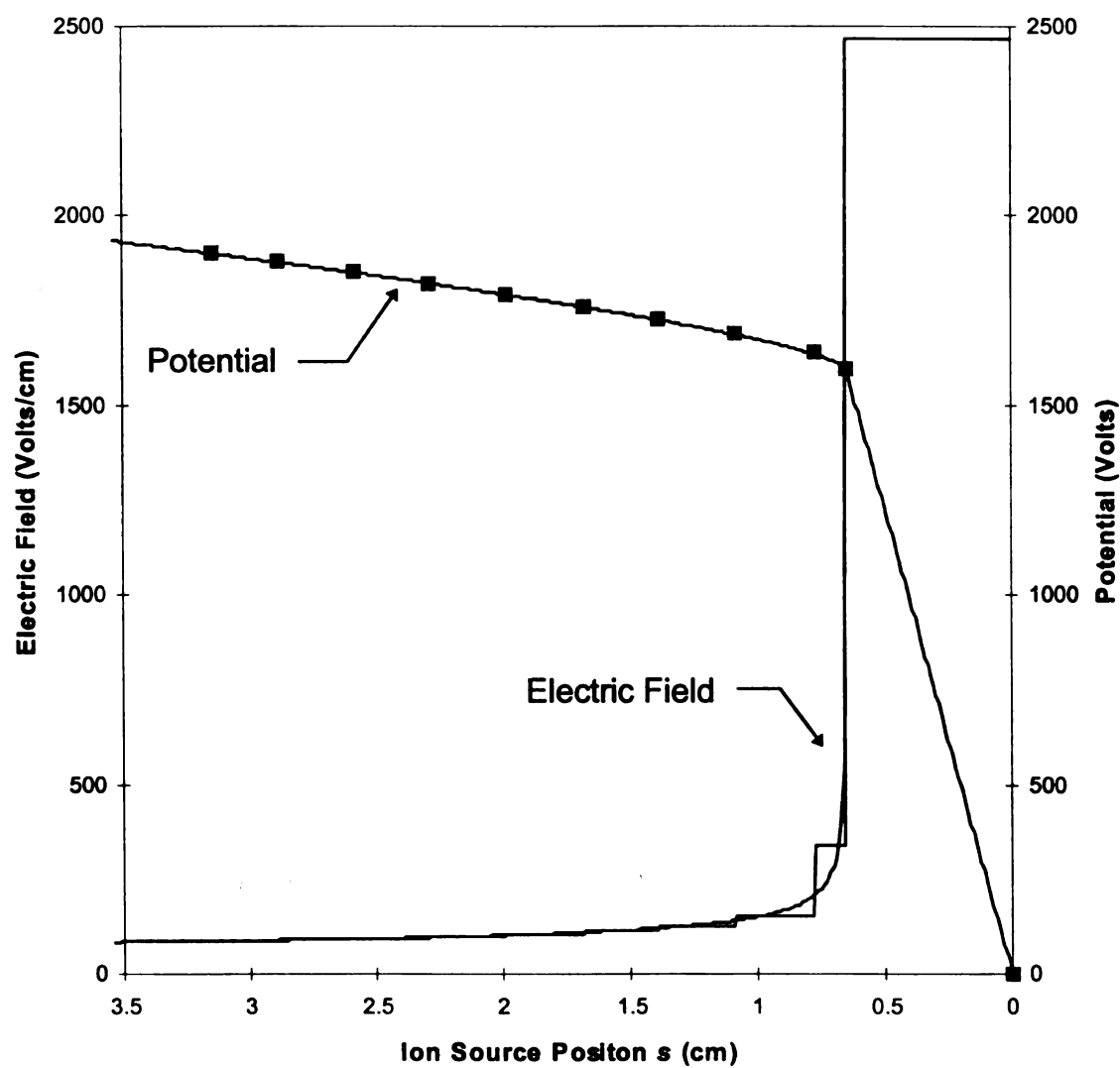
Figure 4-16. Comparison of ideal and actual potentials applied to ion source configuration, and electric fields generated in both cases.

The effect of ionization position offset can also be examined by evaluating the temporal deviation expected for ions beginning at non-ideal locations along the ionization region axis, as plotted in Figure 4-17. While the non-linear ion source configuration yields equal flight times for ions beginning at nine discrete locations within the ionization region, there is a distribution of ion flight times for ions beginning from other axial locations. The pattern of temporal flight-time distributions for ions originating across each inter-electrode space is similar to that observed using the linear two-field ion source. In this case however, the magnitude of the temporal distribution is reduced as a consequence of the electrode spacing being short in comparison with the overall ionization region length. The most significant temporal distribution occurs at the first ionization space where the ideal electric field has the greatest rate of change.

Performance Using Calculated Design

The voltage profile used in the non-linear ion source configuration was designed to provide an average ion arrival time similar to that obtained using the linear electric field configuration. The physical dimensions described above were entered into the Mathcad program NONLINEAR which calculated the necessary voltage for each electrode, listed in Table 4-3. These voltages were then set on the voltage divider as measured, using a handheld digital voltage meter.

A plot of the theoretically predicted and experimentally determined arrival time distributions using the calculated required voltages is shown in Figure 4-18. Ideally, there should be no deviation in ion arrival time due to initial ion location if the electric fields have been properly selected. The experimental data show an ion arrival time range of
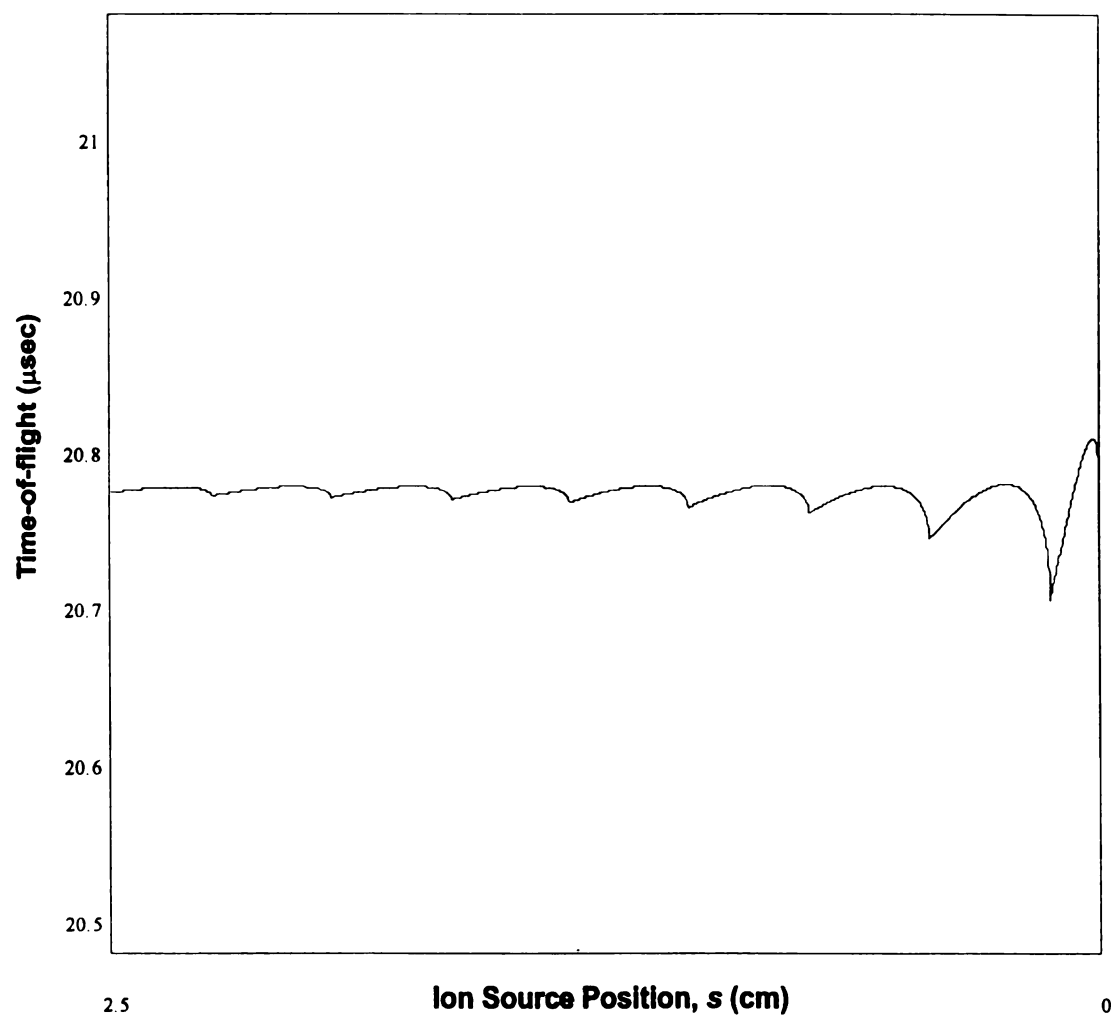
Figure 4-17. Calculated ion arrival-time distribution for the multi-gridded ion source, beginning at the ionization/acceleration region boundary.
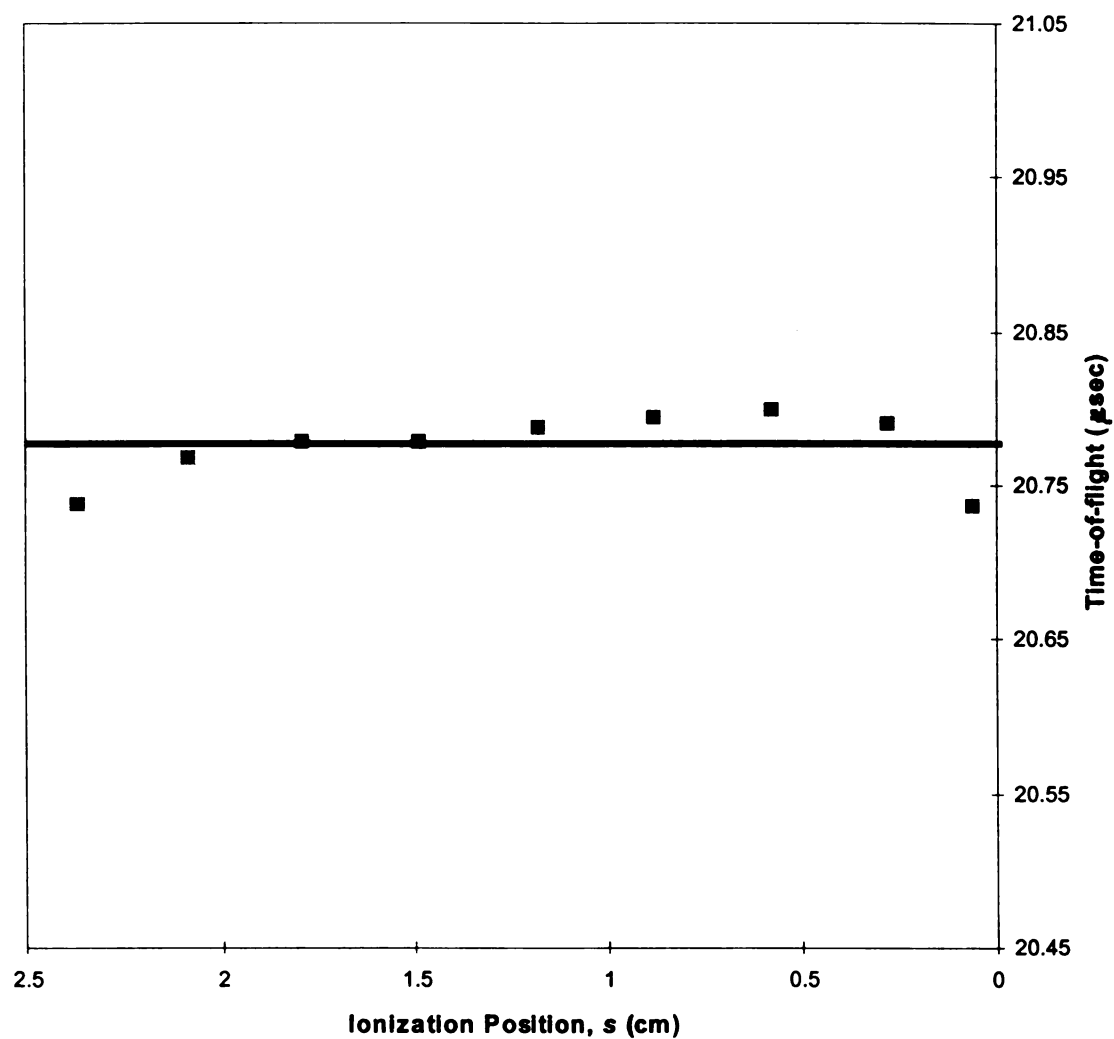
Figure 4-18. Theoretically predicted and experimentally determined ion arrival times for m/z 56 ions originating in each ion source position. D=153 cm, d=0.648 cm.

only 63 nsec, which is a 3.6× improvement in variance over the best case observed using

linear electric fields. Furthermore, if the end points are discarded, the flight time variance

is reduced to 32 nsec, which is a >7× temporal improvement. This data set alone appears

to validate the expectation of the non-linear acceleration proposal.

	Calculated Values	Corrected Values	
Electrode	Potential (V)	Potential (V)	Difference (V)
0	1600	1600	0
1	1641	1642	1
2	1689	1699	10
3	1727	1730	3
4	1762	1764	2
5	1794	1796	2
6	1824	1824	0
7	1852	1854	2
8	1880	1879	-1
9	1903	1901	-2

Table 4-3. Calculated and experimentally derived voltages and electric field values applied to ion source electrodes configured in non-linear acceleration mode.

Performance Using Empirical Voltages

In order to improve the performance of the non-linear acceleration ion source, the

voltages supplying each electrode were adjusted using the potentiometers located on the

voltage divider. Beginning with ionization region position 2, the voltages of electrodes

2-9 were individually adjusted to set the ion arrival time from each ionization region to be

20.764 μs. The experimentally determined optimal voltages are listed in Table 4-3.

The difference between these sets of voltages ranges from –2 to +10 V. The predicted ion arrival times and the measured arrival times using the empirical voltages is illustrated in Figure 4-19, and a plot of the ion arrival time distributions at each ionization position is shown in Figure 4-21Figure 4-21. There are several possible causes for the minor discrepancies between the experimental and calculated voltages. The 10 V difference observed for electrode 2 is partially a consequence of the performance from ionization position 1, which consistently yielded arrival times lower than those resulting from the other ionization positions. This discrepancy could not be corrected, and limitations of the voltage divider precluded the possibility of providing to the other electrodes voltages that would yield identical ion arrival times to that of ionization position 1. Thus, the voltage on electrode 2 was altered to ensure that the arrival time associated with ionization position 2 could duplicated throughout the rest of the ionization region. A second contributor to the voltage discrepancies is that physical distortion in the electrodes or grid material may have altered their axial location. A displacement of only 2 mm corresponds to an ~2.5 V deviation in expected voltage, which is within the voltage error observed. Visual observation of the ion source after conducting the experiments revealed slight imperfections of approximately 1 mm in the grid material on several electrodes. Overall, the difference between the expected and required voltages necessary to achieve complete space focusing are relatively insignificant. Complete space focusing can be readily achieved using an ion source designed to provide non-linear ion acceleration. The fact that minor adjustments can be made that compensate for electrical or mechanical imperfections also has practical significance to the possibility of constructing mass spectrometers implementing non-linear ion acceleration.
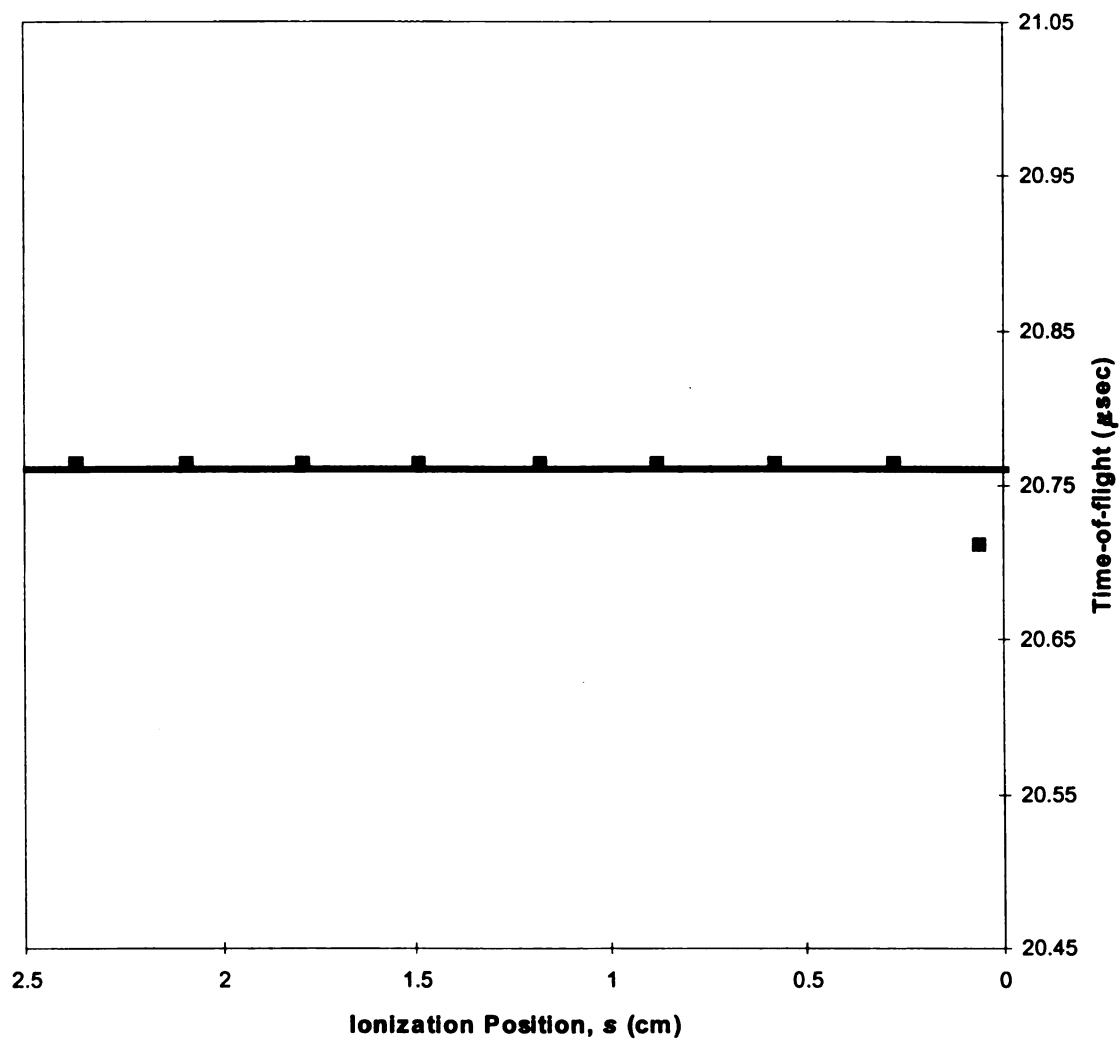
Figure 4-19. Theoretically predicted and experimentally determined ion arrival times for m/z 56 ions originating in each ion source position. D=153 cm, d=0.648 cm.
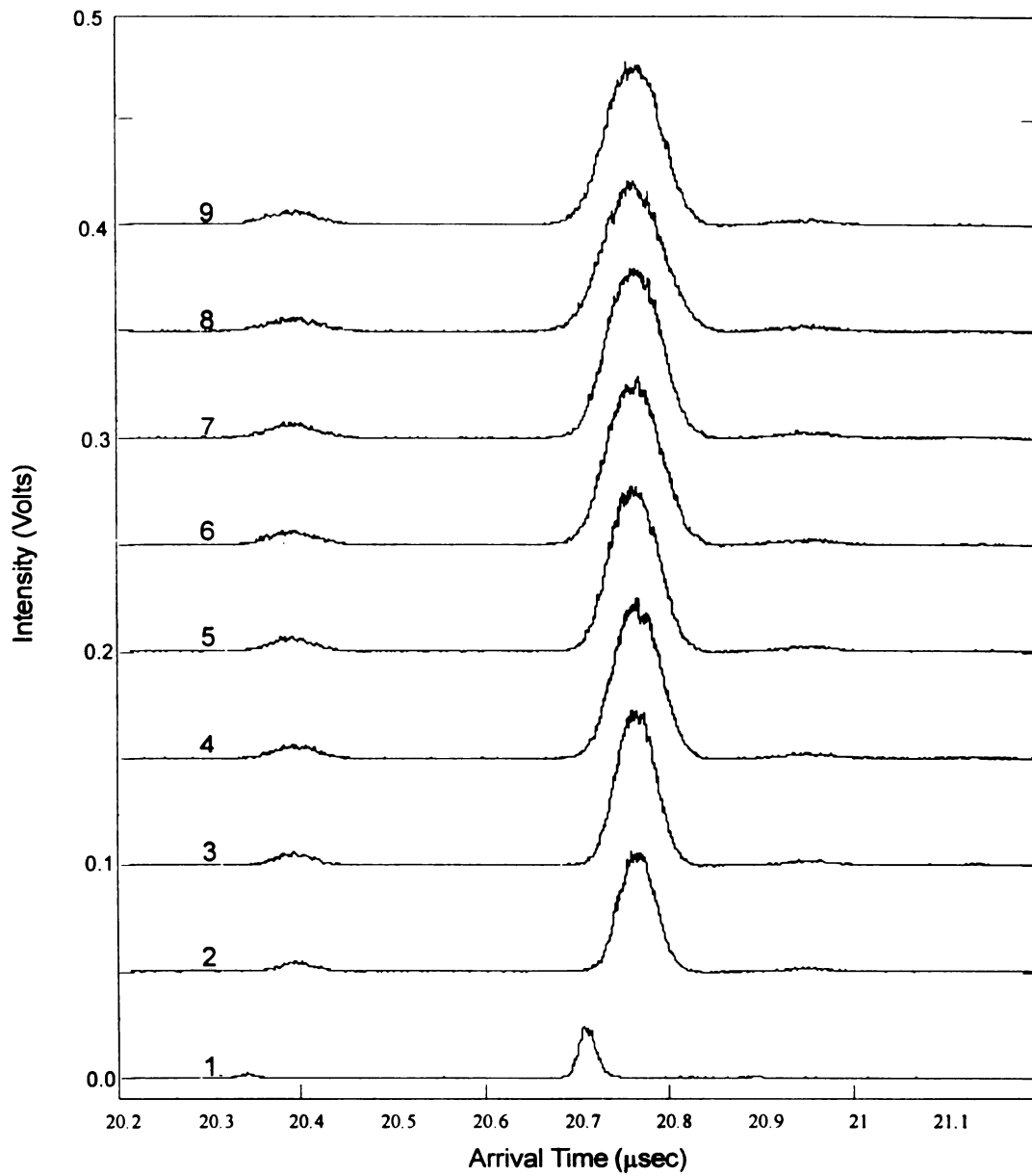
Figure 4-20. Arrival time distributions for ions originating at the various ion source ionization positions, where the ion source voltages were empirically adjusted to provide optimal performance.

Effect of Deliberate Perturbation

The non-linear ion source configuration was further evaluated by adjusting the voltage of a single electrode within the ionization region in order to alter the electric fields within the source and consequently, the time-of-flight for those ions traversing the altered electric fields. The experiment was conducted by altering the voltage on electrode 6 by +3 V in one case and −3 V in a second case, and measuring the change in flight time for ions beginning in ionization regions 6–9. The effect of the perturbation on ion arrival time is plotted in Figure 4-21 as ion arrival time versus ionization position and is compared with the theoretically predicted ideal arrival time distribution as well as the predicted arrival time distribution using the perturbed electric fields. The close agreement between the theoretically predicted non-ideal behavior and the experimentally obtained data is further evidence supporting the hypothesis of non-linear acceleration. Furthermore, the minimal difference between the ion arrival times for the non-ideal and ideal configurations suggests that the non-linear arrangement is relatively insensitive to voltage fluctuations, minimizing the need for power supply voltage stability.
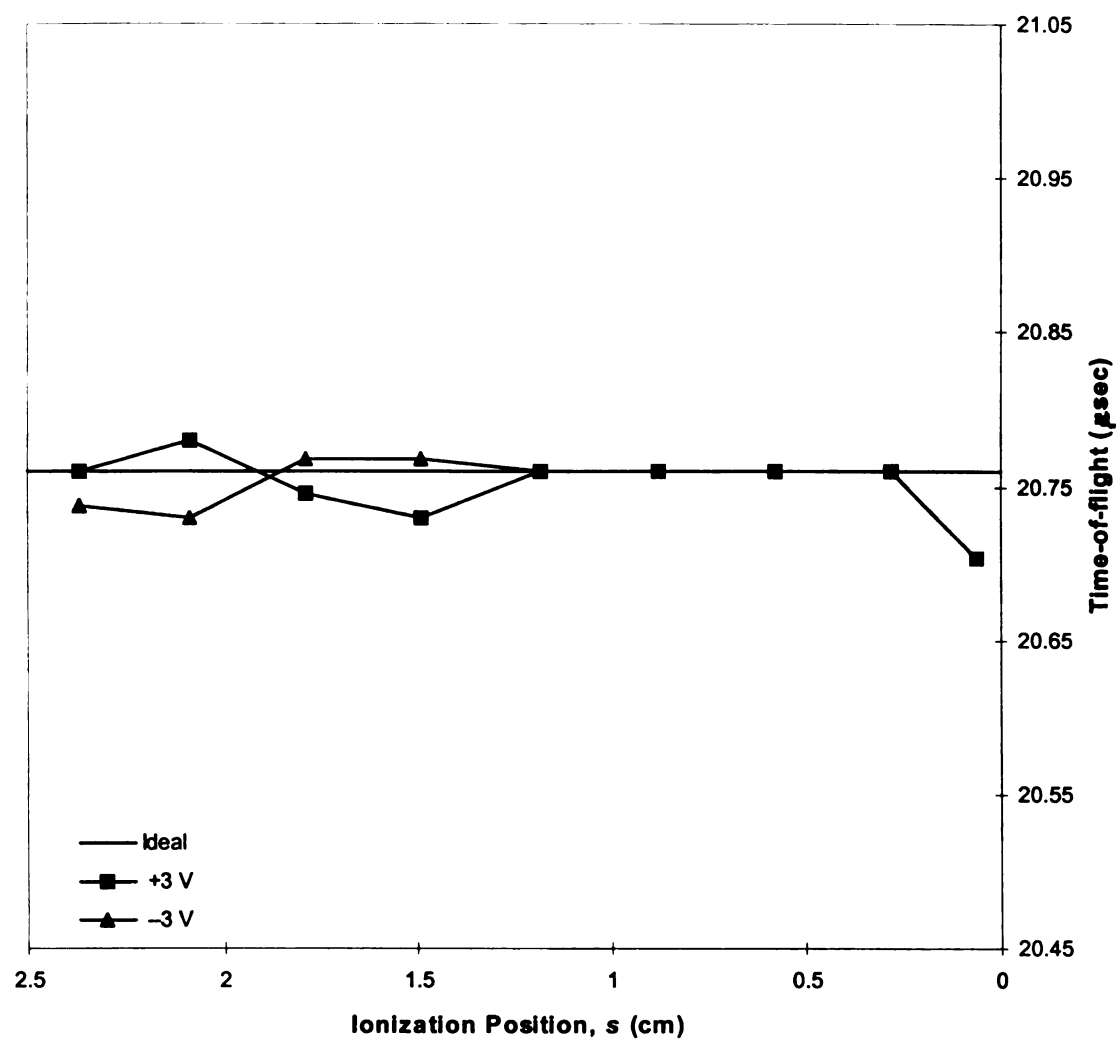
Figure 4-21. Effect of two ±3 V perturbations to electrode 6 on time-of-flight for ions originating from ionization positions 6–9.

Attempts at Evaluating A Grid-free Non-linear Configuration

While the multi-gridded ion source provides strong evidence supporting the requirement of non-linear acceleration for complete space focusing, the series of linear electric fields created within the ion source only approximate a truly non-linear potential gradient. An ideal non-linear ion source configuration requires that the potential profile and the electric field within the ionization region vary smoothly as a function of axial location, and the only way to achieve this configuration is with a grid-free, open ion source geometry.

In an attempt to evaluate such a configuration, the ion source described above was modified by removing the grid material attached to ionization region electrodes 1–8. The electrodes spanning the acceleration region remained gridded as before. The non-linear electric field required for this configuration was determined using the TOFSORC3 program, where the linear field segments calculated by the program were 0.0001 cm in length; significantly small in relation to the overall ion source axial geometry.

The elimination of the electrode grids poses a severe constraint to achieving the appropriate electric field potential profile due to the non-homogeneous nature of the desired non-linear field. The manifestation of this non-homogeneous nature is illustrated in Figure 4-22. Here, the electric field profile, represented in a topographical format as equipotential contour lines, is plotted over a cross-sectional outline of the ion source. This profile was generated using the Simion[19] ion optical modeling program, which calculates electric field gradients and models predicted ion trajectories in a given electrode geometry. The voltages applied to the ionization region electrodes in the Simion optical model were those predicted by the TOFSORC3 program. As shown in the figure,
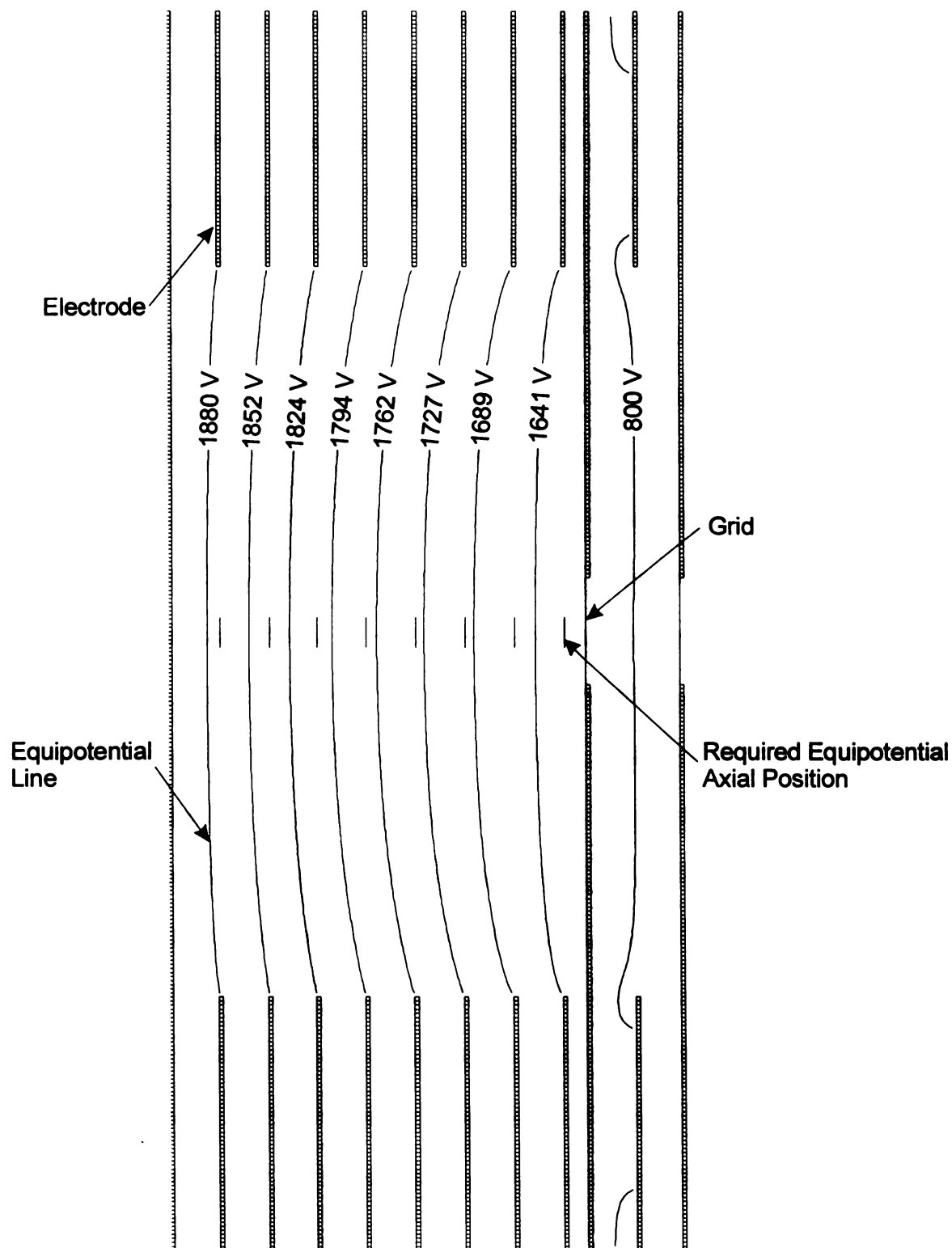
Figure 4-22. Equipotential surface plot of electrode voltages applied to the grid-free ion source. Each equipotential surface exhibits cylindrical axial symmetry, and each is located farther back along the optical axis than desired.

the equipotential electric field lines corresponding to the electrode voltages are not strictly orthogonal to the ion source axis, and exhibit a curvature where the axial location of the applied potential is located farther from the ion source exit than required, and the potential at the axial position corresponding to the electrode coordinate is lower than expected.

In order to achieve the required non-linear potential profile along the longitudinal axis of the ion source, the voltages applied to the ionization region electrodes must be significantly different from the predicted voltages in order to compensate for the electric field inhomogeneity and redistribute the potential gradient along the optical axis. A graph of the ionization electrode voltage profile required for the instrumental conditions used in these experiments is plotted in Figure 4-23. As shown, the difference between the required applied electrode voltage and that required along the optical axis is the greatest at the position corresponding to electrode 1, where the applied potential of 3940 V is over two times greater than that of the desired axial potential. This condition places an electric field strength of ~20kV/cm between electrode 1 and electrode 0 (held at 1600 V), which is far greater than the insulating capacity of the ion source can withstand. Consequently, every attempt at implementing this grid-free non-linear acceleration configuration, even under conditions where the overall accelerating potential was greatly reduced, resulted in arcing between the electrodes and the formation of electrically conducting traces on the insulating ceramics. For this reason, no successful evaluation of the grid-free design was accomplished using this ion source.
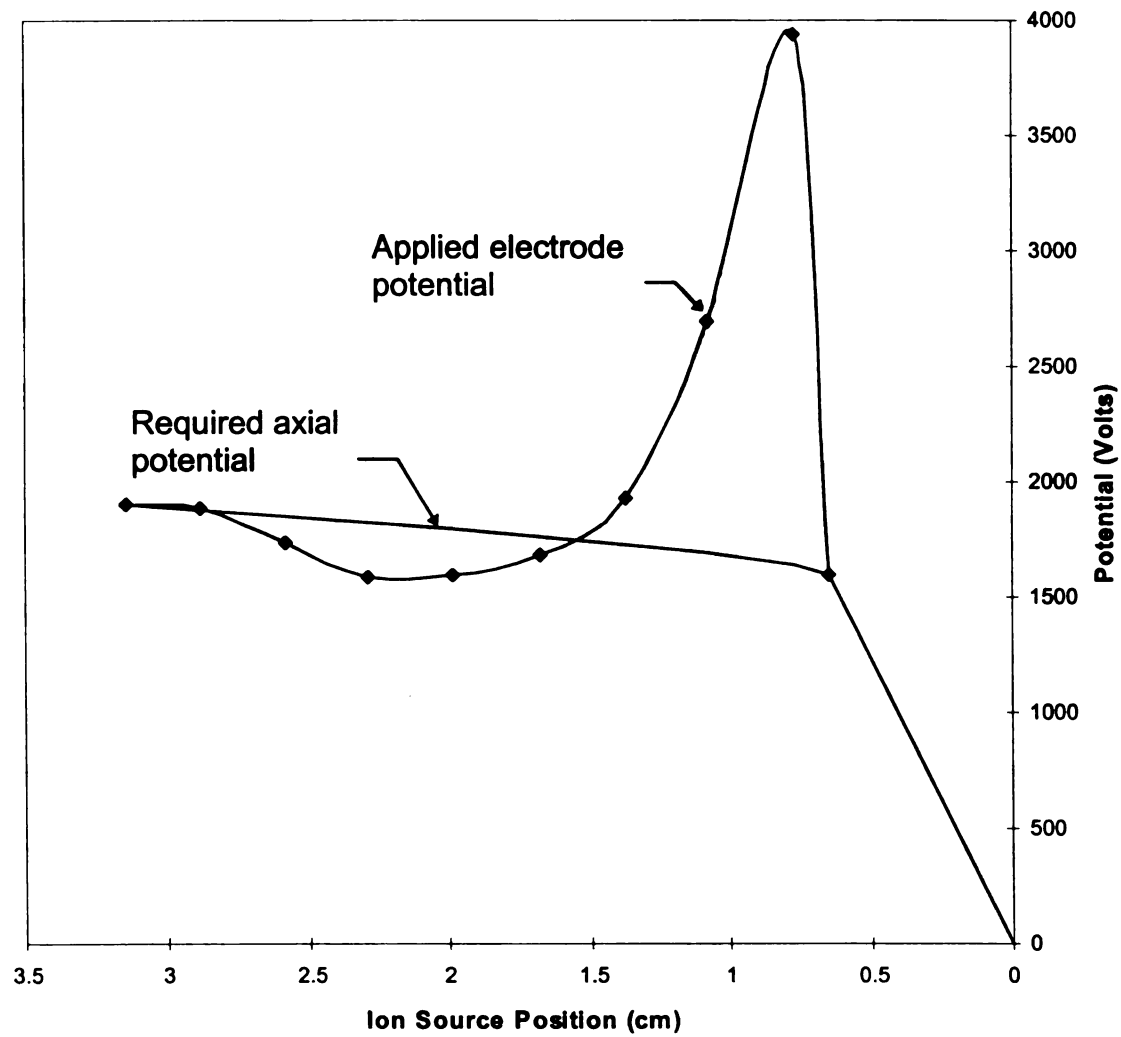
Figure 4-23. Plot of axial potential and the theoretical electrode potentials required to achieve the optimal axial potential profile for the grid-free non-linear ion source configuration. Electrode potentials were determined using the Simion ion optical modeling program.

A second important consideration in the design of a non-linear grid-free ion source relates to the axial profile of the equipotential surfaces. Any deviation of these surfaces from axial orthogonality results in an axially non-parallel ion trajectory, with the consequent axial dispersion of ions within the ion source reducing ion transmission through the ion source and ultimately, significantly reducing the number of ions reaching the detector. A suitable ion source design must minimize this cause of ion dispersion.

A plot of the equipotential surfaces theoretically present with the ion source configured with the electrode potentials illustrated in Figure 4-23 is shown in Figure 4-24. In comparison with the electric field plot illustrated in Figure 4-22, the application of the calculated electrode potentials significantly reduced the difference between the required axial potentials and those present along the various optical axis positions. However, this increased accuracy was accompanied by an increase in curvature of the equipotential surfaces. This condition is most pronounced near electrode 1, where the electric field gradient is the steepest.

In ion source design, there is a tradeoff between equipotential surface curvature and the problem of sustainable electric field gradients described above. If the inner diameter of electrode 1 were reduced, the voltage required to provide the appropriate axial potentials would also have been reduced. In principle, the electrode 1 inner diameter could be reduced to the 0.50" diameter of the ion optical volume, which in this case is determined by the inner diameter of the accelerating region electrodes. However, the result would a significant increase in the equipotential surface curvature and a decrease in ion transmission. Ion trajectory modeling indicated that for the mass spectrometer
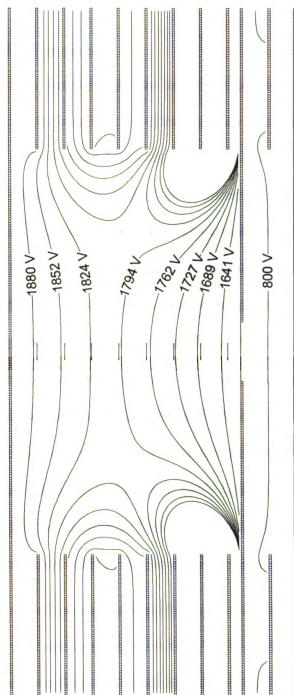
Figure 4-24. Equipotential surface plot of ion source potentials where electrode voltages have been adjusted to achieve a nearly ideal axial potential profile.

configuration used in these experiments, suitable ion transmission could only be achieved using a relatively large ionization region diameter.

Summary and Significance

The dependence of ion time-of-flight on initial ion position when using linear ion acceleration has been documented by experimental data using a two-field ion source model first described by Wiley and McLaren. The experimental results, along with the theoretical analysis, validate their claims that linear fields provide a first-order approximation of space focusing. Theoretical calculations and experimental data also indicate that for static field configurations, the independence of time-of-flight from initial ion position requires the use of a non-linear acceleration field. This may occur either exclusively or in concert with a subsequent linear field, so long as the non-linear field is applied over the region spanning the axial range of initial ion positions. The concomitant use of non-linear and linear fields combines the best features of the completely parabolic non-linear model and the Wiley/McLaren two-field linear model: the non-linear field provides complete space focusing, and the two fields allow the space focus plane to be located beyond the end of the ion source. This flexibility cannot be achieved using either strictly non-linear accelerating fields or two linear fields alone.

While the achievement of a completely non-linear potential profile is problematic, it is possible to achieve an adequate approximation of a non-linear field using a series of short linear fields, so long as those fields are relatively close in relation to the overall axial ion source dimension. When compared with the two-field linear configuration, the data show that this ion source provides a significant improvement to space focusing across the entire ionization region with a slight temporal distortion near the ion source exit where the

electric field gradient is the steepest. In normal operation this region is not utilized for ion generation or capture, and this distortion will be of little or no consequence in the exploitation of non-linear acceleration schemes.

The significance of space focusing using the ion source configuration described in this chapter is illustrated in Figure 4-25. Here, the raw ion abundance information obtained from sampling each ionization position under conditions of linear and non-linear acceleration, displayed previously in Figure 4-14 and Figure 4-20 respectively, is shown summed. The integrated ion arrival time profile obtained using linear acceleration, shown in Figure 4-25a, displays a resolving power of 50, while the profile obtained using non-linear acceleration, shown in Figure 4-25b, displays a greater resolving power of 180. Additionally, there is a concomitant ~3.5x greater signal to background ratio using non-linear acceleration. Thus, for significantly long axial ion extraction volumes, the use of non-linear acceleration yields a significant improvement to resolving power and detectability over linear acceleration configurations. For TOFMS configurations employing energy focusing devices such as the ion mirror in addition to non-linear acceleration, an even greater gain in resolving power would be expected.
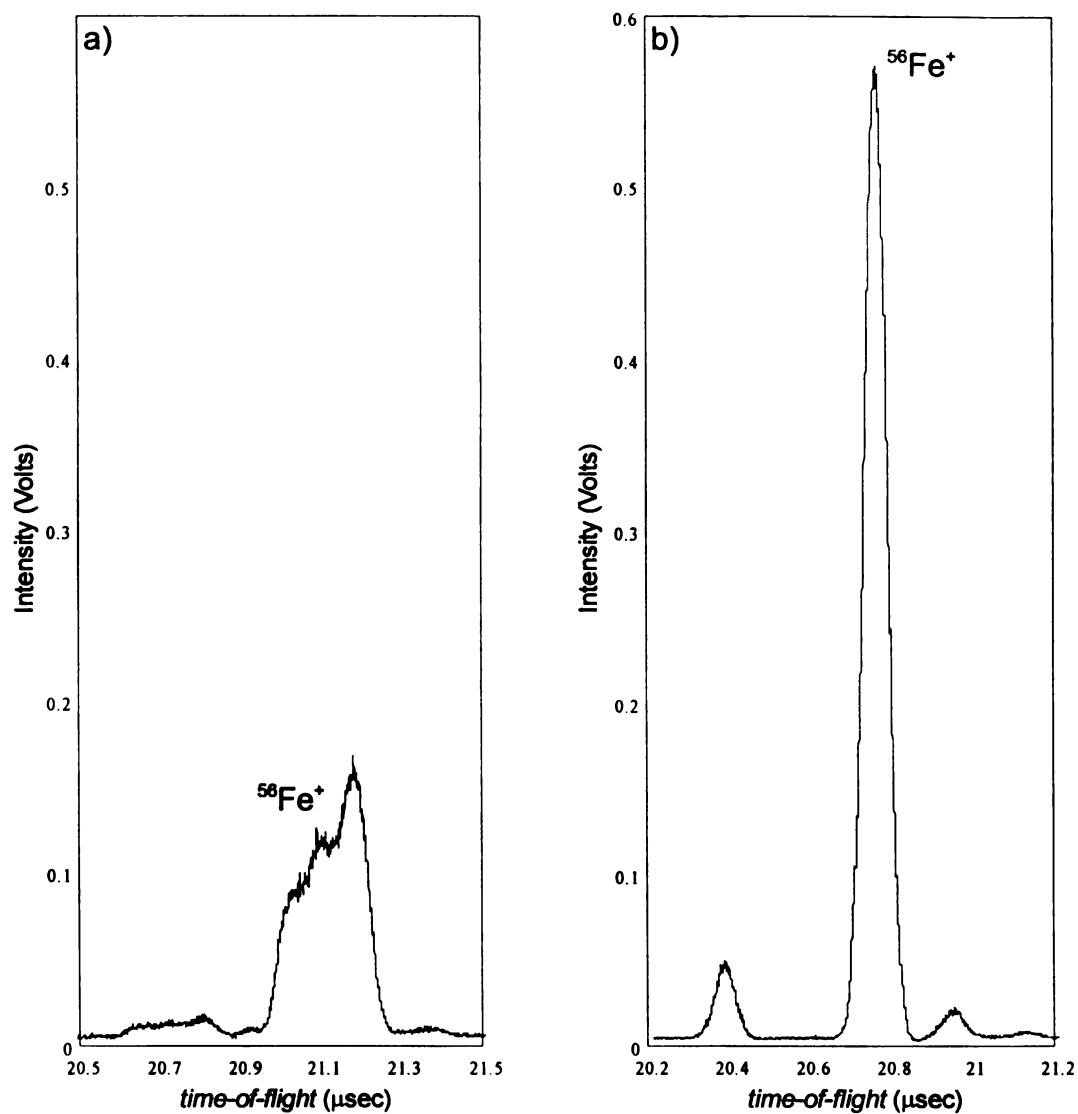
Figure 4-25. Comparison of resolving power obtained using linear (a), and non-linear (b), ion acceleration.

References

1. Wiley, W. C.; McLaren, I. H. *Rev. Sci. Instrum.* **1955**, *26*, 1150.

2. Muga, M. L. *Anal. Instrum.* **1987**, *16*, 31.

3. Yefchak, G. E.; Enke, C. G.; Holland, J. F. *Int. J. Mass Spectrom. Ion Phys.* **1989**, *87*, 313.

4. Kinsel, G. R.; Johnson, M. V. *Int. J. Mass Spectrom. Ion Phys.* **1989**, *91*, 157.

5. Glashchenko, V. P.; Semkin, N. D. *Sov. Phys. Tech. Phys.* **1987**, *32*, 665.

6. Grix, R.; Kutscher, R.; Ki, G.; Grüner, U.; Wollnik, H. *Rapid Comm. Mass Spectrom.* **1988**, *2*, 83.

7. Bandura, D. R.; Makarov, A. A. *Int. J. Mass Spectrom. Ion Phys.* **1993**, *127*, 45.

8. Steadman, J.; Syage, J. A. *Rev. Sci. Instrum.* **1993**, *64*, 3094.

9. Vlasak, P. R.; Beussman, D. J.; Ji, Q.; Enke, C. G. *J. Am. Soc. Mass Spec.* **1996**, *7*, 1002.

10. Flory, C. A.; Taber, R. C.; Yefchak, C. E. *Int. J. Mass Spectrom. Ion Phys.* **1996**, *152*, 177.

11. Stein, R. *Int. J. Mass Spectrom. Ion Phys.* **1974**, *14*, 205.

12. Rockwood, A. L. In *Proc. of 34th ASMS Conf. On Mass Spec. and Allied Topics*, Cincinati, OH, June 8–13, **1986**, 173.

13. Rockwood, A. L.; Udseth, H. R.; Gao, Q.; Smith, R. D. In *Proc. of 42nd ASMS Conf. On Mass Spec. and Allied Topics*, Chicago, IL, May 29–June 3, **1994**, 1038.

14. Hulett, L. D., Jr.; Donohue, D. L.; Lewis, T. A. *Rev. Sci. Instrum.* **1991**, *62*, 2131.

15. Flory, C. A.; Taber, R. C.; Yefchak, C. E. *Int. J. Mass Spectrom. Ion Phys.* **1996**, *152*, 169.

16. Mathsoft, Inc., Cambridge, Massachusetts, 02142.

17. Norwood, K.; Ali, A.; Flesch, G. D.; Ng, C. Y. *J. Am. Chem. Soc.* **1990**, *112*, 7502.

18. Banares, L.; Baumert, T.; Bergt, M.; Kiefer, B.; Gerber, G. *Chem. Phys. Lett.* **1997**, *267*, 141.

19. Idaho National Engineering Laboratory, Idaho Falls, Idaho, 83451.

CHAPTER 5

PROSPECTS FOR FUTURE IMPROVEMENTS TO RESOLVING POWER

For many established and developing GC-MS and LC-MS techniques, the task of coupling the exit end of the chromatographic column to the mass spectrometer represents the most difficult obstacle to the successful implementation of the combined technique. In each case, the emerging analyte greatly expands as it enters the vacuum environment, placing stringent requirements on the pumping required to maintain the vacuum, and complicating any attempt to analyze the entire eluent volume. Time-of-flight ion source configurations requiring an axially narrow initial spatial distribution are thus ultimately limited in their application, and the reduction or elimination of the narrow spatial requirement should yield an increase in applicability and detection efficiency. The use of non-linear ion acceleration stands as a viable solution addressing TOFMS instrumental configurations where the initial spatial distribution represents the primary limitation to achievable resolving power. Furthermore, in instrumental configurations employing capture of previously ionized analytes, as is the case with electrospray and atmospheric pressure ionization, the axial dimension at the moment of ion capture can introduce energetic variations which are amenable to the velocity correcting realized by non-linear field acceleration. Also, the recent popularity of attempts to miniaturize time-of-flight analyzers places added emphasis on space focusing as the ratio of the ion source dimension to the total flight path is often increased, exacerbating the spatial distribution problem.

While the limitations of initial energy spread and turn-around time are not addressed in this work, correcting devices already addressed in the academic literature could be employed to provide additional enhancements to resolving power. It is anticipated that the combination of the dual non-linear/linear ion acceleration along with impulse-field focusing and non-linear ion mirror fields may provide complete correction for each of the fundamental limitations to mass resolving power. For future applications, it is clear that the implementation of non-linear acceleration will extend the ultimate performance of TOFMS instrumentation.

Appendix A

Rapid Analysis of Volatile Flavor Compounds in Apple Fruit Using SPME and GC/Time-of-Flight Mass Spectrometry

Jun Song,[†] Ben D. Gardner,[‡] John F. Holland,[§] and Randolph M. Beaudry*,[†]

Department of Horticulture, Department of Chemistry, and Department of Biochemistry,
Michigan State University, East Lansing, Michigan 48824

Solid-phase microextraction (SPME), time-compressed chromatography (TCC), and time-of-flight mass spectrometry (TOFMS) were examined for their suitability and compatibility for rapid sampling, separation, and detection of apple flavor volatiles. Flavor-contributing volatile compounds were found to have relatively high partition coefficients on a 100 μm thick coating of polydimethylsiloxane (PDMS) on a SPME fiber. The time required to saturate the PDMS coating was highly volatile-dependent, varying from less than 2 min to greater than 30 min. However, the response of this system was linear in the ppb to ppm range when the adsorption duration was standardized. The speed of the TOF mass spectrometer permitted identification and quantification of compounds having chromatographic peak widths of only a fraction of a second. The unskewed nature of fragmentation patterns obtained allowed individual component spectral characterization of unknown compounds even when not fully chromatographically separated. Thus, the time required for chromatography could be reduced by an order of magnitude without loss in analytical performance. Typical analysis times for complex mixtures were 2–5 min as compared with 20–60 min required for standard purge-and-trap analyses.

INTRODUCTION

Aroma is one of the most important quality criteria of fruit and vegetable products, and a considerable amount of research has been devoted to developing analytical techniques for characterizing aroma-producing compounds. Both qualitative and quantitative information is desired in order to monitor produce flavor quality and ripeness and to provide quality control for fresh and processed products. Progress in aroma research is impeded, however, by slow sampling, separation, and detection methodologies. Fruit aroma research is subject to a number of constraints that make more rapid analysis desirable. The seasonal nature of fruit harvest and production requires that new protocols be worked out quickly and efficiently in order to meet research 'time windows' established by the commodity. Typical horticultural and biochemical research requires multiple experimental treatments as part of a statistically relevant design, so sample numbers for most experiments are relatively large (tens to hundreds), and often an entire study must be completed in a limited time. In fruit aroma biosynthesis studies, especially those evaluating the response to metabolic precursor feeding, aroma production is dynamic with short (minute) and long-term (hour) temporal components. As a result, sampling must be repetitive and span a wide range of time intervals. Furthermore, an analytical system should be sufficiently flexible to work with both flow-through and static systems having a broad range of components. Volatile aroma compounds are typically analyzed using either direct headspace (Neubeller and

Buchloh, 1978) or dynamic headspace purge-and-trap methods (Streif, 1981; Werkhoff and Bretschneider, 1987). While direct headspace analysis is largely confined to higher concentration samples, purge-and-trap sampling can enhance sensitivity by enriching volatile components on a polymer bed. The dynamic headspace purge-and-trap method has been thoroughly standardized by Buttery et al. (1989), Mattheis et al. (1991), and Song and Bangerth (1993) for routine analysis of tomato and apple fruit volatiles. However, this technique is expensive, time-consuming, and prone to methodological difficulties. During analysis, the sample preparation step for purge-and-trap analyses is frequently the most time-consuming and labor intensive step. It is also the primary point of analyte loss from the matrix.

An alternate sampling methodology, solid-phase microextraction (SPME), has the potential to reduce the time investment in sampling and should work well in combination with rapid separation and detection systems. SPME has been applied to the analysis of volatile and nonvolatile compounds (Arthur and Pawliszyn, 1990) in gaseous and liquid samples and to analyze flavor in fruit juice beverages, in vegetable oils (Yang and Peppard, 1994), and in orange juice (Steffen and Pawliszyn, 1996). SPME has been shown to be a simple and effective sampling method providing a linear response to concentrations covering four orders of magnitude (Arthur et al., 1992; Louch et al., 1992). It is also rapid, providing complete extraction and transfer of volatile organic compounds in under five min (Gardner et al., 1995).

The recent development of a gas chromatographic detector utilizing TOFMS with time array detection (TAD) has the analysis speed needed to take advantage of the rapidity of SPME sampling technology. This instrument system additionally enables the use of time-compressed chromatography (TCC) whereby temporally unresolved components can be characterized by their

* Author to whom correspondence should be addressed.
† Department of Horticulture.
‡ Department of Chemistry.
§ Department of Biochemistry.

unique mass spectra. TCC permits a significant reduction in the time invested in separation. To date, SPME in conjunction with TCC and TOFMS for analysis of flavor volatiles in horticultural produce has not been evaluated. In this paper, we report on SPME sampling characteristics (speed, variability, linearity, saturation kinetics, and matrix effects) in combination with rapid GC techniques (short, narrow bore columns, high linear flow rates, and high temperature ramp rate) and a TOF mass spectrometer for detection as a system for rapid and quantitative analysis of aroma volatiles in apples.

EXPERIMENTAL PROCEDURES

Volatile Aroma Standards Preparation. Volatile aroma compounds were purchased from Sigma Co. and Fluka Chemical Corp. Standard mixtures were prepared with 0.3–1.0 μL of butyl acetate, ethyl 2-methyl butanoate, hexyl acetate, 1-butanol, 1-hexanol, and 6-methyl-5-hepten-2-one in specially-built gas-tight 4.4-L glass volumetric flasks fitted with a tapered ground glass stopper containing a gas-tight Mininert valve (Alltech Assoc., Inc., Deerfield, IL). The mixed standards sample was applied to a small paper filter disk in the neck of the flask and dropped to the flask bottom. The flask was sealed, and the liquid material was allowed to vaporize to provide known headspace concentrations ranging from 5 to 10 μL L⁻¹.

Sampling. SPME Procedure. A SPME (Supelco Co., Bellefonte, PA) fiber coated with polydimethylsiloxane (PDMS, 1 cm long, 100 μm thickness) was used to collect and concentrate volatiles by virtue of its sorption characteristics (Arthur and Pawliszyn, 1990). The SPME device consisted of a retractable fiber enclosed in a sheath. During sampling, after entering the sample container, the fiber was extended, exposing the sorption surface. The fiber was then retracted prior to removal from the sample container. The fiber was preconditioned at 250 °C for 1–2 h. Various sample exposure times were used for adsorption, and the volatiles were desorbed from the fiber for 90 s at 250 °C into the glass-lined, splitless injector port of a GC (HP-6890, Hewlett Packard Co.). All SPME samplings were carried out at 23 °C in triplicate unless otherwise noted.

SPME Saturation Kinetics. SPME fibers were exposed to the headspace of 4.4-L flasks containing a mixture of butyl acetate and hexyl acetate at a concentration of approximately 5 μL L⁻¹. Fibers were held in the atmosphere of the flask for specific lengths of time ranging from 5 to 480 s. Analyses were carried out using a GC with a flame ionization detector (FID).

To determine saturation kinetics in complex mixtures of volatiles, apple fruit (*Malus domestica* Borkh. cv. Golden Delicious) stored for 2–3 months at 0 °C were warmed to room temperature (23 °C). Intact apple fruit (300–450 g) were placed in a 3-L flask with purified air passing through at a flow rate of 25–30 mL min⁻¹. Sampling of volatile compounds was accomplished by placing the SPME fiber into a glass tee, fitted with a Teflon-lined halfhole septum (Alltech Assoc. Inc., Deerfield, IL) located at the outlet of the flask. All the connecting gas lines were composed of Teflon.

Apple fruit volatiles reached steady-state concentration in the flask within 4–6 h, after which time SPME fibers were exposed to the volatiles emanating from the flask for varying lengths of time up to 24 min. Response determinations were made three times for each exposure period. While numerous volatiles were tracked, data are reported for butyl acetate, butanol, hexyl acetate, hexyl 2-methyl butanoate and α-farnesene, as these compounds appeared to exhibit the full range of responses detected.

SPME Response Linearity. A gas mixture containing butyl acetate, ethyl 2-methyl butanoate, and hexyl acetate was prepared for the standards described above. A stream of volatiles-free nitrogen gas (1–2 mL L⁻¹) was passed through the flask to dilute the volatiles and to generate a wide range of volatile concentrations. The flask was periodically sealed, and the concentration of the volatiles in the flask was determined by comparison to the gas standards described previously. A 100-μL gas sample was removed by using a gas-

tight syringe (Hamilton No. 1810 with stainless steel needle) and directly injected to a gas chromatograph (Carle AGC Series 400) equipped with a FID, which was used to measure volatile vapor concentrations. The GC was equipped with a packed column (10% DEGS-PS, 80/100 mesh Supelcoport, 3.3 m long, 3 mm id.) and was maintained at 140 °C. Helium was used as the carrier gas at a flow rate of 20 mL min⁻¹. Some volatiles, such as hexyl acetate and 6-methyl-5-hepten-2-one, were found to adsorb to the steel needle (data not shown), and care had to be taken in optimizing the sampling procedure. Pumping the syringe plunger 15–20 times (which apparently saturated the adsorption sites inside the needle) gave a consistent GC response, such that the standard's response had a coefficient of variation of only 2–5%. By this means, any effect of needle adsorption was removed from GC response.

After establishing the gas concentrations in the dilution flask, the TOFMS response was determined using the SPME fiber with a 6-min sampling time (see below). TOFMS response was correlated with volatile concentration.

SPME Partition Coefficient. The partition coefficient (K) of the SPME fiber coating was determined for standard mixtures (5–10 μL L⁻¹) of butyl acetate, ethyl 2-methyl butanoate, hexyl acetate, butanol, hexanol, and 6-methyl-5-hepten-2-one. The SPME fiber was exposed to the volatiles for sufficient time (6–8 min) to allow the coating to reach equilibrium with the flask headspace. K was determined using the following equation (Zhang and Pawliszyn, 1993):

$$K = (A_F V_G)/(A_G V_F)$$

where A_F and A_G are, respectively, the peak areas from the GC response to the fiber coating and direct gas injection, V_F is the volume of the coating (calculated to be 8×10^{-4} cm³), and V_G is the volume of the gas injected (100 μL). Five measurements of K were made per volatile.

Purge-and-Trap Procedure. Purge-and-trap analysis was performed for comparison to the SPME technique. Tenax TA (100 mg, 60/80 mesh, Alltech) was placed in glass tubes (5 cm long, 4 mm id.) with glass wool plugs at both ends of the Tenax. Apple aroma volatiles were collected by inserting a Tenax glass tube into the gas outlet of the above-mentioned sample jars containing apple fruit. Volatiles were adsorbed onto the Tenax for 10 min at a flow rate of 100 mL min⁻¹. The tubes were desorbed using a specially-built desorption unit heated to 250 °C for 10 min while being purged with ultra purified helium (99.999%) at a flow rate of 35 mL min⁻¹. A short 0.2 m long × 0.53 mm id. deactivated fused silica precolumn was attached to the injection port of a Varian 3400 (Varian Analytical). A specially-built cryofocusing unit was used to cool the precolumn to less than −100 °C during the heat desorption process. After cryofocusing, the aroma compounds were then volatilized by heating the cryofocusing unit to 150 °C in a few seconds.

Separation and Detection. *SPME/GC/TOFMS of Apple Volatiles.* Adsorbed volatiles were desorbed from the fiber into the HP-6890 GC as described previously. Volatiles were separated using a capillary column (HP-5, 5 m × 0.1 mm id., 0.34 μm coating thickness). The carrier gas was ultra purified helium (99.999%) at a flow rate of 0.5 mL min⁻¹. The temperature program was isothermal for 1.5 min at 40 °C and then raised at the rate of 50 °C min⁻¹ to 250 °C, and held for 2 min. The GC/MS transfer line temperature was 220 °C. Volatile detection was performed by TOFMS using electron impact ionization (FCD-650, LECO Corp., St. Joseph, MI). Mass spectra were collected at a rate of 40 spectra/s over a range of m/z 40–300. The ionization energy was 70 eV.

Data were analyzed using LECO deconvolution software. Identification of volatile components was confirmed by comparison of collected mass spectra with those of authenticated standards and spectra in the National Institute for Standards and Technology (NIST) mass spectral library, Search Version 1.1.

Purge-and-Trap/GC of Apple Volatiles. Volatiles were desorbed from the Tenax as described above and separated using a capillary column (HP-5, 45 m long × 0.25 mm id., 0.25 μm thick coating). The temperature program was isothermal
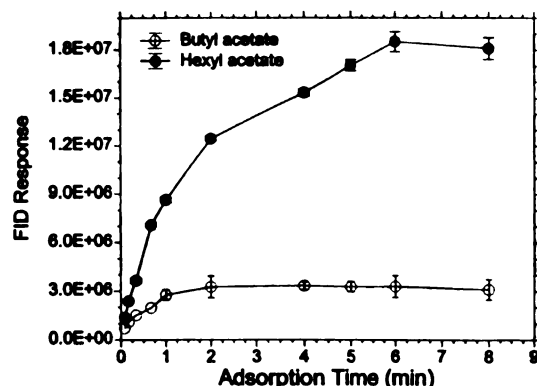
Figure 1. GC/FID response for a mixture of butyl acetate and hexyl acetate as affected by adsorption time on a SPME fiber.
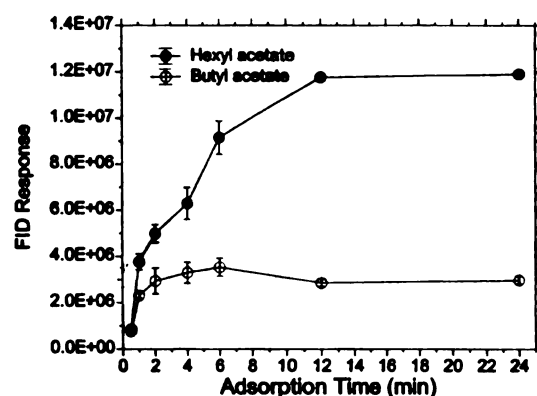
Figure 2. GC/FID response for butyl acetate and hexyl acetate in a complex mixture of apple volatiles as affected by adsorption time on a SPME fiber.

for 5 min at 40 °C and then raised 8 °C min⁻¹ to 250 °C and held for 15 min. Detection was by FID at 300 °C.

RESULTS

Sampling. SPME Saturation Kinetics. The equilibration times for butyl acetate and hexyl acetate standards using the PDMS coating were approximately 2 and 6 min, respectively (Figure 1). The times required for butyl and hexyl acetate to reach equilibrium when in a complex mixture from ripe apple fruit were approximately 4 and 12 min, respectively (Figure 2). Other compounds in the mixture having rapid adsorption kinetics included 2-methylbutyl acetate and 1-butanol (Figure 3). However, hexyl 2-methyl butanoate and α-farnesene did not reach equilibrium in 24 min (Figure 4). The GC response as shown in Figure 3 for 2-methylbutyl acetate in the complex mixture declined as the adsorption time increased beyond 12 min. The nearly linearly increasing response for most compounds appeared to be in the first 1—4 min.

SPME Response Linearity. The response of SPME fiber to volatile concentration was linear for the three compounds tested after 6-min adsorption (Figure 5). For TOFMS detection at 10× background noise, the concentrations of butyl acetate, ethyl 2-methyl butanoate, and hexyl acetate extrapolated to 0.008, 0.0012, and 0.004 μL L⁻¹, respectively.

SPME Partition Coefficients. The PDMS coating/air partition coefficients of SPME fibers for tested aroma impact apple volatiles ranged 33-fold from 1-butanol
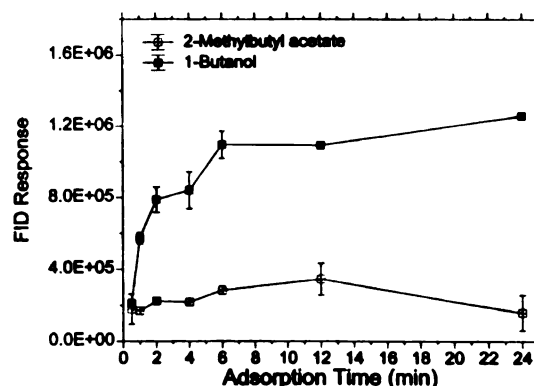
Figure 3. GC/FID response of 2-methylbutyl acetate and butanol in a complex mixture of apple volatiles as affected by adsorption time on a SPME fiber.
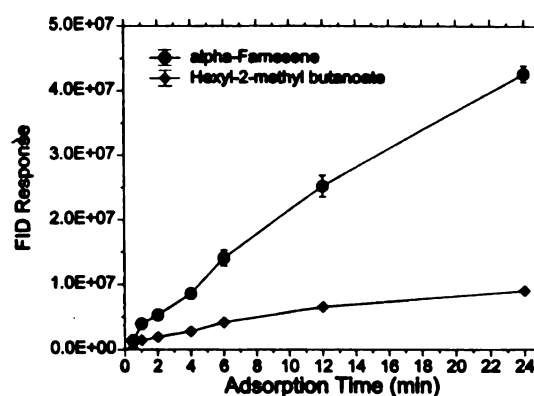
Figure 4. GC/FID response of α-farnesene and hexyl 2-methylbutanoate in a complex mixture of apple volatiles as affected by adsorption time on a SPME fiber.
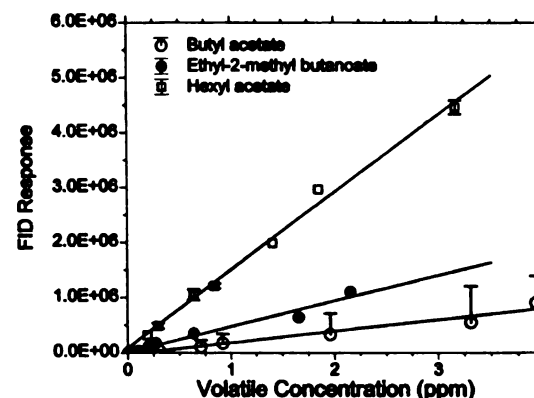
Figure 5. Effect of volatile headspace concentration on the linearity of GC/FID response for butyl acetate, ethyl 2-methylbutanoate, and hexyl acetate adsorbed onto a SPME fiber for 6 min at 23 °C.

with 1.7 × 10⁴ to 6-methyl-5-hepeten-2-one with 5.6 × 10⁵ (Table 1). The dominant influence appears to be the number of carbons in these linear molecules.

SPME Response Variability. With the exception of butyl acetate, the calculated standard errors in these tests resulted in coefficients of variation ranging from 2 to 10%. Butyl acetate varied beyond this range in the linearity tests at concentrations above 3 μL L⁻¹.

Separation. SPME/GC of Apple Volatiles. Using rapid chromatography techniques, apple volatiles con-

Table 1. Experimental Partition Coefficient (log K) Values between Coating and Gas Phase of Some Volatiles in Apples

compound	partition coeff	log K
butyl acetate	2.7×10^4	4.44
ethyl 2-methylbutanoate	3.35×10^5	5.51
hexyl acetate	2.3×10^5	5.36
1-butanol	1.7×10^4	4.21
1-hexanol	2.1×10^5	5.32
6-methyl-5-hepten-2-one	5.65×10^5	5.75

Table 2. Volatile Compounds in Golden Delicious Apple Fruit, Sampled with SPME (PDMS, 100 μm) and Identified by TOFMS

peak	volatile compd	retention time (min) SPME	retention time (min) purge-and-trap
1	pentane	1.082	
2	acetone	1.132	
3	1-butanol	1.322	
4	propyl acetate	1.494	
5	propyl propanoate	1.524	
6	butyl acetate	1.619	13.45
7	ethyl 2-methylbutanoate	1.639	13.80
8	2-methylbutyl acetate	1.753	15.80
9	propyl butanoate	1.802	
10	butyl propyrate	1.932	
11	pentyl acetate	2.005	
12	butyl 2-methylbutanoate	2.105	
13	butyl butanoate	2.164	
14	hexyl acetate	2.396	21.34
15	butyl-2-methylbutanoate	2.437	
16	pentyl butanoate	2.460	
17	hexyl propyrate	2.492	
18	propyl 2-methyl-2-butenoate	2.650	
19	hexyl 2-methylpropyrate	2.855	
20	not identified	2.893	
21	hexyl butanoate	3.183	
22	butyl hexanoate	3.202	
23	4-methoxyallylbenzene	3.223	
24	hexyl 2-methylbutanoate	3.264	32.76
25	2-methylbutyl hexanoate	3.395	
26	hexyl pentanoate	3.633	
27	2-methylpropyl 2-methyl-butanoate	3.754	
28	hexyl hexanoate	4.002	38.82
29	α-farnesene	4.453	41.75

taining 1—15 carbons could be eluted in about 2 min (Table 2, Figure 6a). In all, 29 compounds other than CO₂ were detected and identified in Golden Delicious apple fruit. Using the SPME, dominant volatiles by response were in decreasing order as follows: α-farnesene, hexyl 2-methylbutanoate, hexyl hexanoate, hexyl butanoate, butyl hexanoate, hexyl acetate, and 2-methylbutyl acetate. There was a tendency for the response to increase with larger, more lipophilic and nonpolar compounds. Propyl acetate, butyl acetate, hexyl acetate, ethyl 2-methylbutanoate, 2-methylbutyl acetate, hexyl butanoate, butyl hexanoate, and hexyl hexanoate are dominant volatile compounds in apples (Paillard, 1991). α-Farnesene and 4-methoxyallylbenzene were also identified.

Purge-and-Trap/GC of Apple Volatiles. The chromatography of the purge-and-trap sampled volatiles took in excess of 40 min, which was roughly 10 times longer than for the rapid chromatography techniques used with the SPME device. Five of the compounds separated were identified by comparison of retention times to those of authenticated compounds (Figure 6b).

Detection. *SPME/GC/TOFMS of Apple Volatiles.* Detection and quantification of apple volatiles from a complex matrix via TOFMS using TCC did not require baseline resolution. The rapid spectral acquisition rate

of 40 spectra/s of the TOFMS permitted 40—80 spectra to be collected over the typical 1—2-s peak widths (Figure 7). Co-eluting compounds such as butyl hexanoate and hexyl butanoate differing by at least one m/z could be identified and quantified. For instance, butyl hexanoate and hexyl butanoate were successfully deconvoluted using m/z 117 and m/z 89, respectively, although elution times differed by only 0.2 s. Since TOFMS generates unskewed spectra consisting of true fragmentation relationships, complete spectral characterization is readily accomplished for each analyte. These compounds were quantified using the unique ions found in the full spectra, which were identified either in the NIST library or generated from authenticated standards. The total time invested per analysis for SPME/TCC/TOFMS was approximately 10 min.

Purge-and-Trap/GC/FID of Apple Volatiles. Detection and quantification of apple volatiles from a complex matrix using an FID required baseline resolution. This was obtained using a longer column and slower chromatographic techniques (Figure 6b). The total time invested per analysis for purge-and-trap/traditional GC/FID was between 100 and 120 min.

DISCUSSION

Investigations of aroma synthesis in biological systems often require an analytical system that is capable of both high throughput and adaptability to static and flow-through measurements of various volumes. To date, much of the time investment in flavor analyses has been for sample collection and preparation. Sampling methods for extracting flavor compounds from horticultural products include direct headspace (Neubeller and Bochloh, 1982), liquid—liquid extraction (Weurman, 1969), supercritical extraction (Bundschuh et al., 1986), and dynamic headspace with adsorbents such as charcoal (Streif, 1981) or Tenax (Dirinck et al., 1989). However, the disadvantages of these methods are the lengthy analysis time, which has significantly limited sample throughput and added to experimental complexity.

Ideally, analytical methods for flavor research on horticultural produce should be fast, inexpensive, solventless, relatively independent of the instrument design, and amenable to automation. They should also be applicable to gaseous and liquid samples and have a large linear dynamic range while retaining excellent detection limits. Furthermore, they should be able to function as a screening technique or be used in the quantitative analysis of selected volatile compounds or classes of compounds for monitoring physiological processes that can be directly related to biochemical changes. SPME meets these criteria (Louch et al., 1992; Zhang and Pawliszyn, 1993; Buchholz and Pawliszyn, 1994).

The primary factors affecting the linear range and sensitivity of detection using SPME are the fiber's stationary phase and the properties of the GC detector. In our research, SPME exhibited good linearity of response for volatiles ranging in concentration from ppb to ppm with negligible effects from matrix variations (i.e., water vapor). Volatile concentrations in horticultural produce vary from 0.01 to 10 ppm (Paillard, 1990). Dominant volatiles like butyl acetate and hexyl acetate can reach the 0.5—1 ppm level during fruit ripening (Paillard, 1990), and hexanal in tomatoes can be as high as 3.1 ppm (Buttery et al., 1989). This suggests that SPME sampling should be sensitive enough to be used for dynamic investigations of impact volatiles. For

Analysis of Flavor Compounds Using SPME and GC/TOFMS

J. Agric. Food Chem., Vol. 45, No. 5, 1997 1005
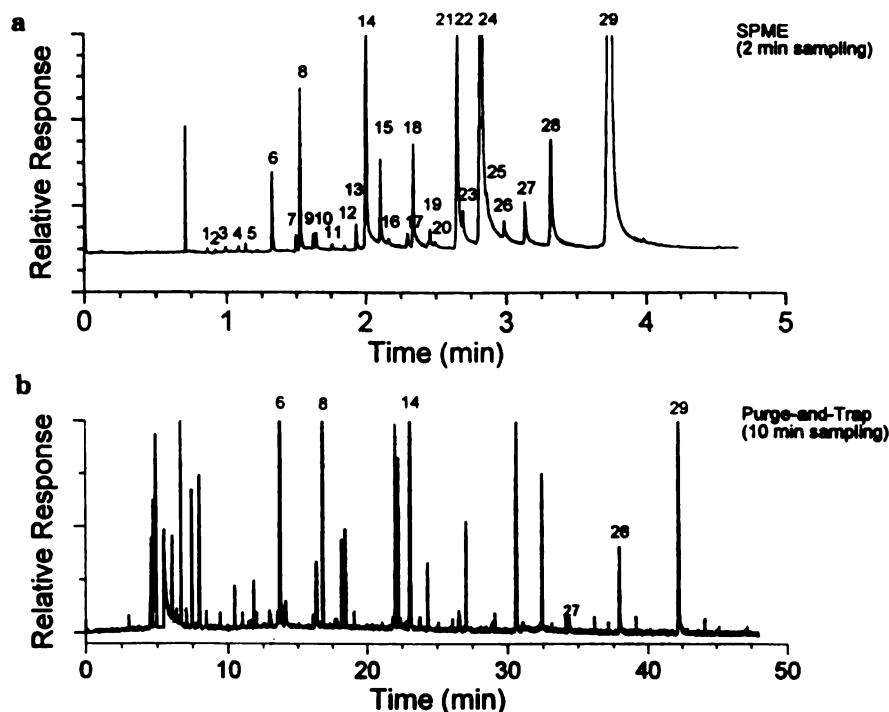
Figure 6. Qualitative comparison of chromatograms for SPME/GC/TOFMS and traditional purge-and-trap volatile headspace analysis with GC/FID.
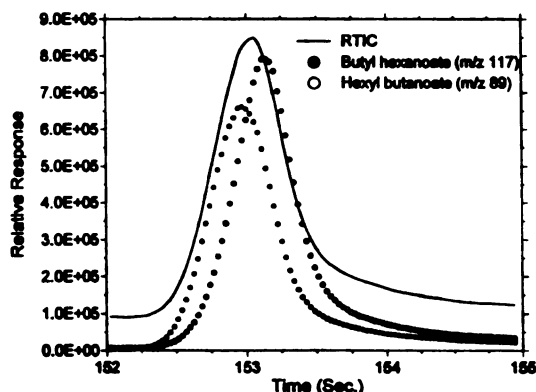
Figure 7. Demonstration of high speed spectral generation (40 spectra/s) enabling the detection and quantification of co-eluting compounds by using GC/TOFMS. The solid line represents the reconstructed total ion current (RTIC). Retention times differ by approximately 0.2 s.

SPME, the capacity of the fiber is a function of the stationary-phase volume and adsorption coefficient for the various volatiles. The PDMS coating used in this study favored adsorption of larger, more lipophilic compounds. However, adsorption can be tailored to fit the needs of a particular research thrust. For instance, it is most efficient to use thick films for compounds with low partition coefficients (Zhang and Pawliszyn, 1993); in our case, thin films are adequate for analytes with high partition coefficients such as 6-methyl-5-hepten-2-one and α-farnesene. To date, however, there are not adequate data regarding partition coefficients of SPME coatings for fruit volatiles.

The equilibration time of the SPME fiber plays an important role in quantitative sampling and is affected by the K value of the SPME coating for individual

volatiles and their respective diffusion coefficients. Zhang and Pawliszyn (1993) reported that BTEX (benzene, toluene, ethyl benzene, and xylene isomers) require just 2–5 min to reach equilibration. In our experiments using the mixed standards and apple samples, 6–8 min were required for most volatiles. Some compounds like hexyl 2-methylbutanoate and α-farnesene take more than 24 min to reach equilibrium. These observations suggest that the kinetic behavior of the adsorption process, which differs with the nature of each analyte, is a factor that must be accommodated in any experimental protocol. Some compounds, such as butyl acetate and 2-methylbutyl acetate, exhibited matrix effects and are negatively influenced by other materials, which continue to increase in concentration (e.g., α-farnesene and hexyl 2-methylbutanoate). This strongly suggests that a competition for a limited adsorption capacity exists making it advisable to avoid approaching a saturation condition of the fiber coating material. Since the response variation in sampling is relatively low, the SPME can be used quantitatively if adsorption time is precisely maintained and the adsorption has not approached saturation.

Two minutes were required for sampling via SPME, generating a volatile profile that is qualitatively comparable with data using purge-and-trap techniques from this and earlier reports (Dirinck et al., 1977; Kakiuchi, 1986; Song and Bangerth, 1993). However, it should be pointed out that there may be marked quantitative differences in the same compounds between SPME and purge-and-trap sampling. For example, the higher proportion of α-farnesene relative to other volatiles for SPME as compared to purge-and-trap reported here (Table 2) and elsewhere (Kakiuchi et al., 1986; Song and Bangerth, 1993) is most likely due to discrimination on the basis of partition coefficients and also adsorption

kinetics. Calibration of the SPME fiber will be required for accurate quantification.

The rapid sampling of apple volatiles by SPME is complemented by the features of the TCC/TOFMS employed, which enabled analysis times to be reduced from hours to minutes. While a narrow bore column (0.1 mm i.d.) has been used to improve GC resolution and speed (Sacks and Akard, 1994), co-elution was unavoidable. However, the high spectral acquisition rate of the TOF mass spectrometer and the data quality is sufficient to permit quantitation of co-eluting compounds with elution times differing by as little as 0.2 s.

SPME sampling is solventless and much faster than purge-and-trap sampling. With the combination of fast GC and the time-of-flight mass spectrometer, the quantitative and qualitative analysis time can be shortened at least 10-fold. The system should be appropriate for real-time analysis of time-course studies on volatile biosynthesis by horticultural produce. It is independent of sample size, which opens the new possibilities for biochemical investigations using small (1–2 mL) vials of plant material.

CONCLUSIONS

The SPME system was found to be a convenient and appropriate sampling technology for rapid qualitative and quantitative analysis of volatile from horticultural produce. Sampling time can be reduced approximately 60-fold relative to conventional purge-and-trap. The primary limitation of the SPME system is that samples cannot be conveniently stored.

Time-compressed chromatography was successfully accomplished using a narrow bore (0.1 mm i.d.), short (5-m) column, and rapid temperature ramp rate (50 °C/min). Chromatographic time was reduced 10-fold relative to conventional methods with good resolution.

Use of TOFMS was found to be of sufficient sensitivity and speed to permit rapid and efficient detection of apple aroma volatiles. The speed of the detector, based on time array detection, makes it well-suited for application to rapid GC separations with the resultant time compression of peaks. Importantly, the rapid spectral generation rates and unskewed nature of spectra obtained enabled analytical resolution of chromatographically unseparated compounds. Because of the independence from chromatographically induced fragmentation pattern skewing, the resulting spectra were 'classic' in nature and easily library searchable. Additional speed is possible, since the mass spectrometer was operating at approximately 10% of its maximum rate, raising the possibility of having detection times of as little as 12 s for complex mixtures.

The analysis system described here appears to be highly appropriate for aroma analyses. The speed of the system overcomes the primary limitation of SPME fiber (i.e., sample storage) and permits collection of pertinent biological data in real time. Typical daily sampling throughput was in the range of 10–20 samples and could be increased to over 100. The factor now limiting total analytical speed is the data handling (i.e., identification, quantification, and reporting of detected compounds).

ABBREVIATIONS USED

FID, flame ionization detector; m/z, mass to charge ratio; PDMS, polydimethylsiloxane; RTIC, reconstructed total ion current; SPME, solid-phase microextraction;

TCC, time compressed chromatography; TOFMS, time-of-flight mass spectrometry.

LITERATURE CITED

Arthur, C. L.; Pawliszyn, J. Solid-phase Microextraction with Thermal Desorption using Fused Silica Optical Fibers. Anal. Chem. 1990, 62, 2145–2148.

Arthur, C. L.; Killam, L. M.; Buchholz, K. D.; Pawliszyn, J.; Berg, J. R. Automation and Optimization of Solid-phase Microextraction. Anal. Chem. 1992, 64, 1960–1966.

Buchholz, K. D.; Pawliszyn, J. Optimization of Solid-phase Microextraction Conditions for Determination of Phenols. Anal. Chem. 1994, 66, 160–167.

Bundschuh, E.; Tylla, M.; Baumann, G.; Gierschner, K. Gewinnung von natuerlichen Aromen aus Reststoffen der Lebensmittelproduktion mit Hilfe der CO₂-Hochdruckextraktion. Lebensm.-Wiss. Technol. 1986, 19, 493–496.

Buttery, R. G.; Ling, L. C.; Guadagni, D. G. Volatilities of Aldehydes, Ketones, and Esters in Dilute Water Solution. J. Agric. Food Chem. 1969, 17, 385–389.

Buttery, R. G.; Teranishi, R.; Flath, A.; Ling, L. C. Fresh tomato volatiles: Composition and sensory studies. In Flavor Chemistry: Trends and Developments; Teranishi, R., Buttery, R. G., Shahidi, F., Eds.; ACS Symposium Series 388; American Chemical Society: Washington, DC, 1989.

Dirinck, P.; Schreyen, L.; Schamp, N. Aroma Quality Evaluation of Tomatoes, Apples, and Strawberries. J. Agric. Food Chem. 1977, 25, 759–762.

Dirinck, P.; De Pooter, H.; Schamp, N. Aroma Development in Ripening Fruits. In Flavor Chemistry: Trends and Developments; ACS Symposium Series 388; Teranishi, R., Buttery, R. G., Shahidi, F., Eds.; American Chemical Society: Washington, DC, 1989; pp 23–34.

Gardner, B. D.; Johnson, J. A.; Artaev, V. B.; Sparkman, O. D.; Holland, J. F. Rapid Sampling for Rapid Analysis: A New Method for VOCs in Drinking Water. Proceedings of the 43th ASMS Conference on Mass Spectrometry and Allied Topics, Atlanta, GA, May 21–26, 1995.

Kakiuchi, N.; Moriguchi, S.; Fukuda, H.; Ichimura, N.; Kato, Y.; Banba, Y. Composition of Volatile Compounds of Apple Fruits in Relation to Cultivars. J. Jpn. Soc. Hortic. Sci. 1986, 55, 280–289.

Louch, D.; Motlagh, S.; Pawliszyn, J. Liquid-Coated Fused Silica Fibers. Anal. Chem. 1992, 64, 1187–1199.

Mattheis, J. P.; Fellman, J. K.; Chen, P. M.; Patterson, M. E. Changes in Headspace Volatiles During Physiological Development of Bisbee Delicious Apple Fruit. J. Agric. Food Chem. 1991, 39, 1902–1906.

Neubeller, J.; Buchloh, G. Aromen und andere Fruchtinhaltsstoffe verschiedener Erdbeersorten. Erwerbsobstbau 1978, 20, 189–192.

Nielsen, F.; Olsen, E.; Fredenslund, A. Henry's Law Constants and Infinite Dilution Activity Coefficients for Volatile Organic Compounds in Water by a Validated Batch Air Stripping Method. Environ. Sci. Technol. 1994, 28, 2133–2138.

Paillard, N. M. M. The Flavor of Apples, Pears and Quinces. In Food Flavors. Part C: The Flavor of Fruits; Morton, I. D., MacLeod, A. J., Eds.; Elsevier Science Publishers B.V.: Amsterdam, 1990; pp 1–42.

Robbins, G. A.; Wang, S.; Stuart, J. D. Using the Static Headspace Method to Determine Henry's Law Constants. Anal. Chem. 1993, 65, 3113–3118.

Sacks, R.; Akard, M. High-speed GC analysis of VOCs: Tunable Selectivity and Column Selection. Environ. Sci. Technol. 1994, 28, 428–433.

Song, J.; Bangerth, F. The Production and Changes of Volatile Compounds from Apple Fruits with Different Fruit Maturities. Acta Hortic. 1993, 368, 150–159.

Steffen, A.; Pawliszyn, J. Analysis of Flavor Volatiles using Headspace Solid-phase Microextraction. J. Agric. Food Chem. 1996, 44, 2187–2193.

Streif, J. Vereinfachte Methode zur schnellen gaschromatographischen Bestimmung von Fluechtigen Aromastoffen. Gartenbauwissenschaft 1981, 46, 72–75.

Werkhoff, P.; Bretschneider, W. Dynamic Headspace Gas Chromatography: Concentration of Volatile Components after Thermal Desorption by Intermediate Cryofocusing in a Cold Trap. *J. Chromatogr.* **1987**, *405*, 87−98.

Weurman, C. Isolation and Concentration of Volatiles in Food Odor Research. *J. Agric. Food Chem.* **1969**, *17*, 370−384.

Yang, X.; Peppard, T. Solid-phase Microextraction for Flavor Analysis. *J. Agric. Food Chem.* **1994**, *42*, 1925−1930.

Zhang, Z. Y.; Pawliszyn, J. Headspace Solid-phase Microextraction. *Anal. Chem.* **1993**, 65, 1843−1852.

Appendix B

```
// 05-16-95    TOFSORC3.CPP

/*    program to calculate ideal space-focusing acceleration field,
      modified from tofsourc.cpp to account for different x widths. */

#include <stdio.h>
#include <math.h>

// array size
#define MAXARRAY 251

// "constants" to change for various runs
#define MASS 56
#define CHARGE 1
#define DISTANCE 153        // drift length in cm
#define TIME 20.778         // time-of-flight in usec

// constants
#define CONVERSION_CONSTANT 1.017941
#define TOLERANCE .00000000005

main()
{
  int  mass=MASS,                    // mass in u
       q=CHARGE,                     // charge
       no_of_fields=MAXARRAY-1,
             i, j, k, m, n, m_old;

  float d=DISTANCE,                  // distance D in cm
        x[MAXARRAY],                 // array size
        C=CONVERSION_CONSTANT;       // conversion to non SI units

  double    E[MAXARRAY],             // electric
            sumxEj, sumxEk, sumEn, sumxEi,
            E_oldhigh, E_oldlow,
            U0, totalx, totalV;

  long double t;

  for (i=0; i<MAXARRAY; ++i)
  {
      E[i]=0;                        // initialize all E[i]
      x[i]=0.01;                     // initialize all x[i]
  }


  E[0]=1000;                         // seed 1st E
  x[1]=.648;                         // set 2nd x

  // initialize variables to zero
  m=0;
  m_old=m;
  E_oldlow=0;
  E_oldhigh=0;
  U0=0;
  totalx=0;
  totalV=0;
```

```
// print header info
    printf("mass=%d d=%f x[1]=%f x[2]=%f T=%f\n E[1]=%f\n",
        mass, d, x[1], x[2], TIME, E[1]);

for (m=1; m<=no_of_fields; ++m)     // set m=1 to adjust all fields
{
    if (m_old!=m)                   // do if 1st time through for this m
    {
        E[m]=E[m-1];
        E_oldhigh=0;
        E_oldlow=0;
        m_old=m;
    }

    sumEn=0;
    for (n=1; n<=m; ++n)
    {
        sumxEj=0;                               // initialize sum xEj
        for (j=n; j<=m; ++j)
        {
            sumxEj += x[j]*E[j];
        }

        sumxEk=0;                               // initialize sum xEk
        for (k=n+1; k<=m; ++k)
        {
            sumxEk += x[k]*E[k];
        }

        sumEn += (sqrt(U0+q*sumxEj)-sqrt(U0+q*sumxEk))/E[n]; // sum En
    } // end for n loop

    sumxEi=0;                                   // initialize sum Ei
    for (i=1; i<=m; ++i)
    {
        sumxEi += x[i]*E[i];
    }

    // find the actual time, t
    t=C*((d*sqrt(2*mass)/(2*sqrt(q*sumxEi)))+(sqrt(2*mass)/q)*sumEn);

    // compare actual time, t, with target time, TIME
    if ((t>TIME) && (t-TIME)>TOLERANCE)
    {
        E_oldlow=E[m];
        if (E_oldhigh==0)
        {
            E[m] += 0.1*E[m];
        }
        else
        {
            E[m]=(E[m]+E_oldhigh)/2;
        }
        --m;
    }
```

```
if ((t>TIME) && (t-TIME)<=TOLERANCE)
{
    totalx=totalx+x[m];
    totalV=totalV+(E[m]*x[m]);
    printf("%f %f \n", totalx, totalV);
}

if ((t<TIME) && (TIME-t)>TOLERANCE)
{
    E_oldhigh=E[m];
    E[m]=(E[m]+E_oldlow)/2;
    --m;
}

if ((t<TIME) && (TIME-t)<=TOLERANCE)
{
    totalx=totalx+x[m];
    totalV=totalV+(E[m]*x[m]);
    printf("%f %f \n", totalx, totalV);
}
} // end for m loop

return(1);
} // end fcn
```

NONLINEAR.mcd Program for modeling a multi-gridded ion source.
Given the ion source parameters, the arrival time at the detector is calculated for ions beginning at the acceleration region edge. The program then calculates the electric field and electrode voltages required for elements in the ionization region. (Written in Mathcad ver. 4.0)

Step 1: Identify ion source parameters

mass $\quad$ m $:= 56$

charge $\quad$ q $:= 1$

Unit conversion constant $\quad$ C $:= 1.017941$

acceleration length (cm) $\quad$ d $:= 0.648$

distance to detector (cm) $\quad$ D $:= 153$

voltage applied to acceleration region (volts) $\quad$ V0 $:= 1600$

Initial energy (eV) $\quad$ $U_0 := 0$

Distance between ionization region electrodes beginning at acceleration region electrode (cm) .

L1 $:= 0.124$ $\quad$ L4 $:= 0.302$ $\quad$ L7 $:= 0.302$

L2 $:= 0.303$ $\quad$ L5 $:= 0.303$ $\quad$ L8 $:= 0.302$

L3 $:= 0.302$ $\quad$ L6 $:= 0.302$ $\quad$ L9 $:= 0.259$

Ionization region center point between electrodes (cm).

s1 $:= 0.062$ $\quad$ s4 $:= 0.151$ $\quad$ s7 $:= 0.151$

s2 $:= 0.151$ $\quad$ s5 $:= 0.151$ $\quad$ s8 $:= 0.151$

s3 $:= 0.151$ $\quad$ s6 $:= 0.151$ $\quad$ s9 $:= 0.130$

Calculation of acceleration region electric field $\quad$ $E0 := \dfrac{V0}{d}$ $\quad$ $E0 = 2.469 \cdot 10^3$

Total length of ionization region $\quad$ $L1 + L2 + L3 + L4 + L5 + L6 + L7 + L8 + L9 = 2.499$

Seed values for electric field calculations

E1 $:= 80$ $\quad$ E4 $:= 8.4$ $\quad$ E7 $:= 8.4$

E2 $:= 10$ $\quad$ E5 $:= 8.4$ $\quad$ E8 $:= 8.4$

E3 $:= 8.3$ $\quad$ E6 $:= 8.4$ $\quad$ E9 $:= 8.4$

Step 2: Calculate ion arrival time (in μsec) at detector for ions traversing only the acceleration region.

$$ t_D := C \cdot \frac{D \cdot \sqrt{2 \cdot m}}{\left(2 \cdot \sqrt{V0}\right)} \qquad t_d := C \cdot \frac{\sqrt{2 \cdot m}}{q \cdot E0} \cdot \left(\sqrt{U_0 + q \cdot d \cdot E0} - \sqrt{U_0}\right) $$

$t_D = 20.603$ $\qquad\qquad$ $t_d = 0.175$

$$ t := t_D + t_d \qquad t = 20.778 $$

Step 3: Calculate the electric fields required for each ionization region where the axial location of the ionization region is between the electrodes at s(x).

Given

$$t = C \cdot \sqrt{2 \cdot m} \cdot \left[\frac{D}{\left(2 \cdot \sqrt{V0 + s1 \cdot E1}\right)} + \frac{\sqrt{U_0 + q \cdot s1 \cdot E1} - \sqrt{U_0}}{q \cdot E1} + \frac{\left[\sqrt{U_0 + q \cdot (s1 \cdot E1 + d \cdot E0)} - \sqrt{U_0 + q \cdot s1 \cdot E1}\right]}{q \cdot E0} \right]$$

E1 := Find(E1) V_1 := L1·E1 + V0

E1 = 327.759 $V_1 = 1.641 \cdot 10^3$

Given

$$t = C \cdot \sqrt{2 \cdot m} \cdot \left[\frac{D}{\left(2 \cdot \sqrt{V0 + s2 \cdot E2 + L1 \cdot E1}\right)} + \frac{\sqrt{U_0 + q \cdot s2 \cdot E2} - \sqrt{U_0}}{q \cdot E2} \dots \right.$$
$$\left. + \frac{\left[\sqrt{U_0 + q \cdot (s2 \cdot E2 + L1 \cdot E1)} - \sqrt{U_0 + q \cdot s2 \cdot E2}\right]}{q \cdot E1} \dots \right.$$
$$\left. + \frac{\sqrt{U_0 + q \cdot (s2 \cdot E2 + L1 \cdot E1 + d \cdot E0)} - \sqrt{U_0 + q \cdot (s2 \cdot E2 + L1 \cdot E1)}}{q \cdot E0} \right]$$

E2 := Find(E2) V_2 := L2·E2 + L1·E1 + V0

E2 = 158.807 $V_2 = 1.689 \cdot 10^3$

Given

$$t = C \cdot \sqrt{2 \cdot m} \cdot \left[\frac{D}{\left(2 \cdot \sqrt{V0 + s3 \cdot E3 + L2 \cdot E2 + L1 \cdot E1}\right)} + \frac{\sqrt{U_0 + q \cdot s3 \cdot E3} - \sqrt{U_0}}{q \cdot E3} \dots \right.$$
$$\left. + \frac{\left[\sqrt{U_0 + q \cdot (s3 \cdot E3 + L2 \cdot E2)} - \sqrt{U_0 + q \cdot s3 \cdot E3}\right]}{q \cdot E2} \dots \right.$$
$$\left. + \frac{\sqrt{U_0 + q \cdot (s3 \cdot E3 + L2 \cdot E2 + L1 \cdot E1)} - \sqrt{U_0 + q \cdot (s3 \cdot E3 + L2 \cdot E2)}}{q \cdot E1} \dots \right.$$
$$\left. + \frac{\left[\sqrt{U_0 + q \cdot (s3 \cdot E3 + L2 \cdot E2 + L1 \cdot E1 + d \cdot E0)} \dots + - \sqrt{U_0 + q \cdot (s3 \cdot E3 + L2 \cdot E2 + L1 \cdot E1)}\right]}{q \cdot E0} \right]$$

E3 := Find(E3) V_3 := L3·E3 + L2·E2 + L1·E1 + V0

E3 = 127.518 $V_3 = 1.727 \cdot 10^3$

Given

$$t = C \cdot \sqrt{2 \cdot m} \cdot \left[\frac{D}{2 \cdot \sqrt{V0 + s4 \cdot E4 + L3 \cdot E3 + L2 \cdot E2 + L1 \cdot E1}} \cdots \right.$$

$$+ \frac{\sqrt{U_0 + q \cdot s4 \cdot E4} - \sqrt{U_0}}{q \cdot E4} + \frac{\left[\sqrt{U_0 + q \cdot (s4 \cdot E4 + L3 \cdot E3)} - \sqrt{U_0 + q \cdot s4 \cdot E4} \right]}{q \cdot E3} \cdots$$

$$+ \frac{\left[\sqrt{U_0 + q \cdot (s4 \cdot E4 + L3 \cdot E3 + L2 \cdot E2)} \cdots + - \sqrt{U_0 + q \cdot (s4 \cdot E4 + L3 \cdot E3)} \right]}{q \cdot E2} + \frac{\left[\sqrt{U_0 + q \cdot (s4 \cdot E4 + L3 \cdot E3 + L2 \cdot E2 + L1 \cdot E1)} \cdots + - \sqrt{U_0 + q \cdot (s4 \cdot E4 + L3 \cdot E3 + L2 \cdot E2)} \right]}{q \cdot E1} .$$

$$\left. + \frac{\left[\sqrt{U_0 + q \cdot (s4 \cdot E4 + L3 \cdot E3 + L2 \cdot E2 + L1 \cdot E1 + d \cdot E0)} \cdots + - \sqrt{U_0 + q \cdot (s4 \cdot E4 + L3 \cdot E3 + L2 \cdot E2 + L1 \cdot E1)} \right]}{q \cdot E0} \right]$$

$E4 := Find(E4) \qquad V_4 := L4 \cdot E4 + L3 \cdot E3 + L2 \cdot E2 + L1 \cdot E1 + V0$

$E4 = 114.243 \qquad V_4 = 1.762 \bullet 10^3$

Given

$$t = C \cdot \sqrt{2 \cdot m} \cdot \left[\frac{D}{2 \cdot \sqrt{V0 + s5 \cdot E5 + L4 \cdot E4 + L3 \cdot E3 + L2 \cdot E2 + L1 \cdot E1}} \cdots \right.$$

$$+ \frac{\sqrt{U_0 + q \cdot s5 \cdot E5} - \sqrt{U_0}}{q \cdot E5} + \frac{\left[\sqrt{U_0 + q \cdot (s5 \cdot E5 + L4 \cdot E4)} - \sqrt{U_0 + q \cdot s5 \cdot E5} \right]}{q \cdot E4} \cdots$$

$$+ \frac{\left[\sqrt{U_0 + q \cdot (s5 \cdot E5 + L4 \cdot E4 + L3 \cdot E3)} \cdots + - \sqrt{U_0 + q \cdot (s5 \cdot E5 + L4 \cdot E4)} \right]}{q \cdot E3} + \frac{\left[\sqrt{U_0 + q \cdot (s5 \cdot E5 + L4 \cdot E4 + L3 \cdot E3 + L2 \cdot E2)} \cdots + - \sqrt{U_0 + q \cdot (s5 \cdot E5 + L4 \cdot E4 + L3 \cdot E3)} \right]}{q \cdot E2} .$$

$$+ \frac{\left[\sqrt{U_0 + q \cdot (s5 \cdot E5 + L4 \cdot E4 + L3 \cdot E3 + L2 \cdot E2 + L1 \cdot E1)} \cdots + - \sqrt{U_0 + q \cdot (s5 \cdot E5 + L4 \cdot E4 + L3 \cdot E3 + L2 \cdot E2)} \right]}{q \cdot E1} \cdots$$

$$\left. + \frac{\left[\sqrt{U_0 + q \cdot (s5 \cdot E5 + L4 \cdot E4 + L3 \cdot E3 + L2 \cdot E2 + L1 \cdot E1 + d \cdot E0)} \cdots + - \sqrt{U_0 + q \cdot (s5 \cdot E5 + L4 \cdot E4 + L3 \cdot E3 + L2 \cdot E2 + L1 \cdot E1)} \right]}{q \cdot E0} \right]$$

$E5 := Find(E5) \qquad V_5 := L5 \cdot E5 + L4 \cdot E4 + L3 \cdot E3 + L2 \cdot E2 + L1 \cdot E1 + V0$

$E5 = 105.454 \qquad V_5 = 1.794 \bullet 10^3$

Given

$$t = C \cdot \sqrt{2 \cdot m} \cdot \left[\frac{D}{\left(2 \cdot \sqrt{s6 \cdot E6 + L5 \cdot E5 + L4 \cdot E4 + L3 \cdot E3 + L2 \cdot E2 + L1 \cdot E1 + V0}\right)} + \frac{\sqrt{U_0 + q \cdot s6 \cdot E6} - \sqrt{U_0}}{q \cdot E6} \ldots \right.$$

$$+ \frac{\left[\sqrt{U_0 + q \cdot (s6 \cdot E6 + L5 \cdot E5)} - \sqrt{U_0 + q \cdot s6 \cdot E6}\right]}{q \cdot E5} + \frac{\left[\sqrt{U_0 + q \cdot (s6 \cdot E6 + L5 \cdot E5 + L4 \cdot E4)} \ldots + -\sqrt{U_0 + q \cdot (s6 \cdot E6 + L5 \cdot E5)}\right]}{q \cdot E4} \ldots$$

$$+ \frac{\left[\sqrt{U_0 + q \cdot (s6 \cdot E6 + L5 \cdot E5 + L4 \cdot E4 + L3 \cdot E3)} \ldots + -\sqrt{U_0 + q \cdot (s6 \cdot E6 + L5 \cdot E5 + L4 \cdot E4)}\right]}{q \cdot E3} \ldots$$

$$+ \frac{\left[\sqrt{U_0 + q \cdot (s6 \cdot E6 + L5 \cdot E5 + L4 \cdot E4 + L3 \cdot E3 + L2 \cdot E2)} \ldots + -\sqrt{U_0 + q \cdot (s6 \cdot E6 + L5 \cdot E5 + L4 \cdot E4 + L3 \cdot E3)}\right]}{q \cdot E2} \ldots$$

$$+ \frac{\left[\sqrt{U_0 + q \cdot (s6 \cdot E6 + L5 \cdot E5 + L4 \cdot E4 + L3 \cdot E3 + L2 \cdot E2 + L1 \cdot E1)} \ldots + -\sqrt{U_0 + q \cdot (s6 \cdot E6 + L5 \cdot E5 + L4 \cdot E4 + L3 \cdot E3 + L2 \cdot E2)}\right]}{q \cdot E1} \ldots$$

$$\left. + \frac{\left[\sqrt{U_0 + q \cdot (s6 \cdot E6 + L5 \cdot E5 + L4 \cdot E4 + L3 \cdot E3 + L2 \cdot E2 + L1 \cdot E1 + d \cdot E0)} \ldots + -\sqrt{U_0 + q \cdot (s6 \cdot E6 + L5 \cdot E5 + L4 \cdot E4 + L3 \cdot E3 + L2 \cdot E2 + L1 \cdot E1)}\right]}{q \cdot E0} \right]$$

$E6 := \text{Find}(E6)$ $V_6 := L6 \cdot E6 + L5 \cdot E5 + L4 \cdot E4 + L3 \cdot E3 + L2 \cdot E2 + L1 \cdot E1 + V0$

$E6 = 99.364$ $V_6 = 1.824 \cdot 10^3$

Given

$$t = C \cdot \sqrt{2 \cdot m} \cdot \left[\frac{D}{2 \cdot \sqrt{s7 \cdot E7 + L6 \cdot E6 + L5 \cdot E5 + L4 \cdot E4 + L3 \cdot E3 + L2 \cdot E2 + L1 \cdot E1 + V0}} \cdots \right.$$

$$+ \frac{\sqrt{U_0 + q \cdot s7 \cdot E7} - \sqrt{U_0}}{q \cdot E7} + \frac{\left[\sqrt{U_0 + q \cdot (s7 \cdot E7 + L6 \cdot E6)} - \sqrt{U_0 + q \cdot s7 \cdot E7} \right]}{q \cdot E6} \cdots$$

$$+ \frac{\left[\sqrt{U_0 + q \cdot (s7 \cdot E7 + L6 \cdot E6 + L5 \cdot E5)} \cdots + -\sqrt{U_0 + q \cdot (s7 \cdot E7 + L6 \cdot E6)} \right]}{q \cdot E5} + \frac{\left[\sqrt{U_0 + q \cdot (s7 \cdot E7 + L6 \cdot E6 + L5 \cdot E5 + L4 \cdot E4)} \cdots + -\sqrt{U_0 + q \cdot (s7 \cdot E7 + L6 \cdot E6 + L5 \cdot E5)} \right]}{q \cdot E4}.$$

$$+ \frac{\left[\sqrt{U_0 + q \cdot (s7 \cdot E7 + L6 \cdot E6 + L5 \cdot E5 + L4 \cdot E4 + L3 \cdot E3)} \cdots + -\sqrt{U_0 + q \cdot (s7 \cdot E7 + L6 \cdot E6 + L5 \cdot E5 + L4 \cdot E4)} \right]}{q \cdot E3} \cdots$$

$$+ \frac{\left[\sqrt{U_0 + q \cdot (s7 \cdot E7 + L6 \cdot E6 + L5 \cdot E5 + L4 \cdot E4 + L3 \cdot E3 + L2 \cdot E2)} \cdots + -\sqrt{U_0 + q \cdot (s7 \cdot E7 + L6 \cdot E6 + L5 \cdot E5 + L4 \cdot E4 + L3 \cdot E3)} \right]}{q \cdot E2} \cdots$$

$$+ \frac{\left[\sqrt{U_0 + q \cdot (s7 \cdot E7 + L6 \cdot E6 + L5 \cdot E5 + L4 \cdot E4 + L3 \cdot E3 + L2 \cdot E2 + L1 \cdot E1)} \cdots + -\sqrt{U_0 + q \cdot (s7 \cdot E7 + L6 \cdot E6 + L5 \cdot E5 + L4 \cdot E4 + L3 \cdot E3 + L2 \cdot E2)} \right]}{q \cdot E1} \cdots$$

$$\left. + \frac{\left[\sqrt{U_0 + q \cdot (s7 \cdot E7 + L6 \cdot E6 + L5 \cdot E5 + L4 \cdot E4 + L3 \cdot E3 + L2 \cdot E2 + L1 \cdot E1 + d \cdot E0)} \cdots + -\sqrt{U_0 + q \cdot (s7 \cdot E7 + L6 \cdot E6 + L5 \cdot E5 + L4 \cdot E4 + L3 \cdot E3 + L2 \cdot E2 + L1 \cdot E1)} \right]}{q \cdot E0} \right]$$

$E7 := \text{Find}(E7) \qquad V_7 := L7 \cdot E7 + L6 \cdot E6 + L5 \cdot E5 + L4 \cdot E4 + L3 \cdot E3 + L2 \cdot E2 + L1 \cdot E1 + V0$

$E7 = 94.799 \qquad V_7 = 1.852 \cdot 10^3$

137

Given

$$t = C \cdot \sqrt{2 \cdot m} \cdot \left[\frac{D}{2 \cdot \sqrt{s8 \cdot E8 + L7 \cdot E7 + L6 \cdot E6 + L5 \cdot E5 + L4 \cdot E4 + L3 \cdot E3 + L2 \cdot E2 + L1 \cdot E1 + V0}} \dots \right.$$

$$+ \frac{\sqrt{U_0 + q \cdot s8 \cdot E8} - \sqrt{U_0}}{q \cdot E8} + \frac{\left[\sqrt{U_0 + q \cdot (s8 \cdot E8 + L7 \cdot E7)} - \sqrt{U_0 + q \cdot s8 \cdot E8} \right]}{q \cdot E7} \dots$$

$$+ \frac{\left[\sqrt{U_0 + q \cdot (s8 \cdot E8 + L7 \cdot E7 + L6 \cdot E6)} \dots + - \sqrt{U_0 + q \cdot (s8 \cdot E8 + L7 \cdot E7)} \right]}{q \cdot E6} + \frac{\left[\sqrt{U_0 + q \cdot (s8 \cdot E8 + L7 \cdot E7 + L6 \cdot E6 + L5 \cdot E5)} \dots + - \sqrt{U_0 + q \cdot (s8 \cdot E8 + L7 \cdot E7 + L6 \cdot E6)} \right]}{q \cdot E5} \,.$$

$$+ \frac{\left[\sqrt{U_0 + q \cdot (s8 \cdot E8 + L7 \cdot E7 + L6 \cdot E6 + L5 \cdot E5 + L4 \cdot E4)} \dots + - \sqrt{U_0 + q \cdot (s8 \cdot E8 + L7 \cdot E7 + L6 \cdot E6 + L5 \cdot E5)} \right]}{q \cdot E4} \dots$$

$$+ \frac{\left[\sqrt{U_0 + q \cdot (s8 \cdot E8 + L7 \cdot E7 + L6 \cdot E6 + L5 \cdot E5 + L4 \cdot E4 + L3 \cdot E3)} \dots + - \sqrt{U_0 + q \cdot (s8 \cdot E8 + L7 \cdot E7 + L6 \cdot E6 + L5 \cdot E5 + L4 \cdot E4)} \right]}{q \cdot E3} \dots$$

$$+ \frac{\left[\sqrt{U_0 + q \cdot (s8 \cdot E8 + L7 \cdot E7 + L6 \cdot E6 + L5 \cdot E5 + L4 \cdot E4 + L3 \cdot E3 + L2 \cdot E2)} \dots + - \sqrt{U_0 + q \cdot (s8 \cdot E8 + L7 \cdot E7 + L6 \cdot E6 + L5 \cdot E5 + L4 \cdot E4 + L3 \cdot E3)} \right]}{q \cdot E2} \dots$$

$$+ \frac{\left[\sqrt{U_0 + q \cdot (s8 \cdot E8 + L7 \cdot E7 + L6 \cdot E6 + L5 \cdot E5 + L4 \cdot E4 + L3 \cdot E3 + L2 \cdot E2 + L1 \cdot E1)} \dots + - \sqrt{U_0 + q \cdot (s8 \cdot E8 + L7 \cdot E7 + L6 \cdot E6 + L5 \cdot E5 + L4 \cdot E4 + L3 \cdot E3 + L2 \cdot E2)} \right]}{q \cdot E1} \dots$$

$$\left. + \frac{\left[\sqrt{U_0 + q \cdot (s8 \cdot E8 + L7 \cdot E7 + L6 \cdot E6 + L5 \cdot E5 + L4 \cdot E4 + L3 \cdot E3 + L2 \cdot E2 + L1 \cdot E1 + d \cdot E0)} \dots + - \sqrt{U_0 + q \cdot (s8 \cdot E8 + L7 \cdot E7 + L6 \cdot E6 + L5 \cdot E5 + L4 \cdot E4 + L3 \cdot E3 + L2 \cdot E2 + L1 \cdot E1)} \right]}{q \cdot E0} \right]$$

E8 := Find(E8) V_8 := L8·E8 + L7·E7 + L6·E6 + L5·E5 + L4·E4 + L3·E3 + L2·E2 + L1·E1 + V0

E8 = 91.205 $V_8 = 1.88 \cdot 10^3$

Given

$$t = C \cdot \sqrt{2 \cdot m} \cdot \left[\frac{D}{2 \cdot \sqrt{s9 \cdot E9 + L8 \cdot E8 + L7 \cdot E7 + L6 \cdot E6 + L5 \cdot E5 + L4 \cdot E4 + L3 \cdot E3 + L2 \cdot E2 + L1 \cdot E1 + V0}} \right. \dots$$

$$+ \frac{\sqrt{U_0 + q \cdot s9 \cdot E9} - \sqrt{U_0}}{q \cdot E9} + \frac{\left[\sqrt{U_0 + q \cdot (s9 \cdot E9 + L8 \cdot E8)} - \sqrt{U_0 + q \cdot s9 \cdot E9} \right]}{q \cdot E8} \dots$$

$$+ \frac{\left[\sqrt{U_0 + q \cdot (s9 \cdot E9 + L8 \cdot E8 + L7 \cdot E7)} \dots + - \sqrt{U_0 + q \cdot (s9 \cdot E9 + L8 \cdot E8)} \right]}{q \cdot E7} + \frac{\left[\sqrt{U_0 + q \cdot (s9 \cdot E9 + L8 \cdot E8 + L7 \cdot E7 + L6 \cdot E6)} \dots + - \sqrt{U_0 + q \cdot (s9 \cdot E9 + L8 \cdot E8 + L7 \cdot E7)} \right]}{q \cdot E6}.$$

$$+ \frac{\left[\sqrt{U_0 + q \cdot (s9 \cdot E9 + L8 \cdot E8 + L7 \cdot E7 + L6 \cdot E6 + L5 \cdot E5)} \dots + - \sqrt{U_0 + q \cdot (s9 \cdot E9 + L8 \cdot E8 + L7 \cdot E7 + L6 \cdot E6)} \right]}{q \cdot E5} \dots$$

$$+ \frac{\left[\sqrt{U_0 + q \cdot (s9 \cdot E9 + L8 \cdot E8 + L7 \cdot E7 + L6 \cdot E6 + L5 \cdot E5 + L4 \cdot E4)} \dots + - \sqrt{U_0 + q \cdot (s9 \cdot E9 + L8 \cdot E8 + L7 \cdot E7 + L6 \cdot E6 + L5 \cdot E5)} \right]}{q \cdot E4} \dots$$

$$+ \frac{\left[\sqrt{U_0 + q \cdot (s9 \cdot E9 + L8 \cdot E8 + L7 \cdot E7 + L6 \cdot E6 + L5 \cdot E5 + L4 \cdot E4 + L3 \cdot E3)} \dots + - \sqrt{U_0 + q \cdot (s9 \cdot E9 + L8 \cdot E8 + L7 \cdot E7 + L6 \cdot E6 + L5 \cdot E5 + L4 \cdot E4)} \right]}{q \cdot E3} \dots$$

$$+ \frac{\left[\sqrt{U_0 + q \cdot (s9 \cdot E9 + L8 \cdot E8 + L7 \cdot E7 + L6 \cdot E6 + L5 \cdot E5 + L4 \cdot E4 + L3 \cdot E3 + L2 \cdot E2)} \dots + - \sqrt{U_0 + q \cdot (s9 \cdot E9 + L8 \cdot E8 + L7 \cdot E7 + L6 \cdot E6 + L5 \cdot E5 + L4 \cdot E4 + L3 \cdot E3)} \right]}{q \cdot E2} \dots$$

$$+ \frac{\left[\sqrt{U_0 + q \cdot (s9 \cdot E9 + L8 \cdot E8 + L7 \cdot E7 + L6 \cdot E6 + L5 \cdot E5 + L4 \cdot E4 + L3 \cdot E3 + L2 \cdot E2 + L1 \cdot E1)} \dots + - \sqrt{U_0 + q \cdot (s9 \cdot E9 + L8 \cdot E8 + L7 \cdot E7 + L6 \cdot E6 + L5 \cdot E5 + L4 \cdot E4 + L3 \cdot E3 + L2 \cdot E2)} \right]}{q \cdot E1} \dots$$

$$+ \left. \frac{\left[\sqrt{U_0 + q \cdot \left(\begin{array}{c} s9 \cdot E9 + L8 \cdot E8 + L7 \cdot E7 + L6 \cdot E6 + L5 \cdot E5 \dots \\ + L4 \cdot E4 + L3 \cdot E3 + L2 \cdot E2 + L1 \cdot E1 + d \cdot E0 \end{array} \right)} \dots + - \sqrt{U_0 + q \cdot \left(\begin{array}{c} s9 \cdot E9 + L8 \cdot E8 + L7 \cdot E7 + L6 \cdot E6 \dots \\ + L5 \cdot E5 + L4 \cdot E4 + L3 \cdot E3 + L2 \cdot E2 + L1 \cdot E1 \end{array} \right)} \right]}{q \cdot E0} \right]$$

E9 := Find(E9) $V_n := L9 \cdot E9 + L8 \cdot E8 + L7 \cdot E7 + L6 \cdot E6 + L5 \cdot E5 + L4 \cdot E4 + L3 \cdot E3 + L2 \cdot E2 + L1 \cdot E1 + V($

E9 = 88.356 $V_9 = 1.903 \cdot 10^3$

Summary of required voltages

$$V_1 = 1.641 \cdot 10^3 \qquad V_4 = 1.762 \cdot 10^3 \qquad V_7 = 1.852 \cdot 10^3$$

$$V_2 = 1.689 \cdot 10^3 \qquad V_5 = 1.794 \cdot 10^3 \qquad V_8 = 1.88 \cdot 10^3$$

$$V_3 = 1.727 \cdot 10^3 \qquad V_6 = 1.824 \cdot 10^3 \qquad V_9 = 1.903 \cdot 10^3$$

Step 4: Calculation of actual flight time for ions beginning at any axial location within the ionization region. The output is graphical.

$s1 := 0.000, 0.001 .. L1$

$$f(s1) := C \cdot \sqrt{2 \cdot m} \cdot \left[\frac{D}{\left(2 \cdot \sqrt{V0 + s1 \cdot E1}\right)} + \frac{\sqrt{U_0 + q \cdot s1 \cdot E1} - \sqrt{U_0}}{q \cdot E1} \cdots \right. \\ \left. + \frac{\left[\sqrt{U_0 + q \cdot (s1 \cdot E1 + d \cdot E0)} - \sqrt{U_0 + q \cdot s1 \cdot E1}\right]}{q \cdot E0} \right]$$

$s2 := 0.000, 0.001 .. L2$

$$g(s2) := C \cdot \sqrt{2 \cdot m} \cdot \left[\frac{D}{\left(2 \cdot \sqrt{V0 + s2 \cdot E2 + L1 \cdot E1}\right)} + \frac{\sqrt{U_0 + q \cdot s2 \cdot E2} - \sqrt{U_0}}{q \cdot E2} \cdots \right. \\ + \frac{\left[\sqrt{U_0 + q \cdot (s2 \cdot E2 + L1 \cdot E1)} - \sqrt{U_0 + q \cdot s2 \cdot E2}\right]}{q \cdot E1} \cdots \\ \left. + \frac{\left[\sqrt{U_0 + q \cdot (s2 \cdot E2 + L1 \cdot E1 + d \cdot E0)} - \sqrt{U_0 + q \cdot (s2 \cdot E2 + L1 \cdot E1)}\right]}{q \cdot E0} \right]$$

$s3 := 0.000, 0.001 .. L3$

$$h(s3) := C \cdot \sqrt{2 \cdot m} \cdot \left[\frac{D}{\left(2 \cdot \sqrt{V0 + s3 \cdot E3 + L2 \cdot E2 + L1 \cdot E1}\right)} + \frac{\sqrt{U_0 + q \cdot s3 \cdot E3} - \sqrt{U_0}}{q \cdot E3} \cdots \right. \\ + \frac{\left[\sqrt{U_0 + q \cdot (s3 \cdot E3 + L2 \cdot E2)} - \sqrt{U_0 + q \cdot s3 \cdot E3}\right]}{q \cdot E2} \cdots \\ + \frac{\left[\sqrt{U_0 + q \cdot (s3 \cdot E3 + L2 \cdot E2 + L1 \cdot E1)} - \sqrt{U_0 + q \cdot (s3 \cdot E3 + L2 \cdot E2)}\right]}{q \cdot E1} \cdots \\ \left. + \frac{\left[\sqrt{U_0 + q \cdot (s3 \cdot E3 + L2 \cdot E2 + L1 \cdot E1 + d \cdot E0)} - \sqrt{U_0 + q \cdot (s3 \cdot E3 + L2 \cdot E2 + L1 \cdot E1)}\right]}{q \cdot E0} \right]$$

$$s4 := 0.000, 0.001 .. L4$$

$$i(s4) := C \cdot \sqrt{2 \cdot m} \cdot \left[\frac{D}{\left(2 \cdot \sqrt{V0 + s4 \cdot E4 + L3 \cdot E3 + L2 \cdot E2 + L1 \cdot E1}\right)} + \frac{\sqrt{U_0 + q \cdot s4 \cdot E4} - \sqrt{U_0}}{q \cdot E4} \; ... \right.$$

$$+ \frac{\sqrt{U_0 + q \cdot (s4 \cdot E4 + L3 \cdot E3)} - \sqrt{U_0 + q \cdot s4 \cdot E4}}{q \cdot E3} \; ...$$

$$+ \frac{\left[\sqrt{U_0 + q \cdot (s4 \cdot E4 + L3 \cdot E3 + L2 \cdot E2)} - \sqrt{U_0 + q \cdot (s4 \cdot E4 + L3 \cdot E3)}\right]}{q \cdot E2} \; ...$$

$$+ \frac{\left[\sqrt{U_0 + q \cdot (s4 \cdot E4 + L3 \cdot E3 + L2 \cdot E2 + L1 \cdot E1)} - \sqrt{U_0 + q \cdot (s4 \cdot E4 + L3 \cdot E3 + L2 \cdot E2)}\right]}{q \cdot E1} \; ...$$

$$\left. + \frac{\left[\begin{array}{l}\sqrt{U_0 + q \cdot (s4 \cdot E4 + L3 \cdot E3 + L2 \cdot E2 + L1 \cdot E1 + d \cdot E0)} \; ... \\ + - \sqrt{U_0 + q \cdot (s4 \cdot E4 + L3 \cdot E3 + L2 \cdot E2 + L1 \cdot E1)}\end{array}\right]}{q \cdot E0} \right]$$

$$s5 := 0.000, 0.001 .. L5$$

$$j(s5) := C \cdot \sqrt{2 \cdot m} \cdot \left[\frac{D}{2 \cdot \sqrt{V0 + s5 \cdot E5 + L4 \cdot E4 + L3 \cdot E3 + L2 \cdot E2 + L1 \cdot E1}} \; ... \right.$$

$$+ \frac{\sqrt{U_0 + q \cdot s5 \cdot E5} - \sqrt{U_0}}{q \cdot E5} + \frac{\left[\sqrt{U_0 + q \cdot (s5 \cdot E5 + L4 \cdot E4)} - \sqrt{U_0 + q \cdot s5 \cdot E5}\right]}{q \cdot E4} \; ...$$

$$+ \frac{\left[\begin{array}{l}\sqrt{U_0 + q \cdot (s5 \cdot E5 + L4 \cdot E4 + L3 \cdot E3)} \; ... \\ + - \sqrt{U_0 + q \cdot (s5 \cdot E5 + L4 \cdot E4)}\end{array}\right]}{q \cdot E3} \; ...$$

$$+ \frac{\left[\begin{array}{l}\sqrt{U_0 + q \cdot (s5 \cdot E5 + L4 \cdot E4 + L3 \cdot E3 + L2 \cdot E2)} \; ... \\ + - \sqrt{U_0 + q \cdot (s5 \cdot E5 + L4 \cdot E4 + L3 \cdot E3)}\end{array}\right]}{q \cdot E2} \; ...$$

$$+ \frac{\left[\begin{array}{l}\sqrt{U_0 + q \cdot (s5 \cdot E5 + L4 \cdot E4 + L3 \cdot E3 + L2 \cdot E2 + L1 \cdot E1)} \; ... \\ + - \sqrt{U_0 + q \cdot (s5 \cdot E5 + L4 \cdot E4 + L3 \cdot E3 + L2 \cdot E2)}\end{array}\right]}{q \cdot E1} \; ...$$

$$\left. + \frac{\left[\begin{array}{l}\sqrt{U_0 + q \cdot (s5 \cdot E5 + L4 \cdot E4 + L3 \cdot E3 + L2 \cdot E2 + L1 \cdot E1 + d \cdot E0)} \; ... \\ + - \sqrt{U_0 + q \cdot (s5 \cdot E5 + L4 \cdot E4 + L3 \cdot E3 + L2 \cdot E2 + L1 \cdot E1)}\end{array}\right]}{q \cdot E0} \right]$$

$$s6 := 0.000, 0.001 .. L6$$

$$k(s6) := C \cdot \sqrt{2 \cdot m} \cdot \left[\frac{D}{2 \cdot \sqrt{V0 + s6 \cdot E6 + L5 \cdot E5 + L4 \cdot E4 + L3 \cdot E3 + L2 \cdot E2 + L1 \cdot E1}} \ldots \right.$$

$$+ \frac{\sqrt{U_0 + q \cdot s6 \cdot E6} - \sqrt{U_0}}{q \cdot E6} + \frac{\left[\sqrt{U_0 + q \cdot (s6 \cdot E6 + L5 \cdot E5)} - \sqrt{U_0 + q \cdot s6 \cdot E6} \right]}{q \cdot E5} \ldots$$

$$+ \frac{\left[\sqrt{U_0 + q \cdot (s6 \cdot E6 + L5 \cdot E5 + L4 \cdot E4)} \ldots + - \sqrt{U_0 + q \cdot (s6 \cdot E6 + L5 \cdot E5)} \right]}{q \cdot E4} \ldots$$

$$+ \frac{\left[\sqrt{U_0 + q \cdot (s6 \cdot E6 + L5 \cdot E5 + L4 \cdot E4 + L3 \cdot E3)} \ldots + - \sqrt{U_0 + q \cdot (s6 \cdot E6 + L5 \cdot E5 + L4 \cdot E4)} \right]}{q \cdot E3} \ldots$$

$$+ \frac{\left[\sqrt{U_0 + q \cdot (s6 \cdot E6 + L5 \cdot E5 + L4 \cdot E4 + L3 \cdot E3 + L2 \cdot E2)} \ldots + - \sqrt{U_0 + q \cdot (s6 \cdot E6 + L5 \cdot E5 + L4 \cdot E4 + L3 \cdot E3)} \right]}{q \cdot E2} \ldots$$

$$+ \frac{\left[\sqrt{U_0 + q \cdot (s6 \cdot E6 + L5 \cdot E5 + L4 \cdot E4 + L3 \cdot E3 + L2 \cdot E2 + L1 \cdot E1)} \ldots + - \sqrt{U_0 + q \cdot (s6 \cdot E6 + L5 \cdot E5 + L4 \cdot E4 + L3 \cdot E3 + L2 \cdot E2)} \right]}{q \cdot E1} \ldots$$

$$\left. + \frac{\left[\sqrt{U_0 + q \cdot (s6 \cdot E6 + L5 \cdot E5 + L4 \cdot E4 + L3 \cdot E3 + L2 \cdot E2 + L1 \cdot E1 + d \cdot E0)} \ldots + - \sqrt{U_0 + q \cdot (s6 \cdot E6 + L5 \cdot E5 + L4 \cdot E4 + L3 \cdot E3 + L2 \cdot E2 + L1 \cdot E1)} \right]}{q \cdot E0} \right]$$

$s7 := 0.000, 0.001 .. L7$

$$I(s7) := C \cdot \sqrt{2 \cdot m} \cdot \left[\frac{D}{2 \cdot \sqrt{s7 \cdot E7 + L6 \cdot E6 + L5 \cdot E5 + L4 \cdot E4 + L3 \cdot E3 + L2 \cdot E2 + L1 \cdot E1 + V0}} \cdots \right.$$

$$+ \frac{\sqrt{U_0 + q \cdot s7 \cdot E7} - \sqrt{U_0}}{q \cdot E7} + \frac{\left[\sqrt{U_0 + q \cdot (s7 \cdot E7 + L6 \cdot E6)} - \sqrt{U_0 + q \cdot s7 \cdot E7} \right]}{q \cdot E6} \cdots$$

$$+ \frac{\left[\sqrt{U_0 + q \cdot (s7 \cdot E7 + L6 \cdot E6 + L5 \cdot E5)} \cdots + - \sqrt{U_0 + q \cdot (s7 \cdot E7 + L6 \cdot E6)} \right]}{q \cdot E5} \cdots$$

$$+ \frac{\left[\sqrt{U_0 + q \cdot (s7 \cdot E7 + L6 \cdot E6 + L5 \cdot E5 + L4 \cdot E4)} \cdots + - \sqrt{U_0 + q \cdot (s7 \cdot E7 + L6 \cdot E6 + L5 \cdot E5)} \right]}{q \cdot E4} \cdots$$

$$+ \frac{\left[\sqrt{U_0 + q \cdot (s7 \cdot E7 + L6 \cdot E6 + L5 \cdot E5 + L4 \cdot E4 + L3 \cdot E3)} \cdots + - \sqrt{U_0 + q \cdot (s7 \cdot E7 + L6 \cdot E6 + L5 \cdot E5 + L4 \cdot E4)} \right]}{q \cdot E3} \cdots$$

$$+ \frac{\left[\sqrt{U_0 + q \cdot (s7 \cdot E7 + L6 \cdot E6 + L5 \cdot E5 + L4 \cdot E4 + L3 \cdot E3 + L2 \cdot E2)} \cdots + - \sqrt{U_0 + q \cdot (s7 \cdot E7 + L6 \cdot E6 + L5 \cdot E5 + L4 \cdot E4 + L3 \cdot E3)} \right]}{q \cdot E2} \cdots$$

$$+ \frac{\left[\sqrt{U_0 + q \cdot (s7 \cdot E7 + L6 \cdot E6 + L5 \cdot E5 + L4 \cdot E4 + L3 \cdot E3 + L2 \cdot E2 + L1 \cdot E1)} \cdots + - \sqrt{U_0 + q \cdot (s7 \cdot E7 + L6 \cdot E6 + L5 \cdot E5 + L4 \cdot E4 + L3 \cdot E3 + L2 \cdot E2)} \right]}{q \cdot E1} \cdots$$

$$\left. + \frac{\left[\sqrt{U_0 + q \cdot (s7 \cdot E7 + L6 \cdot E6 + L5 \cdot E5 + L4 \cdot E4 + L3 \cdot E3 + L2 \cdot E2 + L1 \cdot E1 + d \cdot E0)} \cdots + - \sqrt{U_0 + q \cdot (s7 \cdot E7 + L6 \cdot E6 + L5 \cdot E5 + L4 \cdot E4 + L3 \cdot E3 + L2 \cdot E2 + L1 \cdot E1)} \right]}{q \cdot E0} \right]$$
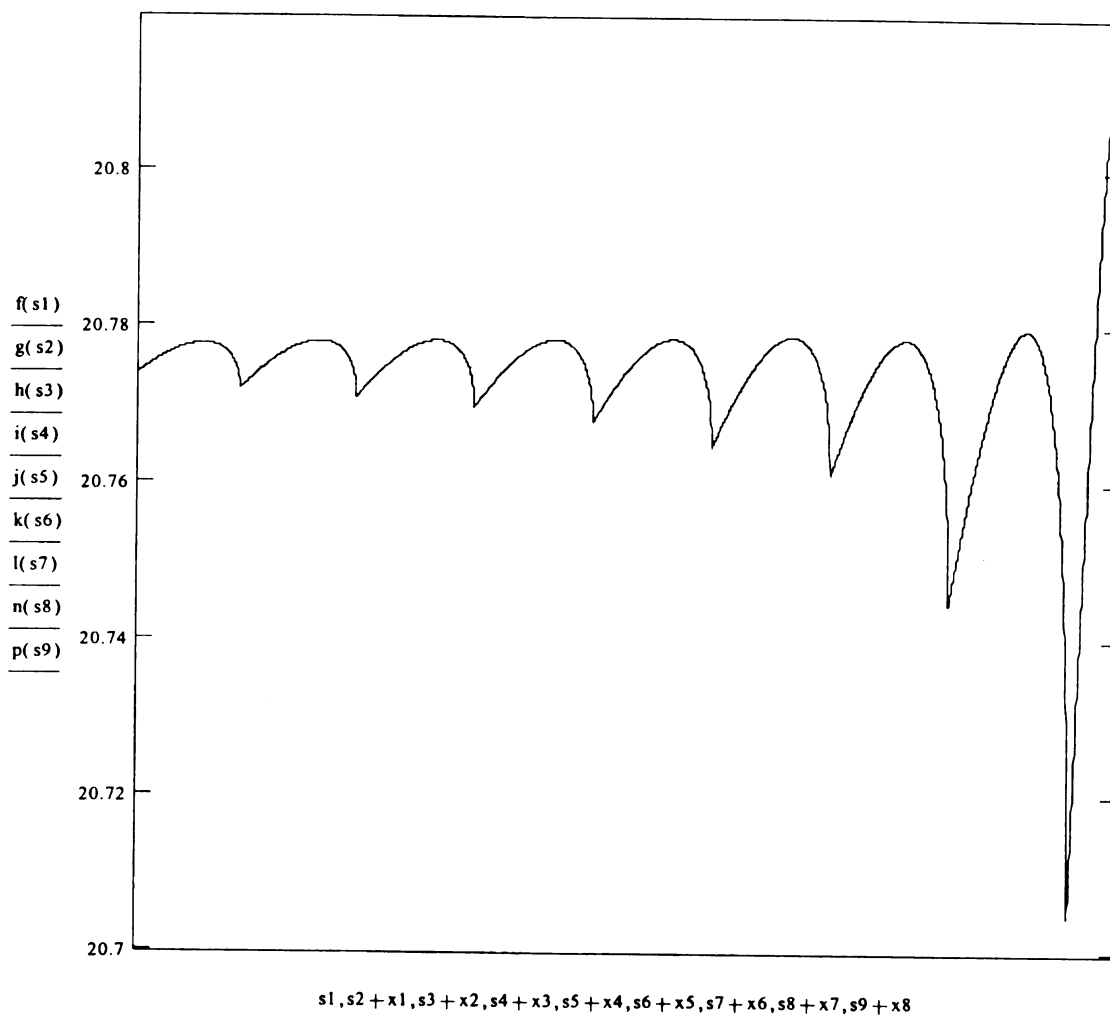
$$s8 := 0.000, 0.001 .. L8$$

$$n(s8) := C \cdot \sqrt{2 \cdot m} \cdot \left[\frac{D}{2 \cdot \sqrt{s8 \cdot E8 + L7 \cdot E7 + L6 \cdot E6 + L5 \cdot E5 + L4 \cdot E4 + L3 \cdot E3 + L2 \cdot E2 + L1 \cdot E1 + V0}} \right. ...$$

$$+ \frac{\sqrt{U_0 + q \cdot s8 \cdot E8} - \sqrt{U_0}}{q \cdot E8} + \frac{\left[\sqrt{U_0 + q \cdot (s8 \cdot E8 + L7 \cdot E7)} - \sqrt{U_0 + q \cdot s8 \cdot E8}\right]}{q \cdot E7} ...$$

$$+ \frac{\left[\begin{array}{l}\sqrt{U_0 + q \cdot (s8 \cdot E8 + L7 \cdot E7 + L6 \cdot E6)} ... \\ + -\sqrt{U_0 + q \cdot (s8 \cdot E8 + L7 \cdot E7)}\end{array}\right]}{q \cdot E6} ...$$

$$+ \frac{\left[\begin{array}{l}\sqrt{U_0 + q \cdot (s8 \cdot E8 + L7 \cdot E7 + L6 \cdot E6 + L5 \cdot E5)} ... \\ + -\sqrt{U_0 + q \cdot (s8 \cdot E8 + L7 \cdot E7 + L6 \cdot E6)}\end{array}\right]}{q \cdot E5} ...$$

$$+ \frac{\left[\begin{array}{l}\sqrt{U_0 + q \cdot (s8 \cdot E8 + L7 \cdot E7 + L6 \cdot E6 + L5 \cdot E5 + L4 \cdot E4)} ... \\ + -\sqrt{U_0 + q \cdot (s8 \cdot E8 + L7 \cdot E7 + L6 \cdot E6 + L5 \cdot E5)}\end{array}\right]}{q \cdot E4} ...$$

$$+ \frac{\left[\begin{array}{l}\sqrt{U_0 + q \cdot (s8 \cdot E8 + L7 \cdot E7 + L6 \cdot E6 + L5 \cdot E5 + L4 \cdot E4 + L3 \cdot E3)} ... \\ + -\sqrt{U_0 + q \cdot (s8 \cdot E8 + L7 \cdot E7 + L6 \cdot E6 + L5 \cdot E5 + L4 \cdot E4)}\end{array}\right]}{q \cdot E3} ...$$

$$+ \frac{\left[\begin{array}{l}\sqrt{U_0 + q \cdot (s8 \cdot E8 + L7 \cdot E7 + L6 \cdot E6 + L5 \cdot E5 + L4 \cdot E4 + L3 \cdot E3 + L2 \cdot E2)} ... \\ + -\sqrt{U_0 + q \cdot (s8 \cdot E8 + L7 \cdot E7 + L6 \cdot E6 + L5 \cdot E5 + L4 \cdot E4 + L3 \cdot E3)}\end{array}\right]}{q \cdot E2} ...$$

$$+ \frac{\left[\begin{array}{l}\sqrt{U_0 + q \cdot (s8 \cdot E8 + L7 \cdot E7 + L6 \cdot E6 + L5 \cdot E5 + L4 \cdot E4 + L3 \cdot E3 + L2 \cdot E2 + L1 \cdot E1)} ... \\ + -\sqrt{U_0 + q \cdot (s8 \cdot E8 + L7 \cdot E7 + L6 \cdot E6 + L5 \cdot E5 + L4 \cdot E4 + L3 \cdot E3 + L2 \cdot E2)}\end{array}\right]}{q \cdot E1} ...$$

$$\left. + \frac{\left[\begin{array}{l}\sqrt{U_0 + q \cdot \left(\begin{array}{l}s8 \cdot E8 + L7 \cdot E7 + L6 \cdot E6 + L5 \cdot E5 ... \\ + L4 \cdot E4 + L3 \cdot E3 + L2 \cdot E2 + L1 \cdot E1 + d \cdot E0\end{array}\right)} ... \\ + -\sqrt{U_0 + q \cdot \left(\begin{array}{l}s8 \cdot E8 + L7 \cdot E7 + L6 \cdot E6 + L5 \cdot E5 ... \\ + L4 \cdot E4 + L3 \cdot E3 + L2 \cdot E2 + L1 \cdot E1\end{array}\right)}\end{array}\right]}{q \cdot E0} \right]$$

$$s9 := 0.000, 0.001 .. L9$$

$$p(s9) := C \cdot \sqrt{2 \cdot m} \cdot \left[\frac{D}{2 \cdot \sqrt{s9 \cdot E9 + L8 \cdot E8 + L7 \cdot E7 + L6 \cdot E6 + L5 \cdot E5 + L4 \cdot E4 + L3 \cdot E3 + L2 \cdot E2 + L1 \cdot E1 + V0}} \cdots \right.$$

$$+ \frac{\sqrt{U_0 + q \cdot s9 \cdot E9} - \sqrt{U_0}}{q \cdot E9} + \frac{\left[\sqrt{U_0 + q \cdot (s9 \cdot E9 + L8 \cdot E8)} - \sqrt{U_0 + q \cdot s9 \cdot E9} \right]}{q \cdot E8} \cdots$$

$$+ \frac{\left[\sqrt{U_0 + q \cdot (s9 \cdot E9 + L8 \cdot E8 + L7 \cdot E7)} \cdots {} + -\sqrt{U_0 + q \cdot (s9 \cdot E9 + L8 \cdot E8)} \right]}{q \cdot E7} \cdots$$

$$+ \frac{\left[\sqrt{U_0 + q \cdot (s9 \cdot E9 + L8 \cdot E8 + L7 \cdot E7 + L6 \cdot E6)} \cdots {} + -\sqrt{U_0 + q \cdot (s9 \cdot E9 + L8 \cdot E8 + L7 \cdot E7)} \right]}{q \cdot E6} \cdots$$

$$+ \frac{\left[\sqrt{U_0 + q \cdot (s9 \cdot E9 + L8 \cdot E8 + L7 \cdot E7 + L6 \cdot E6 + L5 \cdot E5)} \cdots {} + -\sqrt{U_0 + q \cdot (s9 \cdot E9 + L8 \cdot E8 + L7 \cdot E7 + L6 \cdot E6)} \right]}{q \cdot E5} \cdots$$

$$+ \frac{\left[\sqrt{U_0 + q \cdot (s9 \cdot E9 + L8 \cdot E8 + L7 \cdot E7 + L6 \cdot E6 + L5 \cdot E5 + L4 \cdot E4)} \cdots {} + -\sqrt{U_0 + q \cdot (s9 \cdot E9 + L8 \cdot E8 + L7 \cdot E7 + L6 \cdot E6 + L5 \cdot E5)} \right]}{q \cdot E4} \cdots$$

$$+ \frac{\left[\sqrt{U_0 + q \cdot (s9 \cdot E9 + L8 \cdot E8 + L7 \cdot E7 + L6 \cdot E6 + L5 \cdot E5 + L4 \cdot E4 + L3 \cdot E3)} \cdots {} + -\sqrt{U_0 + q \cdot (s9 \cdot E9 + L8 \cdot E8 + L7 \cdot E7 + L6 \cdot E6 + L5 \cdot E5 + L4 \cdot E4)} \right]}{q \cdot E3} \cdots$$

$$+ \frac{\left[\sqrt{U_0 + q \cdot (s9 \cdot E9 + L8 \cdot E8 + L7 \cdot E7 + L6 \cdot E6 + L5 \cdot E5 + L4 \cdot E4 + L3 \cdot E3 + L2 \cdot E2)} \cdots {} + -\sqrt{U_0 + q \cdot (s9 \cdot E9 + L8 \cdot E8 + L7 \cdot E7 + L6 \cdot E6 + L5 \cdot E5 + L4 \cdot E4 + L3 \cdot E3)} \right]}{q \cdot E2} \cdots$$

$$+ \frac{\left[\sqrt{U_0 + q \cdot \left(\begin{array}{l} s9 \cdot E9 + L8 \cdot E8 + L7 \cdot E7 + L6 \cdot E6 + L5 \cdot E5 \cdots \\ + L4 \cdot E4 + L3 \cdot E3 + L2 \cdot E2 + L1 \cdot E1 \end{array} \right)} \cdots {} + -\sqrt{U_0 + q \cdot \left(\begin{array}{l} s9 \cdot E9 + L8 \cdot E8 + L7 \cdot E7 + L6 \cdot E6 \cdots \\ + L5 \cdot E5 + L4 \cdot E4 + L3 \cdot E3 + L2 \cdot E2 \end{array} \right)} \right]}{q \cdot E1} \cdots$$

$$\left. + \frac{\left[\sqrt{U_0 + q \cdot \left(\begin{array}{l} s9 \cdot E9 + L8 \cdot E8 + L7 \cdot E7 + L6 \cdot E6 + L5 \cdot E5 \cdots \\ + L4 \cdot E4 + L3 \cdot E3 + L2 \cdot E2 + L1 \cdot E1 + d \cdot E0 \end{array} \right)} \cdots {} + -\sqrt{U_0 + q \cdot \left(\begin{array}{l} s9 \cdot E9 + L8 \cdot E8 + L7 \cdot E7 + L6 \cdot E6 + L5 \cdot E5 \cdots \\ + L4 \cdot E4 + L3 \cdot E3 + L2 \cdot E2 + L1 \cdot E1 \end{array} \right)} \right]}{q \cdot E0} \right]$$

$x1 := L1 \quad x2 := x1 + L2 \quad x3 := x2 + L3 \quad x4 := x3 + L4 \quad x5 := x4 + L5$

$x6 := x5 + L6 \quad x7 := x6 + L7 \quad x8 := x7 + L8$

$\dfrac{f(s1)}{}$

$\dfrac{g(s2)}{}$

$\dfrac{h(s3)}{}$

$\dfrac{i(s4)}{}$

$\dfrac{j(s5)}{}$

$\dfrac{k(s6)}{}$

$\dfrac{l(s7)}{}$

$\dfrac{n(s8)}{}$

$\dfrac{p(s9)}{}$

$s1, s2 + x1, s3 + x2, s4 + x3, s5 + x4, s6 + x5, s7 + x6, s8 + x7, s9 + x8$

LINEAR.mcd Program for modeling two-stage linear-acceleration ion source parameters. Given the ion source parameters, the arrival time at the detector is calculated for ions located axially along the ionization region. The data is plotted and saved to a file. (Written in Mathcad ver. 4.0)
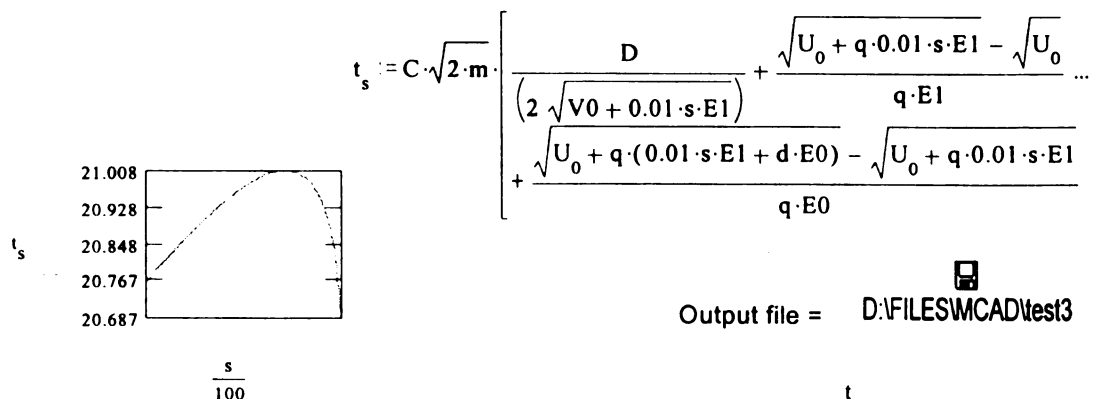
Step 1: Identify ion source parameters

mass $\quad$ m $:= 56$

charge $\quad$ q $:= 1$

Unit conversion constant $\quad$ C $:= 1.017941$

acceleration length (cm) $\quad$ d $:= 0.648$

distance to detector (cm) $\quad$ D $:= 153$

voltage applied to acceleration region (volts) $\quad$ V0 $:= 1629$ $\qquad$ Total voltage $\quad$ V1 $:= 1887$

Initial energy (eV)

$\qquad$ $U_0 := 0$ $\qquad$ Ionization length (cm) $\quad$ s $:= 2.5$

Calculation of acceleration region electric field $\quad$ E0 $:= \dfrac{V0}{d}$ $\qquad$ E0 $= 2.514 \cdot 10^3$

$\qquad$ E1 $:= \dfrac{(V1 - V0)}{s}$ $\qquad$ E1 $= 103.2$

Step 2: Calculate ion arrival time (in μsec) at detector for ions traversing only the acceleration region.

$$t_D := C \cdot \frac{D \cdot \sqrt{2 \cdot m}}{\left(2 \cdot \sqrt{V0}\right)} \qquad t_d := C \cdot \frac{\sqrt{2 \cdot m}}{q \cdot E0} \cdot \left(\sqrt{U_0 + q \cdot d \cdot E0} - \sqrt{U_0}\right)$$

$t_D = 20.419$ $\qquad$ $t_d = 0.173$ $\qquad$ $t := t_D + t_d$ $\qquad$ $t = 20.592$

Step 3: Calculate the electric fields required for each ionization region where the axial location of the ionization region is between the electrodes at s(x).

$$s := 1, 2 .. 250$$

$$t_s := C \cdot \sqrt{2 \cdot m} \cdot \left[\frac{D}{\left(2 \sqrt{V0 + 0.01 \cdot s \cdot E1}\right)} + \frac{\sqrt{U_0 + q \cdot 0.01 \cdot s \cdot E1} - \sqrt{U_0}}{q \cdot E1} \cdots \right.$$
$$\left. + \frac{\sqrt{U_0 + q \cdot (0.01 \cdot s \cdot E1 + d \cdot E0)} - \sqrt{U_0 + q \cdot 0.01 \cdot s \cdot E1}}{q \cdot E0} \right]$$

21.008
20.928
t_s 20.848
20.767
20.687

$\dfrac{s}{100}$

Output file = D:\FILES\MCAD\test3

t

Appendix C

ON THE MASS-INDEPENDENCE OF NON-LINEAR ION ACCELERATION

The theory describing non-linear ion acceleration incorporates, as a fundamental tenent, the expectation that space focusing is mass independent. While the data used to validate the concepts of non-linear ion acceleration and complete space focusing are derived from the temporal characteristics of a single m/z, the theory is expanded to cover the entire m/z range. The justification for this is based on an evaluation of the analytical equations describing ion motion, previously derived in Chapter 4. According to Equation 4-8, the time-of-flight for any ion is proportional to the square root of the m/z times the electric field function. The time will change with the m/z, but the electric field remains constant. Likewise, as multiple linear electric fields are added, as in Equation 4-20, the time-of-flight remains proportional to the square root of the m/z. A second, and more direct argument for mass independence comes from an evaluation of Equation 4-14, where it is clearly seen that the distance at which two ions, beginning from different axial locations within the ion source, become coincident, is independent of mass. While Equation 4-14 is derived from the Wiley/McLaren two linear field model, the same mass-independent relationship holds when a series of linear fields is incorporated in the model. A third argument comes from an evaluation the potential profile required to achieve complete space focusing, derived using the LINEAR program. This computational program verifies that, for a given instrumental configuration, the potential profile required to provide complete space focusing for a low m/z (m/z 50) is identical to the potential profile required to achieve the same effect with a relatively high m/z (m/z 5000).